GPU BASED INFRARED SIGNATURE MODELING AND SCENE
SIMULATION

A THESIS SUBMITTED TO
THE GRADUATE SCHOOL OF NATURAL AND APPLIED SCIENCES
OF
MIDDLE EAST TECHNICAL UNIVERSITY

BY

ÇAĞLAR KAVAK

IN PARTIAL FULFILLMENT OF THE REQUIREMENTS
FOR
THE DEGREE OF MASTER OF SCIENCE
IN
ELECTRICAL AND ELECTRONICS ENGINEERING

JUNE 2014

Approval of the thesis:

GPU BASED INFRARED SIGNATURE MODELING AND SCENE SIMULATION

submitted by **ÇAĞLAR KAVAK** in partial fulfillment of the requirements for the degree of **Master of Science in Electrical and Electronics Engineering Department, Middle East Technical University** by,

Prof. Dr. Canan Özgen
Dean, Graduate School of **Natural and Applied Sciences**   _____

Prof. Dr. Gönül Turhan Sayan
Head of Department, **Electrical and Electronics Engineering**   _____

Prof. Dr. Gözde Bozdağı Akar
Supervisor, **Electrical and Electronics Eng. Dept., METU**   _____

Assist. Prof. Dr. Ahmet Oğuz Akyüz
Co-supervisor, **Computer Engineering Dept., METU**   _____

Examining Committee Members:

Prof. Dr. Veysi İşler
Computer Engineering Dept., METU   _____

Prof. Dr. Gözde Bozdağı Akar
Electrical and Electronics Engineering Dept., METU   _____

Assist. Prof. Dr. Ahmet Oğuz Akyüz
Computer Engineering Dept., METU   _____

Assoc. Prof. Dr. İlkay Ulusoy
Electrical and Electronics Engineering Dept., METU   _____

Assist. Prof. Dr. Fatih Kamışlı
Electrical and Electronics Engineering Dept., METU   _____

Date: _____

I hereby declare that all information in this document has been obtained and presented in accordance with academic rules and ethical conduct. I also declare that, as required by these rules and conduct, I have fully cited and referenced all material and results that are not original to this work.

Name, Last Name: ÇAĞLAR KAVAK

Signature   :

ABSTRACT

GPU BASED INFRARED SIGNATURE MODELING AND SCENE SIMULATION

KAVAK, ÇAĞLAR

M.S., Department of Electrical and Electronics Engineering

Supervisor   : Prof. Dr. Gözde Bozdağı Akar

Co-Supervisor   : Assist. Prof. Dr. Ahmet Oğuz Akyüz

June 2014, 113 pages

The need of a fast and high fidelity scene simulation system is important for the development of modern infrared (IR) imaging systems. The performance testing of these systems is expensive and also depends on environment conditions. However, computer based systems can provide a cost effective alternative to field trials. Ray tracing provides physical accuracy and photo realism for scene generation. However, it has computationally intensive nature and conventionally used for non-real time applications. The development of Graphics Processor Unit (GPU) technology makes ray tracing more available for real time applications. NVIDIA® OptiX™ ray tracing engine, runs on top of the NVIDIA® CUDA™ parallel computing architecture, is primarily applied on visual band rendering and it has not been yet used in physics based scene simulation in the IR region. In this thesis work, an effort is made to model physics based IR scene simulation with OptiX. The developed system is tested on several benchmarks and also the effects of the signature components are analyzed. The results show that spectral dependency of the radiometric data and atmosphere effects are important and must be taken into account. Moreover, the results show that current GPU technology can generate high fidelity IR images at high frame rates.

Keywords: Infrared Scene Simulation, GPU, Signature Modeling, Ray Tracing

ÖZ

GPU TABANLI KIZILÖTESİ İZ MODELLEME VE SAHNE BENZETİMİ

KAVAK, ÇAĞLAR

Yüksek Lisans, Elektrik ve Elektronik Mühendisliği Bölümü

Tez Yöneticisi   : Prof. Dr. Gözde Bozdağı Akar

Ortak Tez Yöneticisi   : Yrd. Doç. Dr. Ahmet Oğuz Akyüz

Haziran 2014 , 113 sayfa

Modern kızılötesi (KÖ) sistemlerin geliştirilmesi için hızlı ve yüksek doğruluğa sahip sahne benzetimi sistemine ihtiyaç duyulmaktadır. Bu sistemlerin testleri yüksek maliyet gerektirmekte ve ortam koşullarına bağlıdır. Bilgisayar tabanlı sahne benzetimleri ise açık saha denemelerine nazaran uygun maliyetli çözümler sunabilmektedir. Işın izleme, fiziksel doğruluk ve fotogerçekçilik sağlamaktadır. Ancak, ışın izleme algoritması yoğun hesaplamalar içerdiği için genellikle gerçek zamanlı olmayan uygulamalarda kullanılmaktadır. Grafik işlem birimi (GPU) teknolojisindeki gelişmeler, paralel işlem yürütme kabiliyetleri ile ışın izleme algoritmasını gerçek zamanlı uygulamalar için uygun hale getirmektedir. NVIDIA paralel hesaplama mimarisi (CUDA) üzerinde çalışan NVIDIA OptiX ışın izleme motoru, öncelikli olarak görsel bant uygulamarında kullanılmış ve henüz KÖ bantta fizik tabanlı sahne benzetimine uygulanmamıştır. Tez kapsamında OptiX ile KÖ bantta fizik tabanlı sahne benzetimi çalışmaları yapılmıştır. Geliştirilen sistem çeşitli senaryolar üzerinde test edilip ayrıca iz bileşenlerinin etkileri incelenmiştir. Analizler sonucunda, gerçekçi KÖ imgeler oluşturmak için izgesel bağımlılık ve atmosferik etkilerin önemli olduğu gösterilmiştir. Bunun yanında, günümüz GPU teknolojisi ile yüksek doğruluk ve çerçeve hızlarında KÖ imgeler oluşturulabilir sonucuna varılmıştır.

Anahtar Kelimeler: Kızılötesi Sahne Benzetimi, GPU, İz Modelleme, Işın İzleme

To My Family

ACKNOWLEDGMENTS

TABLE OF CONTENTS

LIST OF TABLES

TABLES

LIST OF FIGURES

FIGURES

xvi

LIST OF ABBREVIATIONS

2D	Two Dimensional
3D	Three Dimensional
API	Application Programmers Interface
BRDF	Bidirectional Reflectance Distribution Function
BVH	Bounding Volume Hierarchy
CAD	Computer Aided Design
COTS	Commercial Off-The-Shelf
CUDA	Compute Unified Device Architecture
CPU	Central Processing Unit
DHR	Directional Hemispheric Reflectance
DSTO	Defence Science and Technology Organisation
EO	Electro Optics
FOV	Field Of View
FPS	Frame Per Second
GPGPU	General Purpose Graphics Processor Unit
GPU	Graphics Processing Unit
HDR	Hemispherical Directional Reflectance
IR	InfraRed
LOS	Line Of Sight
LOWTRAN	LOW resolution TRANsmission
LWIR	Long Wave InfraRed
MODTRAN	MODerate resolution TRANsmission
MWIR	Mid Wave InfraRed
OpenCL	Open Computing Language
OpenGL	Open Graphics Library
PC	Personal Computer
SGI	Silicon Graphics Incorporated
SM	Streaming Multiprocessors
SWIR	Short Wave InfraRed

CHAPTER 1

INTRODUCTION

The design, development and optimisation of modern infrared imaging systems requires the use of scene simulation systems to create realistic images of infrared signatures. These simulation systems are used in signature prediction, the development and optimisation of missile seeker sensors and image processing algorithms. A physics based accurate signature modeling and simulation system can greatly assist in the development of infrared imaging systems.

Generally, the infrared imaging characteristics of objects are tested by measurements. However, the performance evaluation, training and testing of infrared imaging systems are time consuming, very expensive and also dependent on atmospheric factors which are difficult to control. Whereas, a computer based signature modeling and scene simulation system can provide a cost effective alternative to field trials in which different complicated conditions can be simulated in a relatively short time with controlled environmental factors.

The most important points in developing these simulators are the physical accuracy and performance. Modern Graphics Processor Unit (GPU) cards are manycore architectures with thousands of cores which can be used to get impressive performance. These cards are primarily designed for the gaming industry. Recently, these have been used to accelerate physics based algorithms using General Purpose Graphics Processor Unit (GPGPU) techniques by a parallel nature.

1.1 Problem Statement

The analysis of infrared characteristics of an object is an essential problem in many scientific and engineering fields. The direction of propagation of radiant flux from the source to the sensor is called the path. Along this path, the flux can be absorbed, transmitted, or reflected by either an object, its background or the atmosphere. Infrared scene generation is different from conventional visible band scene simulations due to the fact that every object within the scene above $0°K$ is a source.

The infrared signatures of objects are affected by multitude of factors in the real world. The source of incident radiation from each surface element on the sensor is dependent on material optical properties, spatial temperature distribution, background radiation, reflected direct solar and sky radiation, atmospheric degradation, spectral system response of the sensor and more, all affect the signature of the object. The signature also dynamically varies as a result of heat exchanges on the object from the convection, conduction and radiation. In order to model the signature of the object accurately, the radiometric equation must take into account all of these components. Moreover, one of the main challenges for infrared scene simulations is that the spectral variation of radiometric data directly affects the incident radiation. Hence, computations are required to be integrated in spectral waveband interval of interest. The calculation of each of the items mentioned above require a massive amount of computer power.

Ray tracing represents propagating electromagnetic fields as collections of rays perpendicular to the lines of constant flux. It is capable of producing physics based high quality realistic images. However, the computational cost of this algorithm is significant. The rendering of high quality images of complex scenes can take hours. Moreover, ray tracing algorithms are generally employed solely in the domain of Central Processing Unit (CPU) based environments. Three dimensional (3D) complex virtual world geometry comprises of many surfaces. Therefore, ray tracing applications require enormous calculation and significant CPU time. However, as computers are acquiring the sufficient computing power, ray tracing has become a valid alternative for simulating these kinds of complex scenarios more realistic, and in real time.

Ray tracing algorithm is well suited for the GPU since it is an embarrassingly parallel problem. NVIDIA® OptiX™ is a generic GPU ray tracing engine and it runs on the NVIDIA® CUDA™ parallel computing architecture. OptiX ray tracing engine is primarily used to render the images in the visible band. As far as we know, there is no ray tracer based infrared signature model and scene simulation renderer developed with OptiX engine which can utilize GPU parallel processing power.

1.2 Objectives

In this thesis work, the main objective is to develop a GPU based high fidelity infrared signature model to simulate realistic infrared scenes utilizing parallel processing power of GPU technology and analyze the effects of the signature models on the infrared radiation and the performance of the infrared scene simulation.

The other objectives of this study are listed as follows.

- To demonstrate that it is possible to simulate infrared scenes on a low cost personal computer (PC).

- To develop high fidelity infrared signature models from physical radiometric principles.

- To demonstrate that OptiX ray tracing engine can be extended to simulate infrared band scenes.

- To generate physically realistic object and background infrared signatures under a different atmospheric and infrared waveband conditions.

- To integrate a radiative transfer model to simulate the effects of the atmosphere.

- To render high fidelity infrared scene of the spectral signature model on GPU at high frame rates.

1.3 Related Work

This section presents earlier studies related to infrared signature models, radiometric equations and GPU based rendering systems found in literature.

Due to the complexities of infrared signature computation, over the past 20 years, several studies have produced many computer models for infrared signature prediction and scene simulation. Since infrared scene generation software is a critical technology for countries, these studies are not published without limitation and specific algorithms of these tools are either classified or commercial-in-confidence. Therefore, only restricted information is presented about signature modeling, radiometric fidelity and capability in literature. For this reason, the information about infrared signature simulation systems addressed here is obtained from open literature.

Previously, the generation of real time images used to be limited to graphics supercomputers such as Silicon Graphics Incorporation (SGI) Onyx2. These computers utilize dedicated hardware and multiple processors to generate images at high frame rates. The development of a new generation of PC graphics cards make it possible to generate images using just a PC and a commercial off the shelf (COTS) graphics card. Graphics libraries, such as OpenGL, are developed to render visual images on GPU, but it is possible to generate infrared images using OpenGL [1].

With the development of GPU technology, programmable graphics hardware applications have been developed with OpenGL. Previously, it was difficult to program with graphics hardware due to the fixed function pipelines. Now, programmable vertex and fragment shaders enable to use the GPU for other things than rasterization [2].

In 2007, Nvidia launched a parallel computing architecture, CUDA [3]. Since its release, CUDA has been widely utilized for parallel ray tracing research and many other problems. Then, Nvidia released its ray tracing engine named OptiX [4] in 2009. OptiX is a framework built on Nvidia CUDA GPU computing architecture with the purpose of simplifying development of ray tracing based applications. OptiX has proven to be a good ray tracing engine and have the capability of using GPU efficiently [5].

There are different kinds of infrared scene simulators for different purposes and various infrared signature models are proposed in the literature. Some of these works propose ray tracing based high fidelity radiometric signature models which are time consuming and heavy on computations on CPU. Whereas in computer graphics community, OpenGL based infrared signature models are performed on GPU with high frame rates but less radiometric accuracy.

Ray tracing algorithms are more suitable to the physical signature models where simulating the light interactions is the main part of the signature calculation. These kind of algorithms provide radiometric fidelity but they are really hard to have in real time and needs lots of computations. But the scenes really resembles the real physical world. The papers like [6–11] based on these physical model solutions contain highly detailed terrains, Bidirectional Reflectance Distribution Function (BRDF) models, atmospheric effects, detailed object geometry and thermal signature models. On the other hand, the models presented in references [12–14] are simple and easy to use for low fidelity models. Although, simple radiometric equations could not provide high fidelity, it is considered as sufficient for their application needs under the assumptions. These algorithms investigates to determine the optimum balance between simulation accuracy and calculation time [15–20]. Since it is really hard to have high fidelity in real time systems this approach is more suitable for real time simulation systems.

[21] presents a ray tracer based simplified infrared signature model developed on CPU. The phong lighting model [22] is used to calculate infrared signatures. This study ignores spectral dependency and atmospheric effects in their signature equation. To compute blackbody emissions, a polynomial fitting method is used to reduce integration cost. But this approach makes the calculations tightly depend on the infrared camera. Also their signature model is not physical.

[1, 14, 20] propose a mapping method to represent radiometric quantities with equivalent OpenGL variables in order to use with standart pipeline. Thermal emissions, reflections and atmospheric parameters are mapped to OpenGL parameters. However, these radiometric entities are dependent on spectral parameters. It is therefore not always accurate to replace such a spectrally variant entity with a single parameter that is required by standart OpenGL.

[20] describes a real time infrared sensor simulation system known as Paint the Night (PTN) that is developed to generate synthetic imagery for infrared sensors. The system implements OpenGL to generate the imagery but runs on special SGI hardware. The authors propose a mapping model to represent radiometric quantities with equivalent OpenGL variables. Scene objects are assumed lambertian emitters and diffuse reflectors. In order to approximate directional reflections, specular reflection fraction parameter is defined. OpenGL lighting model approach is used to model infrared signatures. But the accuracy of the method is not described.

[19] describes the radiometric equations employed by an infrared scene generation COTS software package called SensorVision that is used in conjuction with Vega Prime IR Scene [18], a 3D database visualisation software package developed by Paradigm Incorporated, to generate real time infrared scenes. SensorVision and Vega Prime IR Scene are OpenGL based scene simulation systems. Since these simulation systems aim to achieve real time performance, radiometric equations implemented in SensorVision and Vega Prime IR Scene generates errors resulting from approximations employed. One of the important approximation is that the physically accurate calculation is only applied to the radiance incident on the center pixel in the image frame. Therefore, it can generate infrared images accurately for small field of views (FOV). Another important approximation is that in the integration of spectral radiance quantities over wavelength, their signature models move various spectral parameters outside the integral. Materials with spectral reflection coefficients that fluctuate over the spectral band of interest may cause significant errors in the signature calculation. In addition, the use of the average atmospheric transmittance affects the accuracy.

In paper [11] a technique for longwave infrared (LWIR) synthetic image generation is proposed. This study uses LOWTRAN® radiative transfer model [23] to model atmospheric effects and computer graphics ray tracing techniques. The radiance from an object in the scene is represented with its temperature and material optical characteristics. Solar reflected radiations are not considered in this study and spectral dependency of each of radiometric components is omitted due to LWIR infrared region characteristics. Also it is assumed that all materials fall into two categories, specular or diffuse reflectors. Ray tracing algorithm is used to incorporate secondary reflections from the background radiation.

The Digital Imaging and Remote Sensing Image Generation (DIRSIG) is a physics based scene generation system [6]. DIRSIG can produce synthetic images of complex scenes in the visible and infrared regions with ray tracing based algorithms. The signature model equation uses diffuse and specular material approach to model the BRDF for the reflections. The temperatures of objects in the scene are calculated by applying a thermodynamic model. The model includes heat conduction into the bulk of the material, heat transfer by convection and radiation [10, 24]. Moreover, DIRSIG uses MODTRAN® software [25] to correct the atmospheric effects. A full hemisphere sky map is obtained from MODTRAN and is used for sky radiance calculation [24]. It is observed that the DIRSIG signature model is not developed for real time applications.

SAFIR is an infrared scene generation software which is developed for realistic rendering of 3D scenes [9]. It can produce physics based simulated images for air, land and sea scenarios in the visible and infrared bands. In order to calculate scene radiance, SAFIR employs a 3D description of all objects in the scene, object material properties, surface temperature and atmospheric conditions in the scenario. The ray tracing based algorithms are used by SAFIR to calculate the reflectance between surfaces. SAFIR radiometry model considers atmospheric effects by calculating spectral atmospheric transmittance and path radiance. Also the effects of sensor spectral response are employed by sensor model.

The Optronic Scene Simulator (OSSIM) is a scene simulation system which generates synthetic images of complex scenes in the $0.4 - 20 \ \mu m$ spectral region [7]. All calculations in the OSSIM radiometric signature equation are wavelength based to consider the spectral nature of radiation sources. OSSIM signature model considers spectral atmospheric attenuation and atmospheric path radiance by using MODTRAN software. OSSIM thermal model calculates object and terrain radiative temperatures with a heat balance equation [26]. OSSIM rendering equation models thermally emitted radiance, diffuse and specular reflected solar radiance, reflected background and sky radiance with including sensor spectral response, atmospheric transmittance and path radiance effects. OSSIM scene simulation system is not developed for real time applications.

Australian Defence Science and Technology Organisation (DSTO) has a OpenGL based suite of software tools called VIR Suite that is developed for real time generation of radiometrically scaled infrared scenes [15–17].

The paper [16] presents an infrared scene simulation method from the radiometric perspective and describes the techniques they perform to enable real time rendering processing of complex scenes. These techniques include preprocessed in-band emission calculations, storage of offline MODTRAN generated data, the use of environmental cubemap textures for background contributions and BRDF approximation for reflectance characteristics of different surface types. The basic concept of the radiometry model is to associate a list of properties such as temperature and emissivity or directly apparent temperature into scene objects surfaces and paint them with this radiometric scaled colors. They assume that the lack of exact radiometric calculation and the level of radiance calculation approximations are not critical for their application needs. For this purpose, they use band-averaged values for atmospheric transmittance, sensor spectral response and material optical properties in radiometric signature calculations. These approximations are well justified when radiometric data have little spectral variation accross the band of interest. But some of the spectral infrared regions, such as midwave infrared (MWIR), atmospheric transmittance values have significant spectral variation. Because material optical properties such as emissivity and reflectivity have also spectral variation, graybody material assumption may not be accurate for the radiometric calculation model. Furthermore, in many cases the spectral sensor response may not be characterised exactly.

In order to calculate reflections, [16, 17] proposes an approximation to BRDF reflection integral by using the environment map technique to render the sky cubemap. Specular reflection is assumed and the effect of the surface roughness is employed by blurring the sky radiance. This method is useful for simulating different reflections effects but it is not possible to simulate physics based surface BRDFs.

[17] is the new VIR Suite module that proposes a dynamic heat transfer solver to calculate temperature distributions through target and background terrain surfaces. The dynamic thermal signature model is used to predict thermal signatures when measured data are unavailable or insufficient. Two versions of this model exits, one for

offline prediction and the other for dynamic runtime calculations. Offline computation of thermal signatures provides high fidelity module but dynamic surface temperatures calculation for real time application provides lower fidelity.

In [27], the spectral scattering calculations from sky and background radiation are implemented in a parallel fashion by using CUDA. The computation process is partitioned into many threads running in GPU kernel and each thread computes a visible surface element infrared spectral scattering intensity in a specific incident direction. They demonstrate that the CUDA parallel calculation speed improves CPU calculation more than two hundred times.

1.4   Contribution

As it can be seen from the literature research, ray tracing based signature models provide high fidelity and radiometric accuracy. Since ray tracing algorithms lead to a significant computational cost by nature and generally applied on CPU environment, these simulation systems are not suitable for high frame rates purposes. Rasterization based infrared scene simulations are developed on GPU with OpenGL library to utilize parallel processing power. OpenGL based scene signature radiometry models share a common approach for the rendering of infrared images. These models are generally employ similar radiometric equations in order to calculate signatures. Spectral variation is ignored and band-averaged values are used for radiometric data such as atmospheric effects to avoid integral computations. Also, only specular and diffuse surfaces are assumed in order to approximate the BRDF model. Moreover, multiple reflection computations are ignored and only final incident radiation from the object into the sensor is considered to speed up signature calculations. Thus, OpenGL based real time purpose infrared scene simulation studies have less radiometric accuracy due to their signature modeling assumptions.

In this thesis work, a GPU based infrared scene simulation system is developed. It can simulate accurate 3D scenes with physics based spectral signature calculations in MWIR and LWIR bands at high frame rates. To achieve this, the computing power of the graphics cards is the core computational method used in this work. This is

done by using the OptiX ray tracing engine for most of the heavy calculations. OptiX is primarily used to render images in the visible band. However, this thesis work demonstrates that it can be used to model the infrared scene simulations. Another contribution of this thesis work is to demonstrate the effects of the spectral variations of the signature components on radiation computation in the infrared bands.

1.5 Report Outline

This report is divided into six chapters. The rest of the thesis is organized as follows.

Chapter 2 gives useful background information which is helpful to know when reading the rest of the thesis about radiometric principles, bidirectional reflectance distribution function, radiative transfer through atmosphere, basics of scene simulation, ray tracing and parallel processing on GPU.

Chapter 3 explains the detailed description of the infrared signature modeling. Also, the development of the infrared signature model for the scene simulation is proposed.

Chapter 4 describes implementation of the infrared scene simulation in OptiX.

Chapter 5 gives the simulation and analysis results with rendered infrared images.

Finally, Chapter 6 concludes this thesis work with a summary of the results and facts found during this project and future work to be accomplished.

CHAPTER 2

BACKGROUND

This chapter provides applicable background theory and information for the reader that is useful in understanding the concepts and methods described in this thesis work. Analytical proofs and more advanced topics are outside the scope of the thesis.

This chapter is structured to start with radiometry theory that is required to understand infrared signature modeling concepts in Section 2.1, followed by a detailed description of the BRDF and surface reflectance structures in Section 2.2. Section 2.3 deals with radiative transmission through atmosphere. Then, basic concepts of scene simulation are introduced in Section 2.4. After that ray tracing algorithm is described in Section 2.5. Lastly, Section 2.6 contains a brief introduction to the parallel processing on GPU. This section also introduces CUDA and OptiX, Nvidia's parallel computing platform and ray tracing engine.

2.1 Radiometric Overview

The purpose of this section is to highlight the radiometric principles that are relevant to this study. In this section, basics of radiometry theory, infrared spectrum and infrared radiation are explained.

Radiometric concepts are necessary for a quantiative understanding of radiation transfer through a sensor. These concepts allow the analysis to determine how much energy is collected on the sensor detector surface.

11

2.1.1 Principles of Radiometry

Radiometry is the field of physics that addresses the measurement of electromagnetic flux transfer. It describes light at the geometrical optics level, where it travels as rays. Two important assumptions are made in radiometric analysis. The first one is that sources are incoherent, hence, interference can be neglected, and secondly, diffraction is ignored so that light travels in straight lines [28].

The *solid angle* is a parameter that must be discussed because many radiometric units are given with respect to solid angles. A solid angle, Ω, has units of steradians (sr) and is the angle subtended at the center of a sphere by an area on the surface of the sphere [28]. Depiction of solid angle is shown in Figure 2.1.
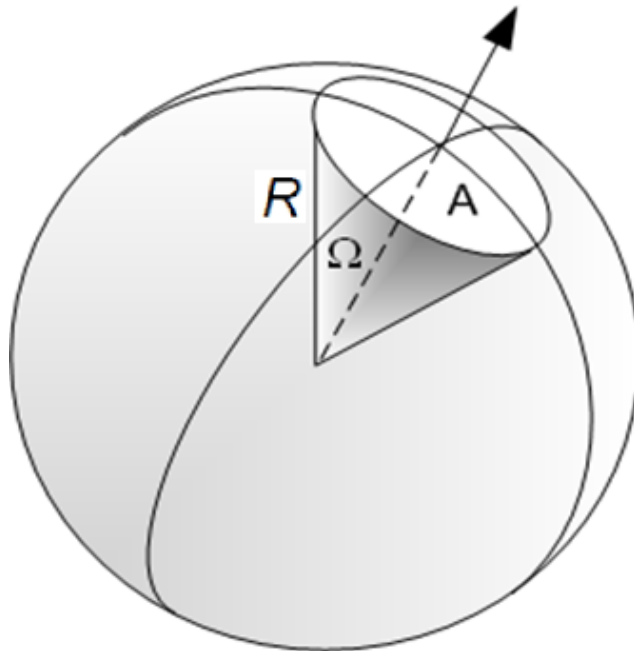
Figure 2.1: Solid angle description

The numerical value of a solid angle is a given area on the sphere surface divided by the square of the sphere radius in Equation 2.1.

$$\Omega = \left(\frac{A}{R^2} \right) \tag{2.1}$$

where A is obtained from the curved surface of the sphere. The maximum number of steradians on a spherical surface is $4\pi R^2 / R^2 = 4\pi$.

12

For the radiometric terms, a precise nomenclature is introduced by a base publication [29]. Table 2.1 gives the radiometric terms, unit dimensions and symbols of the radiometric definitions.

Table 2.1: Radiometric definitions

Radiant Flux	Φ	W
Radiant Intensity	$I = d\Phi/d\omega$	$W\,sr^{-1}$
Irradiance	$E = d\Phi/dA$	$W\,m^{-2}$
Radiant Exitance	$M = d\Phi/dA$	$W\,m^{-2}$
Radiance	$L = d^2\Phi/(dA\cos\theta d\omega)$	$W\,m^{-2}sr^{-1}$

The *radiant flux* is the basic unit in radiometry and also called as *radiant power*, Φ. Radiant flux specifies the amount of energy per unit time and measured in watts [W].

The *radiant intensity*, I, is the exitant flux per unit solid angle and is measured in watts per steradian [$W\,sr^{-1}$].

The *irradiance*, E, addresses the amount of power incident on a surface, while *radiant exitance* or *emittance*, M, addresses the power leaving from a surface, both have the same units of power per unit area [$W\,m^{-2}$]. If the surface reflects all incident light, absorbing and transmitting none, the total radiant exitance equals the total irradiance.

The *radiance*, L, is given as the source power per unit projected area per unit solid angle and measured in watts per square meter per steradian [$W\,m^{-2}sr^{-1}$]. It is also defined as the power emitted per unit surface area per unit projected solid angle. Figure 2.2 describes radiance.

Radiance is an important term in signature calculations since it represents the appearance of surfaces from the sensor. Radiance remains constant in a vacuum when it propagates along rays, hence it is a natural unit in ray tracing. In addition, all the other quantities can be derived from radiance. Moreover, radiance is a directional quantity. Note that the cone $d\omega$ hits the surface point at an angle. The cross-section of the surface is a differential area dA. If the ray comes from a grazing angle and the angle between the surface normal and the direction of exitant radiation is θ, then the
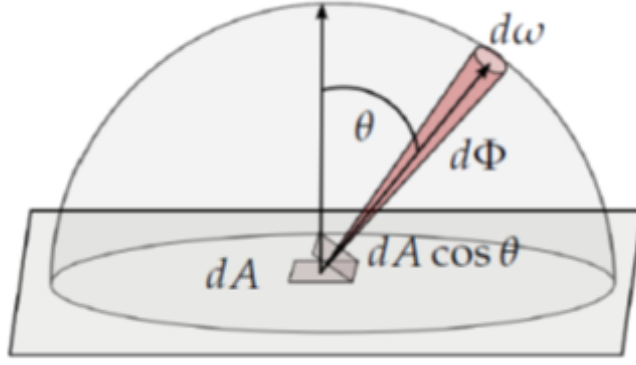
Figure 2.2: Radiance

term *projected area* stands for the area of the actual surface times the cosine of this angle θ.

Similarly the *projected solid angle* stands for the actual solid angle times the cosine of the angle θ. Here symbol ω is used to indicate a solid angle, and Ω is be used to indicate a projected solid angle. If $d\omega$ and $d\Omega$ are corresponding infinitesimal solid angles and projected solid angles respectively, then,

$$d\Omega = d\omega \cos \theta \tag{2.2}$$

In most cases, it can be required to integrate over solid angles or projected solid angles. It can be employed by double integration with the azimuth, ϕ, and zenith, θ, angles as shown in Figure 2.3. If X is the quantity to be integrated, we have,

$$\int_\omega X d\omega = \int_{-\pi}^{\pi} \int_0^{\pi/2} X \sin \theta d\theta d\phi \tag{2.3}$$

$$\int_\Omega X d\Omega = \int_{-\pi}^{\pi} \int_0^{\pi/2} X \cos \theta \sin \theta d\theta d\phi \tag{2.4}$$

Hemispherical Integration

For radiometric calculations, there is a requirement to integrate the incident irradiance, at a point on the model's surface, over the hemisphere to calculate the reflected

14
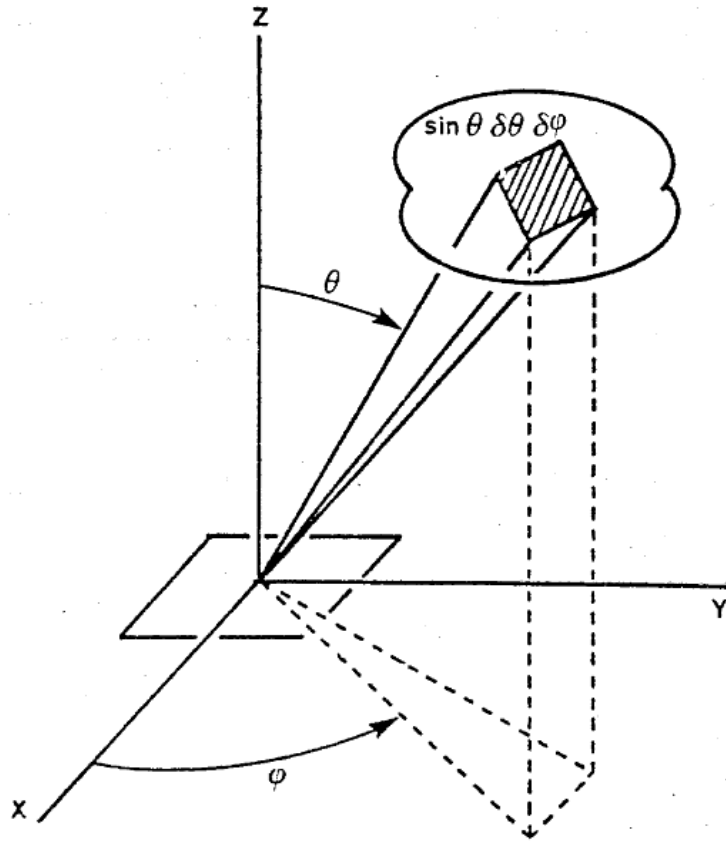
Figure 2.3: Azimuth and zenith angles

radiance in the direction of the observer. When numerically calculating a hemispherical integral, both domains are treated as if they are in cartesian form. Thus, the differential solid angle, $d\omega$, uses the *Jacobian transform* from spherical to cartesian coordinates. When integrating the BRDF over the hemisphere, the differential solid angle (centered on the direction θ),

$$d\omega_\Theta = \sin\theta d\theta d\phi \qquad (2.5)$$

transforms the spherical integral into a form, which the computer can calculate the equation as,

$$\int_\Omega f(\Theta)d\omega_\Theta = \int_0^{2\pi} \int_0^{\pi/2} f(\theta,\phi)sin\theta d\theta d\phi \qquad (2.6)$$

15

2.1.2   Infrared Spectrum

The infrared spectrum is a subset of the electromagnetic spectrum between visible radiation (light) and radio waves (millimeter and longer wavelengths) as shown in Figure 2.4 [30].

Figure 2.4: The electromagnetic spectrum

The electro-optics (EO) and infrared (IR) spectral sub-band regions are shown in Figure 2.5.

Spectral Band Designation	Nominal Wavelength Range (µm)	
UV	0.2 − 0.4	Reflective
Visible	0.4 − 0.7	
NIR	0.7 − 1.0	
SWIR	1.0 − 2.5	
MWIR	3.0 − 5.0	Reflective & Emissive
LWIR	8.0 − 12.0	Emissive
VLWIR	> 20.0	
Sub-mm	> 20.0	

Figure 2.5: EO-IR spectral region

As can be seen from the figure, in the midwave infrared bands, both the reflective and emissive properties are important, however, in the far infrared region the contribution due to reflected radiation is usually much smaller and the emissive radiations are dominant.

16

2.1.3 Infrared Radiation

The infrared energy was detected by *Sir William Herschel* in 1800 while doing experiment with a prism and sun light [30]. The main source of the infrared radiation is heat. Each object with temperature higher than absolute zero ($0°K$) is acting as an infrared source [28, 31].

In the infrared world, the absorption and the emission characteristics of objects and backgrounds are usually more significant than their reflection and transmission characteristics. This is especially true at night where solar reflection is not present. Daylight hours give solar reflections even in the infrared. However, many natural and human made objects are low in infrared reflectance and high in emissivity and absorptance [28].

All objects emit energy as a function of their temperature in the infrared portion of the electromagnetic spectrum. As an object gets hotter, it gives off more intense infrared radiation, and it radiates at shorter wavelengths. Infrared radiation from very hot surfaces can be detected by human eye since the wavelength of this emission is in the visible band range. This is called incandescence. For human eyes, the sensivity threshold is about $800°K$. But even at moderate temperature, the radiation can be detected as heat but not visible. Below a certain temperature, the thermal radiation is not in the visible wavelength range and can not be detected by the human eye, but the radiations are still present. Even at low temperature, such as room temperature, the objects radiate infrared energy with different wavelengths and intensities. Although, infrared energy is invisible to human eye, it can be detected with a thermal camera.

Kirchhoff Law

Radiant properties of a material are its ability to absorb, reflect and transmit optical radiation. The quantities that characterize these actions are absorptance (α), reflectivity (ρ) and transmissivity (τ). Emissivity describes the efficiency with which it radiates energy, absorptivity the efficiency with which it absorbs energy, reflectivity the efficiency with which it reflects energy and transmissivity the efficiency with which it transmits energy. Absorptance, reflectance and transmittance are not constant, they may vary with wavelength, temperature and angle [28].

17

Kirchhoff pointed out that under equilibrium conditions the sum of the absorbed, reflected and transmitted energy is equal to the incident energy. By the conservation of energy, the sum of all three properties must be equal to one at the same wavelength as all three are functions of wavelength [30]. So that one can write,

$$\alpha(\lambda) + \rho(\lambda) + \tau(\lambda) = 1 \tag{2.7}$$

Typically, the majority of solid materials are not transmissive in the infrared wavelengths [28]. If the body is opaque, the transmitted flux equals zero, and then the absorbed and reflected flux equals the incident flux. Hence, the relation reduces as,

$$\alpha(\lambda) + \rho(\lambda) = 1 \tag{2.8}$$

Materials and objects do not only absorb, otherwise their temperature would never cease increasing. They also loose heat, by a process of emission. The amount of energy emitted depends on the emissivity of the objects. Kirchhoff's law states that for a body to be in thermal equilibrium the absorbed equals the emitted energy [28].

$$\alpha(\lambda) = \varepsilon(\lambda) \tag{2.9}$$

Therefore, the above equation can be written as,

$$\varepsilon(\lambda) = 1 - \rho(\lambda) \tag{2.10}$$

That implies a higher emissive infrared sources has a low reflectivity characteristics [28].

Planck's Law and Blackbody Radiation

A blackbody is a theoretical object completely absorbing all incoming radiation in all wavelengths. Considering the energy conservation formula, a blackbody does not transmit nor reflect any part of the incident radiation. It is also an ideal emitter [26].

Blackbody radiation is that radiation that is released from bodies that are above the temperature of absolute zero. Two basic concept hold true for blackbody radiation. The first one is that a higher temperature body corresponds to a larger emission of

flux, and the second one is that a higher temperature body shifts the spectral radiation distribution towards shorter wavelengths. These concepts are true regardless of the emissivity characteristics of the body [28].

The *Planck's Law* describes the spectral distribution of the radiation from a blackbody at specific temperature, T, and wavelength, λ, which is usually written as [31].

$$M_{BB}(\lambda, T) = \frac{c_1}{\lambda^5 (e^{c_2/\lambda T} - 1)} \tag{2.11}$$

where, M_{BB} is the spectral blackbody radiant exitance in $Wm^{-2}\mu m^{-1}$, T is the absolute temperature in $Kelvin$, λ is the wavelength in μm, c_1 is the first radiation constant equal to $3.7418x10^8 \ Wm^{-2}\mu m^4$, c_2 is the second radiation constant equal to $1.4388x10^4 \ K\mu m$

Figure 2.6 [26] shows the emission spectrum of a perfect blackbody at a number of temperatures. Note the overall emittance, which is proportional to the area under the curve, increases rapidly with temperature and the wavelength of maximum spectral radiant exitance shifts towards shorter wavelength as the temperature increases. The individual curves never cross one another; hence the higher the temperature, the higher the spectral radiant exitance at all wavelengths.
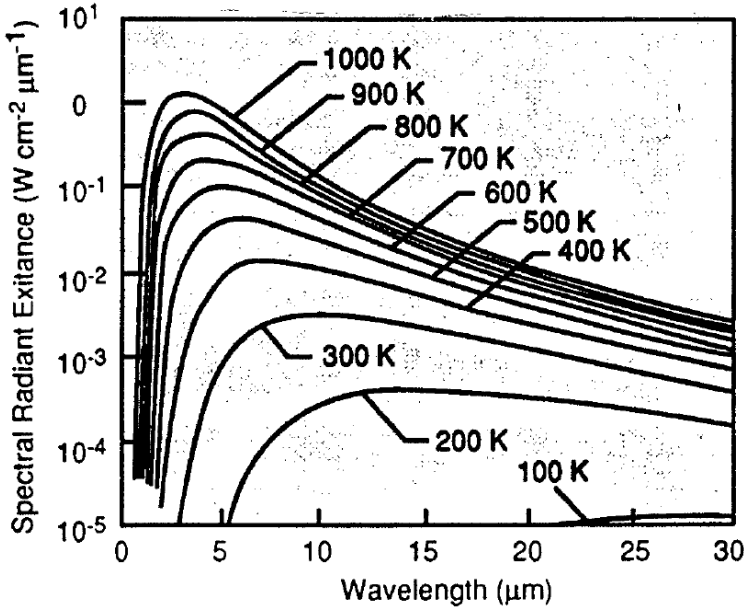
Figure 2.6: Spectral radiant exitance of blackbody at several temperatures

19

The peak wavelength of emisssion for a given blackbody temperature is given by *Wien's law* [28],

$$\lambda_{peak} = 2897.8/T \qquad (2.12)$$

where T is the temperature in $Kelvin$ and λ_{peak} is the peak wavelength in μm.

Since most objects in reality are not blackbody, the concept of emissivity is introduced to illustrate the level of correlation between real object radiation and blackbody radiation. *Emissivity*, $\varepsilon(\lambda)$, describes an object's emission characteristics; where a constant emissivity of one at all wavelengths, $\varepsilon(\lambda) = 1$, indicates a perfect blackbody radiatior.

Emissivity can be described in a number of ways, one of which is the spectral, hemispherical emissivity which defines as the ratio of the radiation of the given object at temperature T, to the radiation of the blackbody at the same temperature [28],

$$\varepsilon(\lambda) = \frac{M_{object}(\lambda)}{M_{BB}(\lambda)} \qquad (2.13)$$

Another representations of emissivity are average emissivity and total emissivity. The average emissivity is defined over a spectral region and the total emissivity refers to the emissivity over entire spectrum [28].

An object with a constant emissivity over all wavelengths is called a *graybody*. A graybody has a constant emissivity of less than one. Objects that emits as a function of wavelength, where they do not follow blackbody or graybody characteristics, are described as *spectral emitters* or *selective radiator* [31]. Figure 2.7 shows the spectral emissvity for a blackbody, a graybody and a selective radiator. A selective radiator as seen in Figure 2.7 has a value that is wavelength dependent.
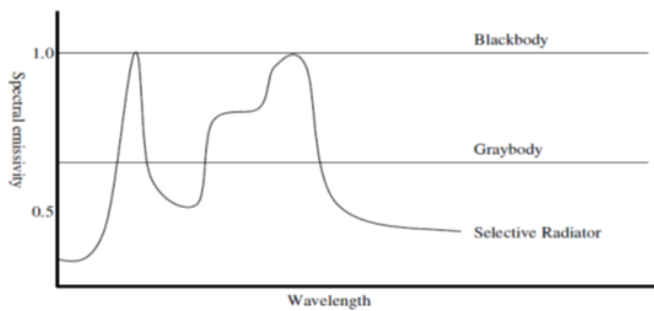
Figure 2.7: Spectral emissivity of three types of radiators

The spectral distribution and magnitude of an object's radiation are primarily a function of the object's temperature and emissivity. The spectral emittance of an object is [28],

$$M(\lambda, T) = \varepsilon(\lambda) M_{BB}(\lambda, T) \tag{2.14}$$

The total emittance within a spectral band is found by integrating the emittance over the appropriate wavelengths [28],

$$M(T) = \int_{\lambda_1}^{\lambda_2} \varepsilon(\lambda) M_{BB}(\lambda, T) d\lambda \tag{2.15}$$

where $M(T)$ is the total emittance in Wm^{-2} and λ_1 and λ_2 are the respective lower and upper wavelength limits.

Lambert Law

The radiant intensity emitted from a *Lambertian* surface is proportional to the cosine of the view angle and radiance is independent of the view angle. Blackbodies, graybodies, and the majority of spectral emitters can be considered as Lambertian sources. To Lambertian emitter, object radiance is not relevant to direction. Lambertian surfaces give a radiance that is directly proportional to its emittance. The total in-band radiance for a Lambert surface within a spectral band at a specific temperature T is found by [28],

$$L(T) = \frac{M(T)}{\pi} \tag{2.16}$$

where $L(T)$ is the total in-band radiance in $Wm^{-2}sr^{-1}$.

To sum up, the spectral emittance of a surface is described by Planck's law. Note that the surface emittance of an object depends on object temperature, wavelength and emissivity. Given that an object is viewed by a sensor with a limiting spectral bandwidth, the emittance of the object is integrated over the band to determine the object's emittance seen by the sensor [28].

2.2 Bidirectional Reflectance Distribution Function (BRDF)

The apparent radiance of a surface also depends on the orientation of the surface relative to the viewer and the radiation sources. Different surface elements of a non-planar object reflect different amounts of radiation towards an observer as a consequence of their differing attitude in space [32]. A surface cannot reflect more energy than it receives according to the law of conservation of energy.

The bidirectional reflectance distribution function (BRDF) was introduced by [29] as a unified notation for the specification of reflectance in terms of both incident and reflected beam geometry. The reflection properties of a surface are specified in terms of the BRDF. The BRDF is defined as the ratio of the reflected radiance dL_r in a particular direction (θ_r, ϕ_r) to the incident irradiance dE_i from direction (θ_i, ϕ_i). The BRDF is denoted by the symbol f_r and the units of the BRDF are inverse solid angle, sr^{-1}.

$$f_r(\theta_i, \phi_i, \theta_r, \phi_r, \lambda) = \frac{dL_r(\theta_i, \phi_i, \theta_r, \phi_r, \lambda)}{dE_i(\theta_i, \phi_i, \lambda)} \qquad (2.17)$$

where θ_i is the zenith angle of incident light, ϕ_i is the azimuth angle of incident light, θ_r is the zenith angle of reflected light, ϕ_r is the azimuth angle of reflected light, λ is the wavelength, L_r is the reflected radiance and E_i is the incident irradiance. Hence, BRDF is the function of incident angle, reflected angle and wavelength.

The geometry of the BRDF definition is shown in Figure 2.8. The BRDF allows one to obtain reflectance for any defined incident and reflected ray geometry simply by integrating over the specified solid angles [29].

The integral of the BRDF over all reflected angles provides the dimensionless *Directional Hemispherical Reflectance (DHR)*. Similarly, the integral of the BRDF over all incident angles gives the *Hemispherical Directional Reflectance (HDR)*. Because the BRDF is invariant under interchange of incident and reflected angles (*reciprocity*) the HDR and DHR are equivalent, and can be used interchangeably [29].
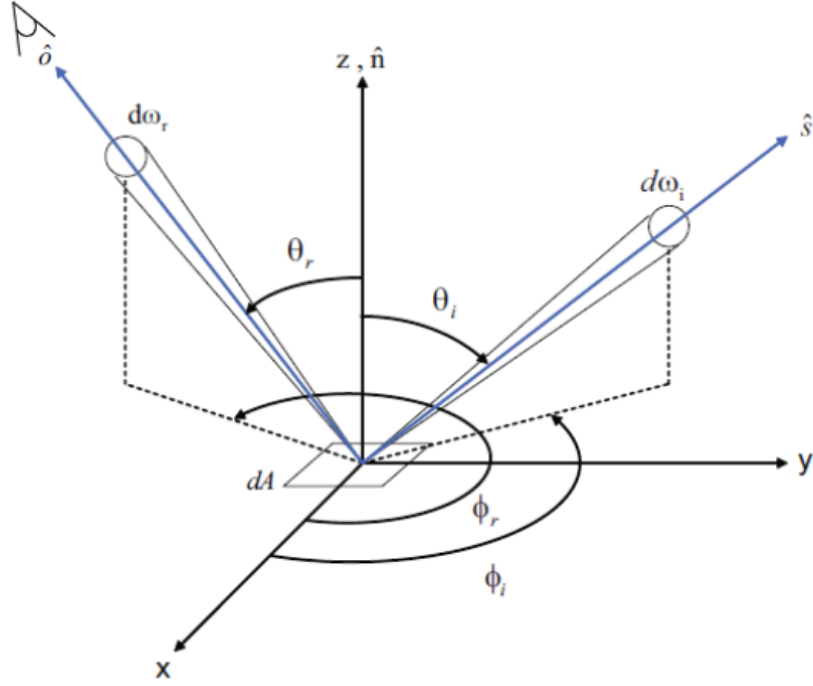
Figure 2.8: Hemispherical geometry of the BRDF

For such opaque objects, $\tau = 0$, spectral reflectivity can be obtained by the integral of the spectral BRDF.

$$\rho(\lambda) = \int_{\omega_r=2\pi} f_r(\theta_i, \phi_i, \theta_r, \phi_r, \lambda) \cos\theta_r d\omega_r \qquad (2.18)$$

$$\varepsilon(\lambda) = 1 - \int_{\omega_r=2\pi} f_r(\theta_i, \phi_i, \theta_r, \phi_r, \lambda) \cos\theta_r d\omega_r \qquad (2.19)$$

Thus, infrared spectral emissivity can be determined according to the spectral BRDF of the material surface.

2.2.1 Surface Reflectance Structure

The incoming light that strikes the surface of an object can be absorbed, reflected or transmitted. If the surface is flat and the material is homogeneous, the reflected light makes an angle with the local normal equal to the angle between the incident ray and the local normal. This is referred to as metallic or specular reflection. This kind of surfaces form virtual images of surrounding objects [32].

Many real world surfaces are not perfectly flat and thus scatter parallel incident lights into different directions. When deviations of the surface normals from the average are small, most of the lights lie near the direction for ideal mirror reflection and contribute to a surface shine or gloss. Moreover, other surfaces are not homogeneous and also scatter light rays which may emerge near the point of entry with several directions and contribute to flat, matte or diffuse reflection [32]. Figure 2.9 shows perfectly diffuse and perfectly specular surfaces.
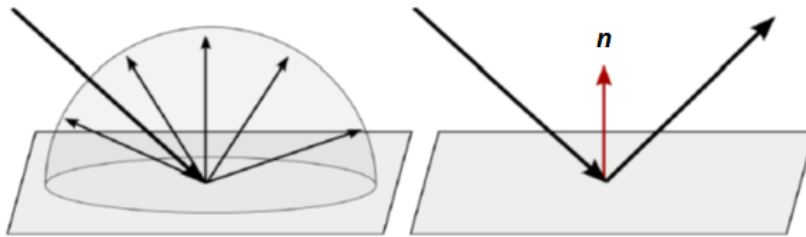
Figure 2.9: Perfectly diffuse and specular surfaces

In each case, the distribution of reflected radiation is dependent on the incident radiation direction and the structure of the object surface. If there is a symmetry, reflectance remains constant by rotating a surface about its normal. Many surfaces have this characteristics and this kind of surfaces enable an important degree of simplification of the analysis.

2.2.2 Perfectly Diffuse Reflectance

An ideal diffuse BRDF is the simplest material type and also called as *Lambertian*. A perfectly diffuse surface reflects the energy uniformly across the entire hemisphere, regardless of the incoming direction. The surface appears equally bright from all directions and reflects all incident energy [29]. Hence the reflected radiance, L_r, is isotropic, that is, it has the same value for all directions. Moreover, the integration of reflected radiance over the entire hemisphere must equal the incoming radiation. Hence, the BRDF for a diffuse surface, f_{rd} is constant and the irradiance equals the radiant exitance.

The radiant exitance can be found by integration of the reflected radiance, L_r, over the hemisphere [32],

$$M = \int_{\Omega_r} L_r d\Omega_r = L_r \pi \qquad (2.20)$$

From this equation, f_{rd}, the BRDF for a perfectly diffuse material is,

$$f_{rd} = L_r/E_i = L_r/M_i = 1/\pi \qquad (2.21)$$

2.2.3 Perfectly Specular Reflectance

A perfectly specular surface reflects and refracts light rays in one direction such that the exitant angle θ_r equals the incident angle θ_i. For example; a mirror surface has the characteristics of specular reflection.

Specular reflection is the most common reflectance type. It is the major assumption in ray optics and is the basis of the well known *Law of Reflection*. it requires that the angle of incidence equals the angle of reflection; this is the 2D definition. In 3D, the elevation angles for the incident and reflected rays must equal and the azimuthal angles must differ by π radians.

The reflected radiance of a surface patch in the direction (θ_r, ϕ_r) is simply the source radiance in the corresponding reflected direction [32]. That is,

$$L_r(\theta_r, \phi_r) = L_i(\theta_r, \phi_r + \pi) \qquad (2.22)$$

The surface thus forms a virtual image of the source. From the definition of the BRDF,

$$L_r = \int f_r dE_i = \int_{\Omega_r} f_r L_i d\Omega_i \qquad (2.23)$$

That is,

$$L_r = \int_{-\pi}^{\pi} \int_0^{\pi/2} f_r L_i \cos\theta \sin\theta d\theta_i d\phi_i \qquad (2.24)$$

This is called the double delta form of the BRDF for perfectly specular reflectance. Thus, f_{rs}, the BRDF for a perfectly specular material is,

$$f_{rs} = \delta(\theta_i - \theta_r)\delta(\phi_i - \phi_r + \pi)/(\sin\theta_i \cos\theta_i) \qquad (2.25)$$

25

2.3 Radiative Transmission through Atmosphere

The energy radiated from the object or source has to pass through the atmosphere before reaching the sensor. The infrared energy that propagates through the atmosphere experiences absorption and scattering due to the molecular and aerosol constituents. Absorption occurs spectrally as the infrared wavelength matches the various electronic, vibrational or rotational transitions for each molecule. Thus, the spectral transmission of infrared energy varies with wavelength as different molecules absorb the energy at various positions in the spectrum [26] as shown in Figure 2.10.
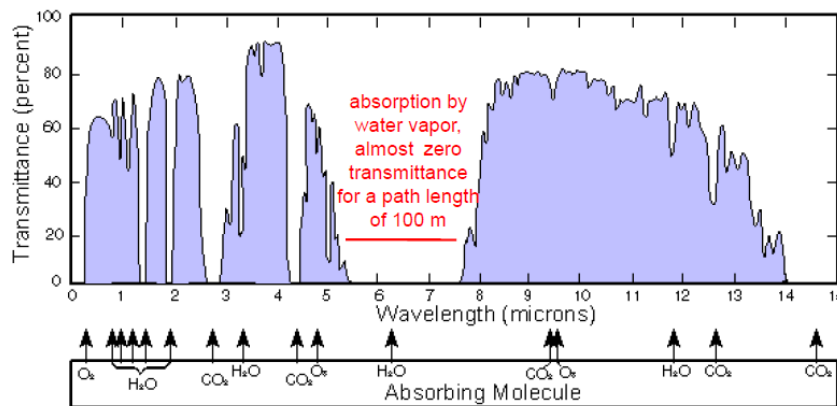
Figure 2.10: Molecular absorption bands in atmosphere

When designing a detection system, it is important to understand and exploit these spectral regions of high transmittance. High absorption bands can significantly reduce the system's detection range. In order to be used in a thermal imaging system, an infrared sensor must be able to sense the radiation in a wavelength interval in which the atmosphere does not considerably attenuate the radiation [28]. For this reason, systems are designed to detect in the short wave infrared (SWIR) $(1 - 3\ \mu m)$, MWIR $(3 - 5\ \mu m)$ or LWIR $(8 - 12\ \mu m)$ regions. The spectral regions through which the earth's atmosphere is transparent are called *atmospheric windows*.

The earth's atmosphere is a mixture of many gases and the existence of these gases in the atmosphere varies with altitude, time and space. Carbon-dioxide (CO_2), water vapours, ozone, nitrous-oxide and methane molecules are the key absorbers in the $2 - 15\ \mu m$ band even though they have very minor concentrations [26]. The existence of water vapours is highly variable from day to day, from season to season, with

altitude and for different geographical locations. Also, the CO_2 concentration varies seasonally and is high over vegetation and industrial areas as compare to over oceans and deserts. The variable nature of these atmospheric gases makes the prediction of atmospheric propagation at infrared frequencies a challenge [26].

2.3.1 Atmospheric Transmittance

The transmission of the atmosphere presents in between the scene and the sensor is calculated on the basis of the absorption, scattering and refractive-index. The absorption and scattering are usually grouped together under the topic of extinction which causes attenuation in the amount of radiant flux passing through the atmosphere. The transmittance of a path through the atmosphere can be approximated as,

$$\tau(\lambda) = e^{-\sigma(\lambda)x} \tag{2.26}$$

where τ represents the transmittance, σ is the extinction coefficient and x is the path length of the atmosphere. This principle is known as *Beer-Lambert Law* [28]. Under most conditions the extinction coefficient (σ) is made up of two components.

$$\sigma(\lambda) = \alpha(\lambda) + \gamma(\lambda) \tag{2.27}$$

where α is the absorption coefficient account for the absorption by the gas molecules of the atmosphere and γ is the scattering coefficient, accounts for scattering by small particles suspended in the atmosphere. In infrared region of the spectrum, the absorption poses a far more serious problem than does the scattering posses [31].

2.3.2 Atmospheric Path Radiance

As the atmosphere comprises of particles, they thermally emit radiation along the path in LOS of the source to the detector. The path radiance of the atmosphere may be calculated by considering atmospheric particles as blackbodies at a particular temperature. The path radiance becomes negligible as the path transmittance gets higher (closer to one). Therefore, with a cold clear sky, the path radiance can usually be neglected but at high temperatures it can cause noticeable effects [28].

27

2.4   Scene Simulation Basics

This section describes the basic topics of scene simulation. Some techniques used in scene simulations and generating synthetic images are discussed.

Computer Graphics is the art of creating realistic images on the computer.

Scene is a synthetic 3D representation of a set of objects in a virtual environment.

Rendering is the process of converting 3D geometric descriptions of graphical objects into 2D images.

Scene Simulation is the modeling and rendering of a scene. It includes geometric and radiometric modeling of all scene entities.

The aim of rendering algorithms is to generate realistic images that accurately capture the appearance of scene objects. Scene models include natural backgrounds such as terrain, ocean and sky, man made and natural objects such as buildings and trees.

The rendering process consists of solving the following pipeline of problems,

- Physical transforms of scene's surfaces to account for motion, rotations, etc.

- Projection of scene's geometric surfaces and volumes to 2D image

- Rasterization:

  - Converting projected polygons to image pixels

  - Determining which surfaces are visible at each image pixel

  - Determining the correct intensity for each image pixel

Two primary methods for projecting the scene to a 2D image and determining the visible surfaces,

- World space to screen space perspective projection in combination with z-buffer hidden surface algorithm.

- Reverse ray tracing, casting rays from eye position through image pixels into scene and gathering information from intersections.

28

Typically in computer graphics applications a simple pinhole camera perspective transformation is applied to transform 3D scene coordinates to 2D image coordinates.

OpenGL [2] is a software interface to graphics library originally implemented in SGI hardware. It provides an API routines that can be called from a C program. It is generally used with GPU cards for realtime performance.

2.5 Ray Tracing Algorithm

Ray tracing is a widely used scene generation algorithm that can produce realistic computer generated images. It is based on following the path of a ray of light through a scene as it interacts with and bounces off objects in an environment. Rasterization based methods have problems in simulating reflections and shadows. Ray tracing solves this problem by simulating the movement of light through the scene simulating a chosen set of light rays and it can cover characteristics of direct illumination, shadows, specular reflections and refractions through transparent objects accurately [33]. The ray tracing technique is computationally expensive and slow even for scenes with only moderate complexity.

In 1968, the first ray tracing algorithm was proposed by *Appel* for rendering solid objects [34]. The idea was to send rays from the camera through each pixel of an image plane, and find the closest intersection points. The process was stopped when the ray hit the closest object. This algorithm is known as *ray casting*. In 1979, *Turner Whitted* [35] pursued the idea further, by introducing recursion to enable reflective and refractive effects. Subsequent advances in ray tracing increased accuracy by introducing effects for depth of field, diffuse inter-reflection, soft shadows, motion blur, and other optical effects.

The common feature in ray tracing algorithms is that they compute the intersection points of 3D rays and a collection of 3D surfaces. In rendering applications, the optical properties of the point where the ray intersects the model determine what happens to the ray, e.g., it might be reflected, absorbed or refracted. Other applications might not care about information other than where the intersection happens, or even if an intersection occurs at all.

A virtual camera is defined with a location and direction. Then, rays are traced into a 3D scene geometry through every pixel on the screen. These rays represent the pixels on the resulting image. Figure 2.11 shows an example of ray tracing algorithm [33].
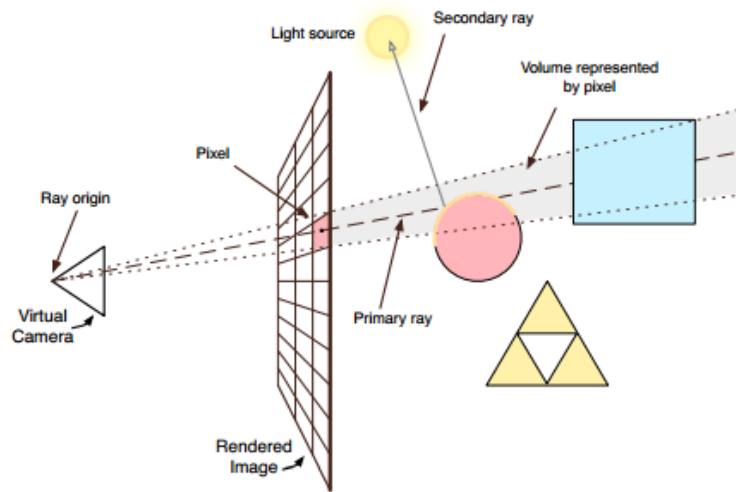
Figure 2.11: Ray tracing algorithm

The rays going from the camera to the objects in the scene are called primary rays. After a primary ray hits an object, the algorithm can spawn a set of new recursive rays that are going to simulate the different effects and behave like the original rays sent from the camera. These secondary rays can be used to find whether the point is in a shadow or not, by tracing a ray to the light sources in the scene. They can also be used to calculate reflections and refractions on the object, allowing us to draw accurate transparent objects such as glass or water. If a ray does not hit an object within a limited distance on its journey through the scene, a default colour or texture is returned and set as the colour of the given pixel. When all the rays have terminated either by hitting the scene walls or by reaching the maximum number of recursions, the rays and the surface colour are scaled, summed, and set as the pixel colour of the original pixel on the screen.

Ray tracing is often used when creating 3D-animated movies and have also in recent years become a valid option for use in real time graphics games like *Quake 3 and 4*. This is mainly due to the improvements done to graphic hardware and the massively parallel nature of the ray tracing algorithm. The research done on the subject has also played a significant roll in the progress and still new fields of research look into alternative use cases for ray tracing.

2.5.1 Ray–Surface Intersections

Ray tracing algorithm simulates the interaction of rays with geometry. Hence, the most basic operation is ray-surface intersection tests. One of ray tracing's nice features is that it is easy to support any geometric object that can be intersected with a 3D line. For example, it is straightforward to support spheres natively with no tessellation [36]. Spheres, cylinders, triangles and cubes are some of the common types of simple objects. However, the most important primitive is the triangle since complex models usually are built up from triangles. The most effective ray-triangle intersection test methods are based on barycentric coordinates [37].

The ray can fundamentally be described using Equation 2.28. A ray is defined by its origin $\mathbf{o}$ and direction vector $\mathbf{d}$, parameterized by a distance parameter t and $\mathbf{p}$ is the position along the ray at different distances. In these terms ray tracing is the problem of finding the values t where the ray intersect objects.

$$\mathbf{p}(t) = \mathbf{o} + t\mathbf{d} \tag{2.28}$$

The primary rays are generated by using a pinhole camera from the eye and sent to the pixels of the image plane. A more complicated camera model can simulate the depth of field.

2.5.2 Acceleration Structures

Since the ray tracing was first described in 1980 [35], the run time has gone from taking days to calculate down to potential real time rendering. A naive implementation of ray tracing tests a ray with every object in the scene for every pixel in the screen, making the algorithm very slow. Since complex scenes may contain millions of surfaces, this method becomes infeasible. *Turner Whitted* stated that he used up to 95% of the checking for intersections between rays and objects [35].

Execution of ray tracing is normally *sub-linear* in the number of objects. Hence, doubling the number of objects in the scene should less than double the running time. This is accomplished by organizing the objects into an acceleration structure that can quickly reject whole groups of primitives as not candidates for intersection with any

given ray instead of testing every primitive. Acceleration structures are an space subdivision hierarchies that are used for speeding up the traversal and intersection queries for ray tracing, especially for large scene databases.Two most commonly used acceleration structures are *bounded volume hierarchy* and *Kd-tree*.

There are many different types of acceleration structures, each with their own advantages and drawbacks. Furthermore, different scenes require different kinds of structures for optimal performance (e.g., static vs. dynamic scenes, generic primitives vs. triangles, and so on). The most common trade-off is construction speed vs. ray tracing performance, and extreme solutions exist on both ends of the spectrum. For example, a high quality kd-tree can take minutes to construct its acceleration structure. Once finished, though, rays can be traced more efficiently than with other types of acceleration structures, which in turn might be much faster to construct [36].

2.6 Parallel Processing on GPU

The aim of this section is to understand the importance and powerful features of modern graphics hardware. GPU is a single-chip processor designed to process mathematically intensive tasks and rasterize the huge amount of vertices and triangles at high frame rates. GPU is a manycore device that specializes on high execution throughput of parallel applications. A GPU mainly consists of an on-chip global RAM memory and an array of identical streaming multiprocessors (SM), each able to switch between hundreds to thousands of threads in almost no time. Most of its transistors are devoted to data processing. The GPUs performance stems from the SM ability to quickly launch and switch between thousands of threads.

GPU's are originally designed for graphics rendering and gaming industry. Using the massive power of the GPU is an emerging trend in high performance computing. The power and flexibility of GPUs makes them an attractive platform for general purpose computation. Example applications range from in-game physics simulation to conventional computational science.

A simple way to understand the difference between a CPU and GPU is to compare how they process tasks. A CPU consists of a few cores optimized for sequential

serial processing while a GPU consists of thousands of smaller, more efficient cores designed for handling multiple tasks simultaneously. For example, Intel I7 CPU has 4 cores and can execute 8 threads. GTX 680 GPU has 1536 cores and can execute 16384 threads.
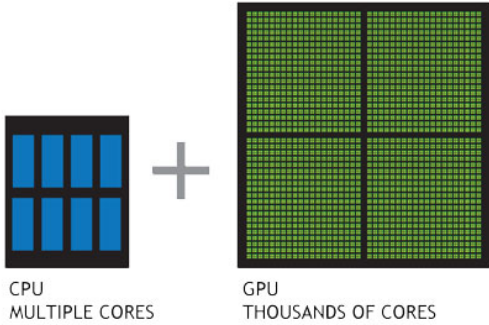
Figure 2.12: CPU vs GPU cores

Figure 2.13 shows the performance gap between CPUs and GPUs. Theoretical GFLOP/s for Nvidia GPU and Intel CPU architectures shows that the GPU performance has outgrown CPU performance. It is expected that the GPU will get even more powerful in the future.
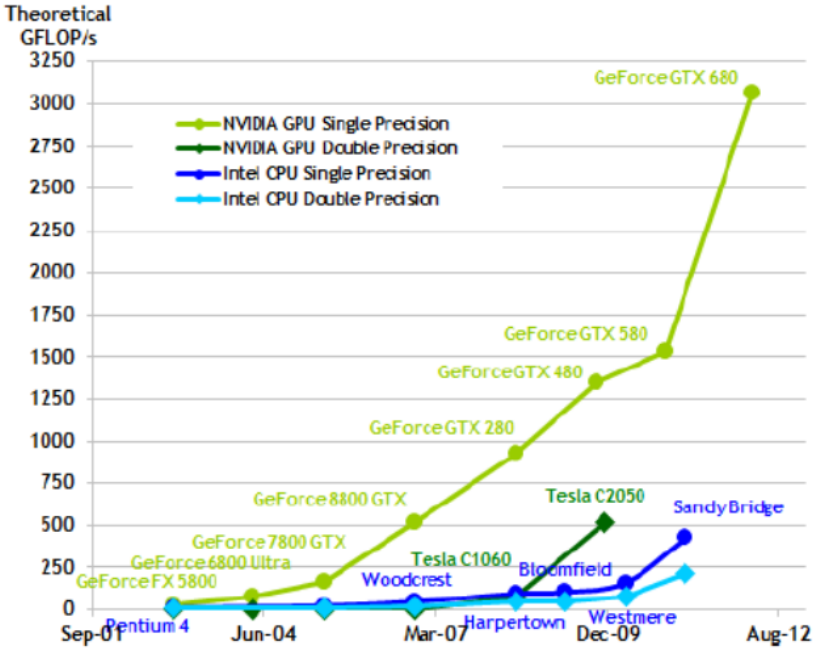
Figure 2.13: Theoretical GFLOP/s for Nvidia GPU and Intel CPU architectures

33

The GPU has also surpassed the CPU in number of transistors on the chip. For instance, the GK104 has 3.5 billion, while an Intel I7 Ivy Bridge has around 1.7 billion. The main difference between the GPU and the CPU is how the space on the chip is divided. The CPU has advanced branch prediction features, instruction level parallelism, and a sophisticated multi-leveled cache hierarchy to overcome the memory wall. These features take a lot of space on the die. Typical CPUs consist of $4-8$ cores with identical functionality and a multi-level cache. GPUs are simpler in their structure and are built up with more repeated logic. A GPU mainly consists of an on-chip global RAM memory and an array of identical SM, each able to switch between hundreds to thousands of threads in almost no time. Most of its transistors are devoted to data processing. The GPUs performance stems from the SM ability to quickly launch and switch between thousands of threads.

As a consequence, the GPU is perfectly suited for performing massive parallel calculations. However, the CPU's, are good at performing sequential calculations, input/output (I/O) and program flow. Applications designed to execute sequential part on CPU and numerically intensive part on GPU give the best performance.

2.6.1   Compute Unified Device Architecture (CUDA)

CUDA is a parallel computing platform and programming model invented by Nvidia in 2007 to support joint CPU/GPU applications. It is designed to utilize the power of the graphics processing unit for general purpose computations. CUDA allows the programmer to efficiently program in a manner similar to C to exploit the latest Nvidia graphics cards, so any users based on C developing can easily develop CUDA applications. In CUDA, parallelized programs are launched from a kernel of code. The code on the kernel is run on several thousands of threads. Individual threads run all of the code on the kernel, but with different data. CUDA arrange threads into thread blocks that can be one, 2D or 3D structures. Then all of thread blocks are organized into a one dimensional or two dimensional grid of blocks. The device (GPU) schedules blocks for execution on the multiprocessors in the order of their placement. The placement is determined by the user, and is specified when launching the kernel from the host (CPU) [3, 27, 38].

2.6.2   OptiX Ray Tracing Engine

GPUs are best at exploiting very high degrees of parallelism, and ray tracing fits that requirement perfectly. The Nvidia OptiX ray tracing engine is a programmable ray tracing framework designed for helping software developers build ray tracing applications on Nvidia GPUs and other highly parallel architectures. Since OptiX is built on CUDA GPU computing architecture, it is available for all systems which have a CUDA enabled GPU [36, 39, 40].

The core idea of the OptiX engine is that most ray tracing algorithms can be implemented using a small set of programmable operations. This is a direct analog to the programmable rasterization pipelines employed by OpenGL and Direct3D. The core of OptiX is a domain specific just in time compiler that generates custom ray tracing kernels by combining user supplied programs for ray generation, material shading, object intersection, and scene traversal. This enables the implementation of a highly diverse set of ray tracing based algorithms and applications, including interactive rendering, offline rendering, collision detection systems, artificial intelligence queries, and scientific simulations such as sound propagation [40].

OptiX employs a special purpose object model designed to minimize the constant data used by the programmable operations. In contrast to an OpenGL system, a language limited to rendering, or prescribed solutions with fixed data structures, the OptiX engine is extremely general. It enables developers to quickly accelerate whatever ray tracing task they wish, integrate it as needed, and run it on commonly available hardware [39].

The OptiX engine takes care of the *heavy lifting* associated with ray tracing, giving developers more time to concentrate on technique with relatively small programs that leverage the latest GPU advances. A single ray execution model makes building custom techniques straight forward, while state of the art acceleration structures, such as BVH and KD trees, cutting edge traversal algorithms, load balancing, recursion, parallelism across CUDA Cores and GPUs, out of core processing, and interop with OpenGL, Direct3D and CUDA applications for hybrid ray tracing rasterization applications, makes ray tracing development far easier than alternative approaches [39].

The ray tracing pipeline provided by OptiX contains several programmable components. Each of these programs are invoked on the GPU at specific points during the execution of a generic ray tracing algorithm. The combination of user programs and OptiX kernel code forms the ray tracing pipeline, which is outlined in Figure 2.14. Unlike a feed-forward rasterization pipeline, it is more natural to think of the ray tracing pipeline as a call graph. The core operation, *rtTrace*, alternates between locating an intersection (*Traverse*) and responding to that intersection (*Shade*). By reading and writing data in user-defined ray payloads and in global device memory arrays, these operations are combined to perform arbitrary computation during ray tracing [36, 40].
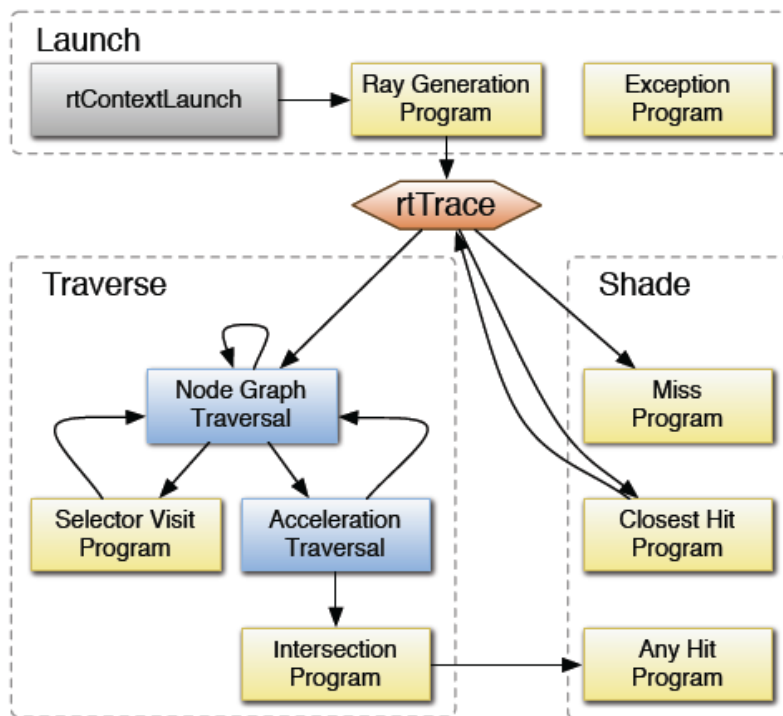
Figure 2.14: Optix ray tracing pipeline

A call graph in Figure 2.14 showing the control flow through the ray tracing pipeline. The yellow boxes represent user-specified programs and the blue boxes are algorithms internal to OptiX. Execution is initiated by the API call *rtContextLaunch*. A built-in function, *rtTrace*, can be employed by the ray generation program to cast rays into the scene. This function may also be called recursively by the closest hit program for shadow and secondary rays. The exception program is executed when the execution of a particular ray is terminated by an error such as excessive memory consumption.

There are eight types of programs:

Ray generation programs are the entry into the ray tracing pipeline, invoked by the system in parallel for each pixel or other user-defined work assignment. A single invocation of *rtContextLaunch* creates many instantiations of these programs.

Intersection programs implement ray-geometry intersection tests. As the acceleration structures are traversed, the system invokes an intersection program to perform the geometric query. The program determines if and where the ray touches the object and may compute normals or other attributes based on the hit position.

Bounding box programs compute the bounds associated with each primitive to enable acceleration structures over arbitrary geometry to optimize ray tracing performance.

Closest hit programs are invoked once traversal has found the closest intersection of a ray with the scene geometry. This program type closely resembles *pixel shaders* in classical rendering systems. Typically, a closest hit program performs computations like shading, potentially casting new rays and storing result data in the ray payload.

Any hit programs are called during traversal for every ray-object intersection. The any hit program allows the material to participate in object intersection decisions while keeping the shading operations separate from the geometry operations. It may optionally terminate the ray using the built-in function *rtTerminateRay*, which stops all traversal and unwind the call stack to the most recent invocation of *rtTrace*.

Miss programs are executed when the ray does not intersect any geometry in the interval provided. They can be used to provide a background color or implement environment maps.

Exception programs are executed when the system encounters an exceptional condition, e.g., when the recursion stack exceeds the amount of memory available for each thread, or when a buffer access index is out of range. They are useful for debugging and error reporting purposes.

Selector visit programs can be used to implement more sophisticated scene traversal schemes. For example, they can be used to implement a level of detail system where the distance to the object determines if a coarse or detailed model is used.

CHAPTER 3

INFRARED SIGNATURE MODELING

Signature prediction is an important part of infrared system analysis. Signature modeling and simulation provides a cost effective means to examine a wide range of scenarios. Due to the complexities of infrared signature computation many computer models have been constructed. An accurate infrared signature model requires understanding the relevant physics for the application and using the physical models.

This chapter describes the method, procedures and ideas that is implemented in Chapter 4. The background theory presented in Chapter 2 is expanded in detail and is focused towards the infrared signature modelling application. The chapter first describes the main components of the infrared signature model. Then, general infrared signature equation is explained. At the end of this chapter, spectral based and band-averaged based infrared signature models for the scene simulation are proposed.

3.1 Infrared Signature Components

The objective of this section is to provide a description of the factors affecting the infrared signature of a scene.

The infrared signature is the signal that is emitted, reflected or transmitted from an object surface across the whole infrared spectrum. The energy radiated from any object surface depends upon its property to absorb, reflect and transmit radiation. When absorption occurs, it produces heat and new radiation is produced called self-emission. The difference between visible and infrared wavelengths is that in visible scenes the

important parameters are the reflection and external source irradiance, whereas, the radiance from an object in the thermal infrared bands is due primarily to its body temperature and its surface material emissivity and reflectivity characteristics. The thermal environment of an object has also a major impact on its infrared radiance as a result of its temperature distribution.

In an infrared imaging system, the radiation received at the sensor comprises of thermal self-emitted radiations from the object and reflected radiations from the other sources in the environment. Thermal emission from the object corresponds to its temperature and emissivity. The sources of reflected radiations from all directions in the hemispherical environment consists of sun, sky and background; all of these are reflected in some part from the object towards the sensor. The infrared radiation is then attenuated as it passes through the atmosphere due to scattering and absorption. Additionally, the atmosphere itself provides a direct component. The atmosphere that is in the field of view of the sensor contributes through the path radiance to infinity and the path radiance between the sensor and object. The main components of the infrared signature model is given in Figure 3.1 [18].
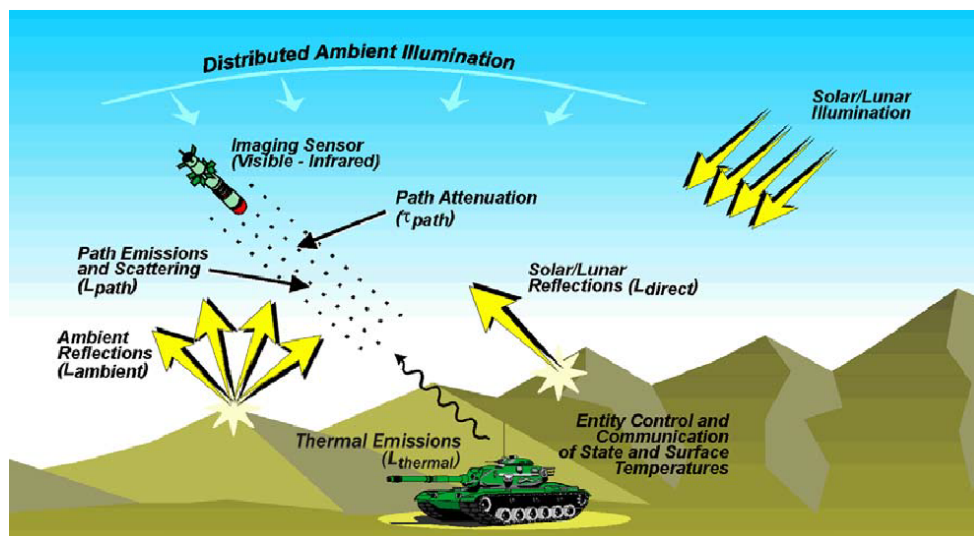
Figure 3.1: Main contributors to radiometric signature in an infrared scene

In the near and midwave infrared bands, both the reflective and emissive properties are generally equally important. For example, the sun is the important source of reflected radiation with a temperature of about $(6000°K)$ especially in the near infrared bands [28]. The solar irradiance on an object surface changes with a diurnal cycle.

Also, the earth and sky provide thermal emissions and also solar reflections in day time with scattering. However, in the far infrared region the contribution due to reflected radiation is usually much smaller and the emissive property of the object and background is dominant. The sources of infrared radiation on objects are mainly the hot surfaces and the high emissivity material skin in the far infrared region.

3.2 General Infrared Signature Radiometric Equations

The spectral radiance at the sensor from a surface in a specified direction and specified wavelength is given in general by an integral equation [41]. It is referred to as the *rendering equation* and it is considered as a fundamental equation in physics based rendering. The physical basis for the rendering equation is the law of conservation of energy. In this section the terms of that integral equation are defined. The integral equation then is used as the basis for the developed signature computation models which are proposed in the next section.

The key requirements for infrared signature rendering systems are [42]:

- Radiometric accuracy using physics based, spectral radiometric floating point calculation covering the spectral region of interest,

- Accurate object signatures, including self-emitted and reflected solar, background and sky radiance,

- Accurate spectral atmospheric path radiance and transmittance,

- Support for a variety of different and adverse environmental conditions,

- Accurate sensor spectral system response model,

- A full 3D virtual world defines geometrical model.

The radiance leaving a surface at each particular position, $\mathbf{x}$, direction, $\omega_{\mathbf{o}}$ and wavelength, λ, namely, $L_o(\lambda, \mathbf{x}, \omega_{\mathbf{o}})$, is the sum of the radiance emitted, $L_e(\lambda, \mathbf{x}, \omega_{\mathbf{o}})$, and the radiance reflected, $L_r(\lambda, \mathbf{x}, \omega_{\mathbf{i}}, \omega_{\mathbf{o}})$.

$$L_o(\lambda, \mathbf{x}, \omega_{\mathbf{o}}) = L_e(\lambda, \mathbf{x}, \omega_{\mathbf{o}}) + L_r(\lambda, \mathbf{x}, \omega_{\mathbf{i}}, \omega_{\mathbf{o}}) \qquad (3.1)$$

The emitted radiance is given by,

$$L_e(\lambda, \mathbf{x}, \omega_{\mathbf{o}}) = L_{BB}(\lambda, T)\varepsilon(\lambda, \mathbf{x}, \omega_{\mathbf{o}}) \tag{3.2}$$

where $\varepsilon(\lambda, \mathbf{x}, \omega_{\mathbf{o}})$ is the emissivity of the surface at position $\mathbf{x}$ for wavelength λ in outward direction $\omega_{\mathbf{o}}$ and $L_{BB}(\lambda, T)$ is the blackbody thermal emitted radiance for surface temperature T as given by the *Planck law* in Equation 2.11.

From the definition of the BRDF that the reflected radiance is given by the integral of the surface reflectance times the incident radiation over the entire incident hemisphere directions. Since BRDF is specified by the surface local coordinate system, and the incoming energy distribution is given in the viewer-oriented coordinate system, it is necessary to convert between two [29]. Incident and reflected directions from a location over the entire hemisphere is illustrated in Figure 3.2.
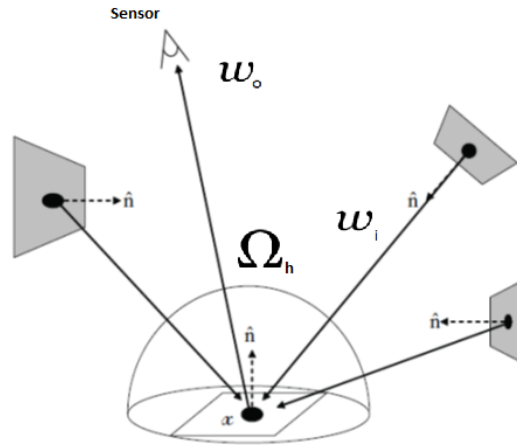
Figure 3.2: An illustration of the process of hemispherically integrating the irradiance on the surface, to calculate the reflected radiance in the direction of the sensor, from a point, $\mathbf{x}$.

The reflected radiance due to incident radiation from all directions is given by,

$$L_r(\lambda, \mathbf{x}, \omega_{\mathbf{i}}, \omega_{\mathbf{o}}) = \int_{\Omega_{\mathbf{h}}} f_r(\lambda, \mathbf{x}, \omega_{\mathbf{i}}, \omega_{\mathbf{o}}) L_i(\lambda, \mathbf{x}, \omega_{\mathbf{i}})(\omega_{\mathbf{i}} \cdot \mathbf{n}) d\omega_{\mathbf{i}} \tag{3.3}$$

where $\omega_{\mathbf{i}}$ is the negative direction of the incoming radiation and $\omega_{\mathbf{o}}$ is the reflected radiance direction, $\Omega_{\mathbf{h}}$ is the unit hemisphere containing all possible values for $\omega_{\mathbf{i}}$, $f_r(\lambda, \mathbf{x}, \omega_{\mathbf{i}}, \omega_{\mathbf{o}})$ is the surface reflectance which is expressed as the BRDF, the incident

radiation, $L_i(\lambda, \mathbf{x}, \omega_{\mathbf{i}})$, is from other sources in the entire hemisphere and $\mathbf{n}$ is the surface normal.

Combining two equations gives the general rendering equation for radiance leaving a surface,

$$
\begin{aligned}
L_o(\lambda, \mathbf{x}, \omega_{\mathbf{o}}) \;=\;& L_{BB}(\lambda, T)\varepsilon(\lambda, \mathbf{x}, \omega_{\mathbf{o}}) + \\
& \int_{\mathbf{\Omega_h}} f_r(\lambda, \mathbf{x}, \omega_{\mathbf{i}}, \omega_{\mathbf{o}})L_i(\lambda, \mathbf{x}, \omega_{\mathbf{i}})(\omega_{\mathbf{i}} \cdot \mathbf{n})d\omega_{\mathbf{i}}
\end{aligned}
\tag{3.4}
$$

By using zenith and azimuth angles, the integral equation 3.4 becomes,

$$
\begin{aligned}
L_o \;\; (\lambda, \mathbf{x}, \theta_r, \phi_r) =\;& L_{BB}(\lambda, T)\varepsilon(\lambda, \mathbf{x}, \theta_r, \phi_r) + \\
& \int_0^{2\pi} \int_0^{\pi/2} f_r(\lambda, \mathbf{x}, \theta_i, \phi_i, \theta_r, \phi_r)L_i(\lambda, \mathbf{x}, \theta_i, \phi_i)cos\theta_i \sin\theta_i d\theta_i d\phi_i
\end{aligned}
\tag{3.5}
$$

where θ_i is the zenith angle of incident radiation, ϕ_i is the azimuth angle of incident radiation, θ_r is the zenith angle of reflected radiation, ϕ_r is the azimuth angle of reflected radiation, $\cos\theta_i$ accounts for the *off-axis* angle between the incident radiation and the surface normal, $\sin\theta_i$ is from conversion of spherical to cartesian coordinates as explained in Chapter 2.

Equation 3.5 describes the radiance in the direction of the sensor at the object surface. However, the radiance arriving at the infrared sensor is directly affected by the atmospheric effects. Hence, the surface radiance must subsequently be modified to account for atmospheric effects along sensor view path to become at sensor radiance. The dominant physical quantities that constitute the atmospheric effects in the infrared band are the atmospheric transmittance and the path radiance. The incoming energy is attenuated by the atmospheric transmittance and path radiance is added on top of the attenuated radiation. Moreover, the radiance incident on the sensor is also affected by the sensor spectral system response. Hence, the spectral radiance incident on the sensor for a particular wavelength can be described as,

$$
L_s(\lambda, \mathbf{x}, \theta_r, \phi_r) = \left[L_o(\lambda, \mathbf{x}, \theta_r, \phi_r)\tau_a(\lambda) + L_p(\lambda)\right] S(\lambda)
\tag{3.6}
$$

where $\tau_a(\lambda)$ is the spectral atmospheric transmittance along the surface-sensor path and $L_p(\lambda)$ is the spectral path radiance due to scattered solar radiation and atmospheric self-emission.

The normalized spectral response of a sensor system, $S(\lambda)$, is determined by the response of the detector, $R_d(\lambda)$, the optical system, $R_o(\lambda)$, and possible filter elements, $R_f(\lambda)$, that can be introduced in the optical path [1]. The spectral response of the system is given by,

$$S(\lambda) = R_d(\lambda)R_o(\lambda)R_f(\lambda) \tag{3.7}$$

Equation 3.6 gives the incident spectral radiance on the sensor at a particular wavelength. The total incident in-band radiance of an object surface at the sensor is calculated by the integration of spectral radiometric equation over the particular waveband limits of the sensor.

$$L_t(\Delta\lambda, \mathbf{x}, \theta_r, \phi_r) = \int_{\lambda_1}^{\lambda_2} L_s(\lambda, \mathbf{x}, \theta_r, \phi_r)d\lambda \tag{3.8}$$

where λ_1 and λ_2 are the respective lower and upper waveband limits of the sensor, $L_t(\Delta\lambda, \mathbf{x}, \theta_r, \phi_r)$ is the total in-band radiance at the sensor.

3.3 Proposed Infrared Signature Models

For infrared imaging applications, radiometric signature calculation needs to include all significant radiation sources. The generation of high fidelity infrared images requires the implementation of the general infrared signature radiometric equations for each surface element in a sensor's field of view. The infrared imaging physical signature model describes the process of radiance transfer completely, however, it is a complicated process and requires extremely time consuming computations. Solving the rendering equation for any given scene is the primary challenge in realistic rendering. It is hard to apply in computer simulation because the following reasons:

- The full BRDF of material is hard to achieve,

- The integral over the hemisphere, $\mathbf{\Omega_h}$, is computationally expensive,

- The total in-band radiance at the sensor requires integrating over sensor system response spectra which also is computational expensive.

44

Therefore, to render the infrared scene in a computer program, the rendering equation needs to be applied special approximations to ensure radiometric validity while satisfying the necessary performance constraint. In traditional infrared signature modeling approaches, a simplified radiance equation model has been adapted to simplify these problems.

The basic building block of the proposed infrared signature scene model is the total incident radiance from each visible point in the field of view of the sensor. Surface materials are assumed as opaque. Hence, the radiance of surfaces hidden behind any other object do not reach the sensor provided the object obscuring the field of view.

For the proposed signature models, it is assumed that surface material optical characteristics can be represented in a combination of specular and diffuse components. Hence, a new parameter, represents fraction of radiance reflected specularly, F_s, is used to define material specular and diffuse characteristics. For example, if this parameter is equal to zero, then the surface material is assumed as perfectly diffuse and if it is between the zero and one, the surface material is assumed as a combination of both specular and diffuse. Under the specular and diffuse assumption, the reflection integral is not required to be evaluated as the BRDF is only non-zero when the incident and reflected zenith angles are equal and the azimuthal angles differ by 180 degrees and diffuse reflections are assumed lambertian that is reflecting equal radiance into all directions. This method is very fast to compute surface reflections than complex BRDF model.

For the reflected signature calculations, the incident radiance from the entire hemisphere, L_i, is split into three terms:

- Solar irradiamce

- Sky irradiance

- Scene background objects irradiance

Incident irradiance from the hemisphere reflects at object surfaces to become surface radiance. The spectral irradiance of the sun at earth terrain is modified by the transmittance and scattering of the atmosphere. The direct sunlight decreases with in-

creasing path length through atmosphere. The position of the sun has a strong effect on the scattered radiation in the solar radiation. Sky radiation in the infrared is caused by scattering of the sun radiation and by emissions from atmospheric constituents. The temperature of the atmosphere has a strong effect on the radiation in the termal infrared region [26]. The sky ambient radiation incident to the object surface comes from every direction. In many cases the incident radiance on a reflecting surface is not from the sky and sun alone. The surface can also be radiated from adjacent scene objects. External objects serve as secondary sources of radiation. The scene background objects reflection is provided by the ray tracer that accounts for object interactions and multiple reflections. Also, external illumination gives rise to multiple reflections within an object and shadowing effects.

3.3.1 Spectral Signature Model Radiometric Equations

In this section, proposed spectral signature model radiometric equations are explained in detail. The spectral radiance from a surface for a particular wavelength, $L_o(\lambda, \omega_\mathbf{o})$, is the sum of the thermal emitted spectral radiance, $L_e(\lambda)$, and the reflected spectral radiance, $L_r(\lambda, \omega_\mathbf{i}, \omega_\mathbf{o})$.

$$L_o(\lambda, \omega_\mathbf{o}) = L_e(\lambda) + L_r(\lambda, \omega_\mathbf{i}, \omega_\mathbf{o}) \tag{3.9}$$

The thermal emitted spectral radiance is computed as,

$$L_e(\lambda) = L_{BB}(\lambda, T)\varepsilon(\lambda) \tag{3.10}$$

where $\varepsilon(\lambda)$ is the hemispherical spectral emissivity of the surface for wavelength λ and $L_{BB}(\lambda, T)$ is the blackbody spectral radiance for surface temperature T.

The total reflected spectral radiance is considered as the sum of the spectral solar diffuse reflected radiance, sky ambient reflected radiance and scene background specular reflected radiance.

$$
\begin{aligned}
L_r(\lambda, \omega_\mathbf{i}, \omega_\mathbf{o}) \;=\; & L_{solar/diffuse}(\lambda, \omega_\mathbf{i}) + L_{sky/diffuse}(\lambda, \omega_\mathbf{i}) + \\
& L_{bg/specular}(\lambda, \omega_\mathbf{i}, \omega_\mathbf{o})
\end{aligned} \tag{3.11}
$$

46

where $L_{solar/diffuse}(\lambda, \omega_{\mathbf{i}})$ is the diffuse reflected solar spectral radiance at surface for the incident radiation direction $\omega_{\mathbf{i}}$, $L_{sky/diffuse}(\lambda, \omega_{\mathbf{i}})$ is the reflected sky ambient spectral radiance and $L_{bg/specular}(\lambda, \omega_{\mathbf{i}}, \omega_{\mathbf{o}})$ is the spectral background radiance reflected specularly.

The radiometric equation giving the reflected sky ambient spectral radiance is derived from the integration over the entire incident hemisphere,

$$L_{sky/diffuse}(\lambda, \theta_i, \phi_i) = \int_0^{2\pi} \int_0^{\pi/2} L_{sky}(\lambda, \theta_i, \phi_i)$$
$$(1 - F_s)\frac{\rho(\lambda)}{\pi}cos\theta_i \sin\theta_i d\theta_i d\phi_i \qquad (3.12)$$

where (θ, ϕ) is the angle of the incident of reflected radiation relative to the surface normal. All variables with subscript i are incident quantities while those with subscript r are reflected quantities. $L_{sky}(\lambda, \theta_i, \phi_i)$ is the incident spectral sky radiance from the hemisphere, F_s represents specular reflection ratio of the material and $\rho(\lambda)$ is the spectral hemispherical reflectance of the surface.

The solar diffuse reflected spectral radiance is defined as,

$$L_{solar/diffuse}(\lambda, \theta_i, \phi_i) = E_{solar}(\lambda, \theta_i, \phi_i)\tau_s(\lambda)cos\theta_i(1 - F_s)\frac{\rho(\lambda)}{\pi} \qquad (3.13)$$

where $E_{solar}(\lambda, \theta_i, \phi_i)$ is the spectral solar irradiance at the surface, $\tau_s(\lambda)$ is the spectral atmospheric transmittance coefficient along the sun-surface path.

For the special case of scene background specular reflections, $L_i(\lambda, \theta_i, \phi_i)$ is the incident spectral radiance from the hemisphere viewed in the direction $\omega_{\mathbf{i}}$. Incident background radiation could be from the sky, sun or scene objects. (θ_i, ϕ_i) is the incident specular direction complementary to the sensor view direction (θ_r, ϕ_r).

$$L_{bg/specular}(\lambda, \theta_i, \phi_i, \theta_r, \phi_r) = L_i(\lambda, \theta_i, \phi_i)F_s\rho(\lambda)\delta(\theta_i - \phi_r)\delta(\theta_i - \phi_r + \pi) \quad (3.14)$$

Proposed radiometric equations so far yield the spectral radiance in the direction of the sensor. Considering the spectral normalized spectral system response of the sensor and spectral atmospheric transmission with path radiance along the line of sight path between the surface and the sensor, the spectral radiance detected by the sensor is

computed as,

$$L_s(\lambda, \theta_r, \phi_r) = [L_o(\lambda, \theta_r, \phi_r)\tau_a(\lambda) + L_p(\lambda)] S(\lambda) \tag{3.15}$$

Finally, the total in-band radiance detected by the sensor for the spectral signature model is calculated by the integration of spectral incident radiance over the band limits of the sensor,

$$L_t(\Delta\lambda, \theta_r, \phi_r) = \int_{\lambda_1}^{\lambda_2} L_s(\lambda, \theta_r, \phi_r)d\lambda \tag{3.16}$$

where λ_1 and λ_2 are the waveband limits of the sensor,

3.3.2 Band-Averaged Signature Model Radiometric Equations

In some cases, the lack of exact radiometric calculation is not critical for the application and band-averaged signature modeling approach can be valid for the infrared imaging application. For this purpose, spectral signature calculation model is approximated by separating out the spectral variation of radiometry data and using band-averaged values for the sensor system response, atmospheric transmittance and material optical properties. Although ignoring the spectral dependency of the radiometric data is an incorrect signature calculation method and gives a result that includes a level of error, it is used frequently by many infrared scene simulation systems as can be seen from the literature review.

The developed signature model is based on the assumption that the surface material characteristics, atmospheric components and sensor effects vary slowly with wavelength, hence, the hemispherical spectral emissivity, reflectivity, spectral atmospheric transmittance and spectral normalized sensor system response values are moved outside of the spectral integral equation. From this point, the resultant radiometric equations for the proposed band-averaged signature model are explained in this section.

The in-band radiance from a surface for a particular waveband limits $\Delta\lambda$, is the sum of the thermal emitted in-band radiance and the reflected in-band radiance.

$$\hat{L}_o(\Delta\lambda, \omega_\mathbf{o}) = \hat{L}_e(\Delta\lambda) + \hat{L}_r(\Delta\lambda, \omega_\mathbf{i}, \omega_\mathbf{o}) \tag{3.17}$$

48

where $\hat{L}_o(\Delta\lambda, \omega_\mathbf{o})$ is the surface in-band radiance in direction $\omega_\mathbf{o}$, $\hat{L}_e(\Delta\lambda)$ is the in-band thermal emitted radiance and $\hat{L}_r(\Delta\lambda, \omega_\mathbf{i}, \omega_\mathbf{o})$ is the in-band reflected radiance.

The thermal emitted in-band radiance is computed as,

$$\hat{L}_e(\Delta\lambda) = L_{BB}(\Delta\lambda, T)\bar{\varepsilon}(\Delta\lambda) \tag{3.18}$$

where $\bar{\varepsilon}(\Delta\lambda)$ is the hemispherical band-averaged emissivity of the surface and $L_{BB}(\Delta\lambda, T)$ is the in-band blackbody radiance for surface temperature T.

The integration of spectral blackbody radiance, $L_{BB}(\lambda, T)$, over all wavelengths of interest gives the in-band blackbody radiance within that waveband.

$$L_{BB}(\Delta\lambda, T) = \int_{\lambda_1}^{\lambda_2} L_{BB}(\lambda, T)d\lambda \tag{3.19}$$

Band-averaged emissivity is calculated by integrating spectral emissivity values over the infrared band interval and dividing by the length of the interval.

$$\bar{\varepsilon}(\Delta\lambda) = \frac{1}{\lambda_2 - \lambda_1} \int_{\lambda_1}^{\lambda_2} \varepsilon(\lambda)d\lambda \tag{3.20}$$

The total reflected in-band radiance is defined as the sum of the in-band solar diffuse reflected radiance, sky ambient reflected radiance and scene background specular reflected radiance.

$$
\begin{aligned}
\hat{L}_r(\Delta\lambda, \omega_\mathbf{i}, \omega_\mathbf{o}) &= \hat{L}_{solar/diffuse}(\Delta\lambda, \omega_\mathbf{i}) + \hat{L}_{sky/diffuse}(\Delta\lambda, \omega_\mathbf{i}) + \\
&\quad \hat{L}_{bg/specular}(\Delta\lambda, \omega_\mathbf{i}, \omega_\mathbf{o})
\end{aligned} \tag{3.21}
$$

where $\hat{L}_{solar/diffuse}(\Delta\lambda, \omega_\mathbf{i})$ is the diffuse reflected solar in-band radiance at surface for the incident radiation direction $\omega_\mathbf{i}$, $\hat{L}_{sky/diffuse}(\Delta\lambda, \omega_\mathbf{i})$ is the reflected sky ambient in-band radiance and $\hat{L}_{bg/specular}(\Delta\lambda, \omega_\mathbf{i}, \omega_\mathbf{o})$ is the background in-band radiance reflected specularly.

The radiometric equation giving the reflected sky ambient in-band radiance is again derived from the integration over the entire incident hemisphere,

$$
\begin{aligned}
\hat{L}_{sky/diffuse}(\Delta\lambda, \theta_i, \phi_i) &= \int_0^{2\pi} \int_0^{\pi/2} L_{sky}(\Delta\lambda, \theta_i, \phi_i) \\
&\quad (1 - F_s)\frac{\bar{\rho}(\Delta\lambda)}{\pi}cos\theta_i \sin\theta_i d\theta_i d\phi_i
\end{aligned} \tag{3.22}
$$

49

where $L_{sky}(\Delta\lambda, \theta_i, \phi_i)$ is the incident in-band sky radiance from the hemisphere and $\bar{\rho}(\Delta\lambda)$ is the band-averaged hemispherical reflectance of the surface.

Band-averaged reflectivity is simply calculated from Kirchoff's law for opaque objects.

$$\bar{\rho}(\Delta\lambda) = 1 - \bar{\varepsilon}(\Delta\lambda) \tag{3.23}$$

The integration of spectral sky incident radiance, $L_{sky}(\Delta\lambda, \theta_i, \phi_i)$, over all wavelengths of interest gives the in-band sky ambient radiance within that waveband.

$$L_{sky}(\Delta\lambda, \theta_i, \phi_i) = \int_{\lambda_1}^{\lambda_2} L_{sky}(\lambda, \theta_i, \phi_i) d\lambda \tag{3.24}$$

The solar diffuse reflected in-band radiance is computed as,

$$\hat{L}_{solar/diffuse}(\Delta\lambda, \theta_i, \phi_i) = E_{solar}(\Delta\lambda, \theta_i, \phi_i) cos\theta_i (1 - F_s)\frac{\bar{\rho}(\Delta\lambda)}{\pi} \tag{3.25}$$

where $E_{solar}(\Delta\lambda, \theta_i, \phi_i)$ is the transmitted solar in-band irradiance at the surface.

The transmitted solar in-band irradiance is calculated by integrating the spectral solar irradiance with transmission of the sun-surface path over the specified band interval.

$$E_{solar}(\Delta\lambda, \theta_i, \phi_i) = \int_{\lambda_1}^{\lambda_2} E_{solar}(\lambda, \theta_i, \phi_i)\tau_s(\lambda) d\lambda \tag{3.26}$$

Specularly reflected scene background in-band radiance, $\hat{L}_{bg/specular}(\Delta\lambda, \theta_i, \phi_i, \theta_r, \phi_r)$, is computed as,

$$\begin{aligned} \hat{L}_{bg/specular}(\Delta\lambda, \theta_i, \phi_i, \theta_r, \phi_r) &= F_s L_i(\Delta\lambda, \theta_i, \phi_i)\bar{\rho}(\Delta\lambda) \\ &\quad \delta(\theta_i - \phi_r)\delta(\theta_i - \phi_r + \pi) \end{aligned} \tag{3.27}$$

where $L_i(\Delta\lambda, \theta_i, \phi_i)$ is the incident in-band background radiance for the specular direction and it is computed as,

$$L_i(\Delta\lambda, \theta_i, \phi_i) = \int_{\lambda_1}^{\lambda_2} L_i(\lambda, \theta_i, \phi_i) d\lambda \tag{3.28}$$

In order to calculate total in-band at sensor radiance for the band-averaged signature model, average atmospheric transmittance and in-band path radiance components

with band-averaged sensor sytem response are considered.

$$\hat{L}_t(\Delta\lambda, \theta_r, \phi_r) = \left[\hat{L}_o(\Delta\lambda, \theta_r, \phi_r)\bar{\tau}_a(\Delta\lambda) + L_p(\Delta\lambda)\right]\bar{S}(\Delta\lambda) \qquad (3.29)$$

where $\hat{L}_t(\Delta\lambda, \theta_r, \phi_r)$ is the total in-band radiance detected by the sensor for the band-averaged signature model, $\bar{\tau}_a(\Delta\lambda)$ is the band-averaged atmospheric transmittance, $L_p(\Delta\lambda)$ is the in-band path radiance and $\bar{S}(\Delta\lambda)$ is the band-averaged sensor sytem response.

The band-averaged transmittance in the waveband limits of the infrared sensor is computed as,

$$\bar{\tau}_a(\Delta\lambda) = \frac{1}{\lambda_2 - \lambda_1}\int_{\lambda_1}^{\lambda_2}\tau_a(\lambda)d\lambda \qquad (3.30)$$

where $\tau_a(\lambda)$ is the spectral atmospheric transmittance.

In-band path radiance, $L_p(\Delta\lambda)$, is computed from the spectral path radiance data using the equation,

$$L_p(\Delta\lambda) = \int_{\lambda_1}^{\lambda_2}L_p(\lambda)d\lambda \qquad (3.31)$$

Band-averaged normalized system response, $\bar{S}(\Delta\lambda)$, is calculated by integrating spectral system response over the infrared band interval and dividing by the length of the interval.

$$\bar{S}(\Delta\lambda) = \frac{1}{\lambda_2 - \lambda_1}\int_{\lambda_1}^{\lambda_2}S(\lambda)d\lambda \qquad (3.32)$$

CHAPTER 4

IMPLEMENTATION

In this chapter, the implementation of the proposed infrared signature models and scene simulation in OptiX are explained in detail. First of all, how the proposed infrared signature models are applied on scene simulation application is described. After that the implementation of the scene generation in OptiX is explained by introducing the flow chart of the algorithm. It is not the purpose here to describe the details of the rendering process. Instead the rest of this chapter focuses on the radiometric aspects of signature calculation and scene simulation in OptiX.

4.1 Implementing the Infrared Signature Models

To render an image frame, the developed system computes the total radiance arriving at each pixel on the sensor. The generation of high fidelity infrared images from a 3D model of scene geometry requires the following steps:

- Determine the objects that are in the sensor's field of view. These objects are normally described by a collection of 3D polygons. The number of polygons vary with the complexity of the object.

- Calculate the spectral radiance of each surface element in the scene. The radiance could include reflected and emitted energy. The reflected radiance can be from a source such as the sun, the sky or another background scene objects. The incident radiance into the sensor is influenced by the atmospheric path between the sensor and the surface element. The radiance is further influenced by

the material optical properties such as emissivity of the surface element. These parameters can be spectral dependent and vary as a function of wavelength. This implies that the radiance calculation must be carried out each wavelength of interest.

- Calculate the spectral atmospheric transmittance and spectral path radiance between the surface element and the sensor using a physics based accurate radiative transfer model.

- Calculate the total spectral incident radiance into sensor as the sum of the incident radiance from the surface element multiplied by the spectral atmospheric transmittance and add the spectral atmospheric path radiance.

- Multiply the spectral incident radiance at sensor with the sensor spectral system response and integrate the total spectral radiance over sensor infrared waveband to determine the total incident in-band radiance.

- Repeat the process for all the surface elements in the sensor's field of view. The surface elements could be from terrain, objects and sky background.

In this thesis work, infrared wavebands of primary interest are selected as $3 - 5\ \mu m$ for MWIR and $8 - 12\ \mu m$ for LWIR bands to cover typical infrared systems. These wavelengths correspond to windows in Earth's atmosphere where light propagates with less severe attenuation. Even in these two windows, the attenuation can be significant. The majority of infrared signature analysis work has been performed in these bands [28]. The selected infrared regions are divided into 128 spectral wavelength intervals for the spectral signature calculations, which gives sufficient accuracy.

4.1.1 Surface Material Model

Material optical properties of surfaces represent an important aspect of signature computation process. Ideally, the full BRDF is a high fidelity representation of a surface's reflectance properties; however, it is very complex and a full spatial and spectral characterization of the BRDF requires a significant data collection effort, and it produces a large volume of data. It also requires a large amount of processing power and memory.

Therefore, it is not feasible to calculate the reflection integral in rendering equation in run time process. Instead, most commercial visualization implementations use a simple specular and diffuse approximation in order to manage the optical database and simplify the computational requirements. Hence, the domain of the BRDF is significantly reduced an assumption of the diffuse and specular surfaces. This section describes the implementation of the surface reflectance model.

ASTER Spectral Library v2.0 is used to obtain measurement based physical hemispherical emissivity and reflectivity data [43]. More information about ASTER can be found in appendix A.

Specular materials have view angle dependency of reflected signature. For a specular reflector, the background radiance from the hemisphere is determines the reflected radiance. Also, the infrared energy can bounce from the specular surfaces and still remain significant. Figure 4.1 presents a sample scenario where the target is the ground, the house is the ground's background, and the tree is the house's background. When viewing the ground, the tree's radiance is a significant portion of the total radiation. It is shown by [44] that for temperatures near earth ambient, only a single bounce need to be considered significant whereas, for a hotter object, multiple reflection bounces may provide significant radiation.
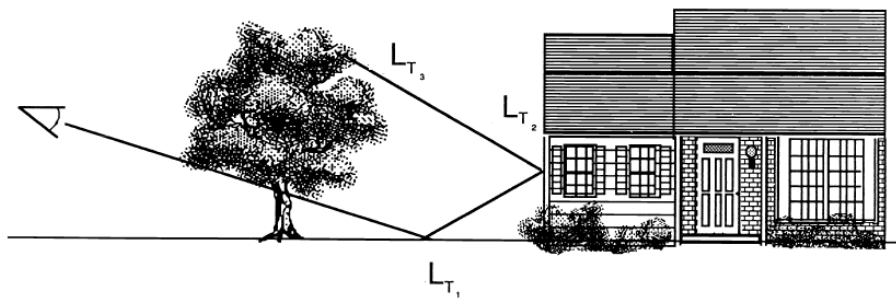
Figure 4.1: An illustration of multiple bounces for radiation propagation

4.1.2 Atmospheric Radiation Model

Atmospheric effects are one of the most important factors that affect the physical realism of the infrared scene. For high fidelity infrared signature modelling, the attenuation caused by the propagation of the infrared energy through the atmosphere and path radiance component due to particles in the atmosphere are to be considered. In this implementation, MODTRAN radiative transfer model is used to obtain radiometric data for the appropriate atmospheric conditions and path geometry.

MODTRAN® is a computer program designed to calculate atmospheric radiation transfer for wavelengths extending at modereate resolution from the thermal infrared through the visible and into the ultraviolet [45]. The MODTRAN program is a computationally rigorous radiation transfer algorithm that is used to calculate the spectral absorption, transmission, emission and scattering characteristics of the atmosphere. Modtran software is a currently accepted standart for atmospheric radiation transfer calculations. Atmospheric transmittance, path radiance, direct solar irradiance and sky radiance quantities are obtained from MODTRAN for spectral infrared wavelengths in this implementation. Appendix B gives more detailed information for MODTRAN software.

To obtain atmospheric data, meteorological input parameters such as air temperature, wind speed, aerosol model, air pressure, relative humidity, geographical location and time of day are required. Atmospheric path transmission and path radiance values are computed for the line of sight geometry as a function of sensor altitude, zenith angle of sensor view direction and distance between the sensor and object position.

During the scene simulation, the distance between the sensor and the object may change. Therefore, for each frame the atmospheric transmittance and path radiance values must calculated for the changing range. However, for the following reasons, atmospheric data cannot be computed in run time process. The main reason is that MODTRAN atmospheric model have slow calculation speed. Also, since MODTRAN is a commercial software it is not directly incorporated into the developed system. For these reasons, prior to runtime MODTRAN is applied to generate look up tables covering the line of sight geometry required and spectral band region of

56

interest at the beginning of simulation. Different look up tables need to be used for accommodating the different spectral characteristics and different geometries within the scenes of interest. Then the look up tables are placed in GPU memory and while in the process of run time simulation, the atmospheric data is extracted by linear interpolation from the GPU memory in according with relative geometry of object surface and sensor in the scene and applied to the radiance calculations on each frame. In order to maintain consistency, transmittance and path radiance values are defined in logarithmic space as a function of range due to fact that these quantities change linearly with range in logarithmic space. Hence, during the run time process, linearly interpolated transmittance and path radiance values are extracted accurately.

4.1.3   Thermal Emission Model

The thermal emission from a surface mainly depends on the thermal equilibrium temperature and spectral emissivity of the material. To calculate the thermal emitted radiation from a surface, these two parameters must be known. In traditional infrared scene simulation applications, temperature distribution is always regarded as known values or input parameter of the system for the demand of real time capability. Hence, it is introduced to the simulation as prior to the run time process. Blackbody spectral and in-band radiance values are computed as a function of temperature over the range of possible surface temperatures prior to run time stage by using Planck equation for the given spectral band of interest and transferred to GPU memory. During run time operation, blackbody radiance with material emissivity of the surface are used to calculate thermal emissions.

4.1.4   Reflected Radiation Model

Reflected radiation model is split into three distinct component. These are direct solar reflections, sky reflections and reflected radiations from the background objects in the scene.

Sky radiance map is obtained from MODTRAN software for the entire hemisphere as a function of view direction zenith angle. In thermal infrared bands azimuthal

57

dependency is not dominant as in visible band. Hence azimuthal dependency is ignored in this implementation. The hemisphere is divided into many regions and sky ambient radiance is computed at intervals of $3°$ for the interval of $0 - 90°$ in zenith angles. Then the reflected diffuse and specular sky ambient radiance from the surface materials are considered.

Moreover, secondary reflected radiations from the background objects for the specular materials are also computed.

Solar radiation is defined as an angle dependent spectral incident flux from the above extraterrestrial source at arbitrary locations within the scene. Solar position algorithm predicts the apparent angular position of the sun for arbitrary geodetic location, date and time of day [46]. The apparent zenith angle of the sun relative to the scene is then used as an input parameter to MODTRAN software to obtain solar radiation data. Then direct solar reflected radiance for the specular and diffuse surfaces is calculated. It is assumed that the sun illuminates the environment with parallel directional rays of light.

4.2 Simulating the Infrared Scene in OptiX

Since graphic cards have proven to be the most effective way to handle massively parallel problems, it is decided to use GPU for the infrared scene simulation in order to accelerate the calculations in this project. This is done by using the NVIDIA OptiX ray tracing engine for most of the heavy calculations. Total infrared signature calculation for each pixel is performed in parallel on GPU since radiance computation of each pixel is totally independent from any other pixels. Hence, threads are divided by all the image pixels and then tracing of the rays are implemented in a parallel fashion.

As a part of the project, an infrared scene generator is implemented using C++ object-oriented structure with Microsoft® Visual Studio 2010 IDE and compiler. The rendering engine is implemented using the OptiX framework version 3.0.1. In order to analyze and compare the simulation results, MATLAB® is used.

58

To describe its core functions, the developed infrared scene generator contains:

- Ray tracer based scene generation executed on GPU in a parallel fashion,

- Capable of simulating real time scenes of MWIR and LWIR spectral wavebands,

- OpenGL-CUDA interoperability in order to render the ray traced scene to OpenGL pixel buffer object and then display infrared images on the screen with configurable settings,

- Acceleration techniques provided by OptiX engine to optimize ray tracing algorithm,

- Interactive mouse and keyboard user-interactions to move and rotate the camera allowing the scene to be viewed at different perspectives,

- Reading radiance value of the pixels by simply clicking mouse,

- Contrast adjustment, image resolution resize, pixel radiance information,

- Diffuse and specular reflections,

- Anti- aliasing effect and false color representation,

- Taking screenshot of infrared scene and saving as *ppm* file,

- Object-oriented structure, making it simple to extend the renderer with new materials or geometry by writing the corresponding OptiX programs.

- GPU based two infrared signature model implementations which are spectral and band-averaged signature models,

- A number of different object geometry types such as sphere, cube, plane, triangle,

- Loading of custom geometry scenes from *obj* standart format. Most 3D geometry modeling tools can export to obj format.

59

In order to visualize the calculated infrared signature values on the screen, a linear mapping approach is used. Radiance values are converted into gray-scale color values that are in $[0, 1]$ interval. The color value of each pixel of the image is computed as,

$$C_t = \frac{L_t - L_{\min}}{L_{\max} - L_{\min}} \tag{4.1}$$

where C_t is the total color value in $[0, 1]$ interval, L_t is the total radiance value which is calculated from the signature model and the interval $[L_{\min}, L_{\max}]$ defines the respective minimum and maximum radiance limits.

Several examples of infrared scenes generated within the implementation are shown in Figure 4.2 and 4.3, respectively. The first figure shows the rendering result of a complex scene, in which there are many objects have different geometry, material, temperature distribution on a terrain plane and sky background. This figure shows gray-scale representation of the scene where black regions represent minimum radiance values and white regions represent maximum radiance values. Then, the false color representation of this scene is given in the next figure. In this figure, red regions indicate higher radiance values and blue regions represent lower radiance values.
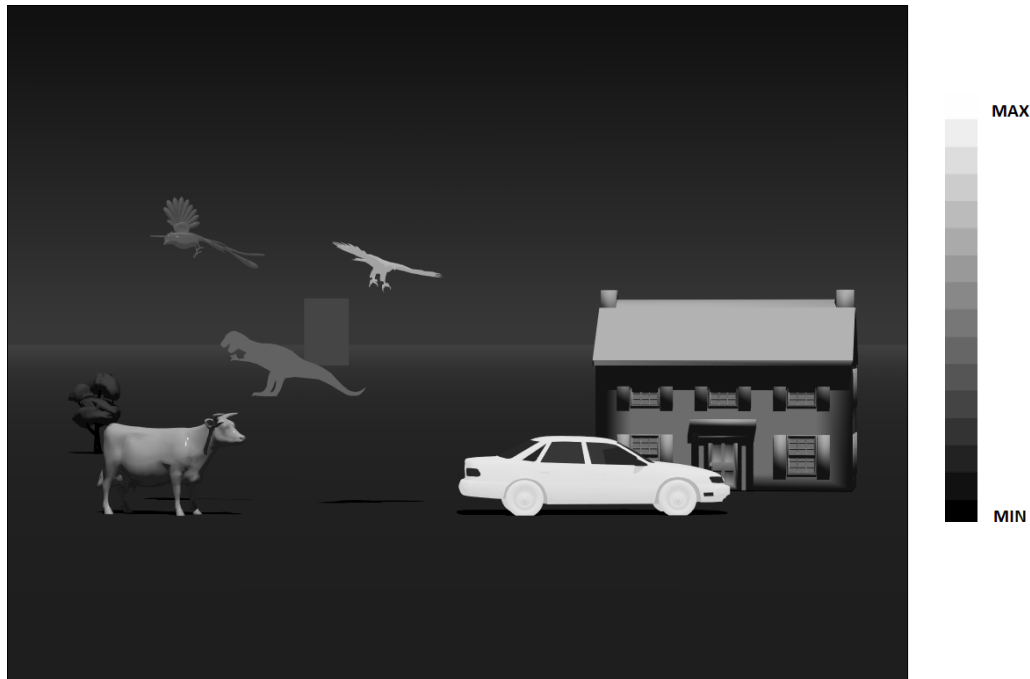
Figure 4.2: A screenshot of infrared scene implementation
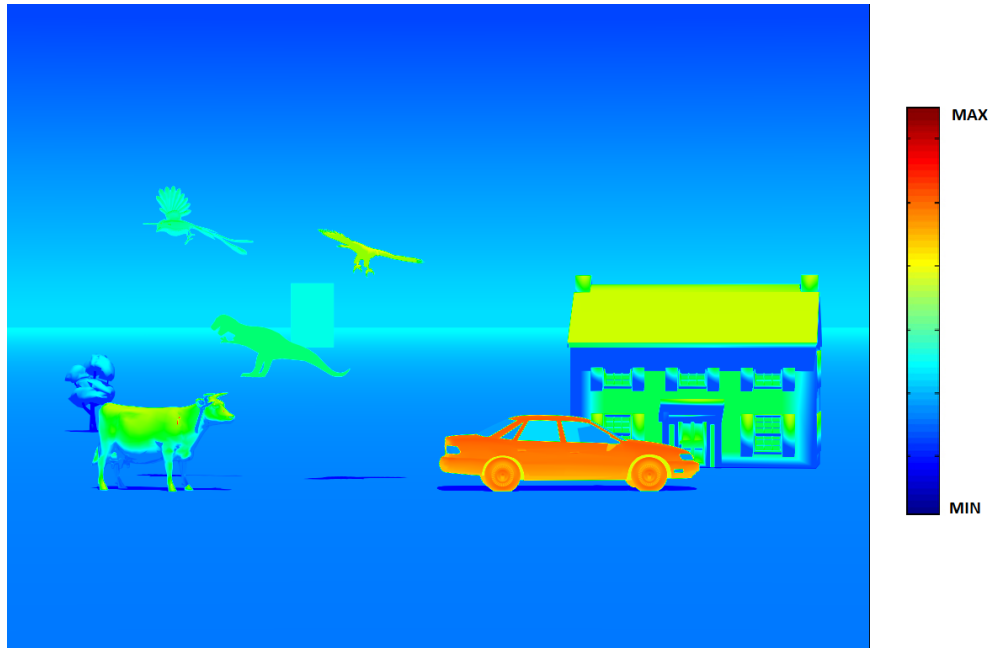
Figure 4.3: False color representation of infrared scene radiance

4.2.1 Scene Simulation Flow Diagram

Nvidia OptiX ray tracing architecture is used to perform infrared scene simulation on GPU due to its capabilities and flexible to program as generic ray tracing engine. Ray tracing algorithm is used to determine which surfaces contribute radiance to each pixel in a synthetic image. In this implementation, the ray tracer took the form of a traditional *back tracing* architecture, in which the ray propagation direction is opposite of the radiation flow. Each initial ray is cast in parallel outward from the position of the sensor, and upon hitting a surface, secondary reflection rays may be generated according to surface material characteristics. These secondary rays may then propagate to other surfaces, at which the same process can occur recursively.

The following works are done before simulating the infrared scene. Firstly, surface temperature distribution of 3D geometrical models are assigned. Then physical material of the 3D geometry is specified to determine emissivity and reflectivity parameters. After that spectral region of infrared sensor is selected as MWIR or LWIR. Also atmosphere conditions are defined and radiometric data are obtained from MOD-TRAN prior to simulation. The background is implemented as a combination of terrain with clear sky dome. The terrain is considered as a uniform plane of constant

temperature and material. Finally, the ray tracing method is applied to construct infrared imaging simulation system which can generate the synthetic infrared images of a 3D scene.
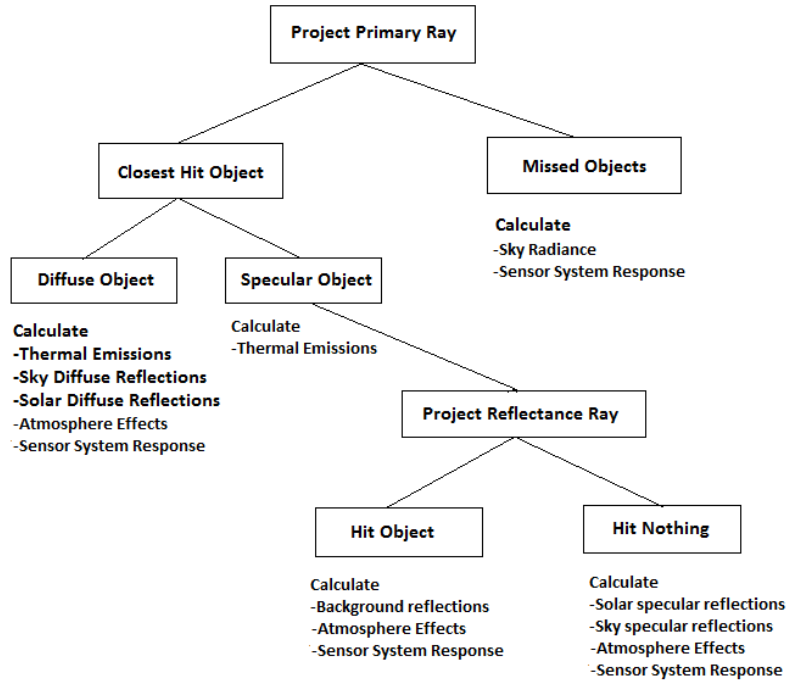
Figure 4.4: The flow chart of the algorithm

Solution of the signature equation starts with projection of a primary ray backwards from the sensor representing the flux path. After the scene geometry is ray traced, the values of the surface material as emissivity, reflectivity and specular reflection ratio, blackbody radiance, sensor view direction and the surface normal are available at each pixel. Rays which escaped the scene geometry are assigned to the sky radiance in that direction, while rays which hit self emitting surfaces have this emitted radiance added to the ray radiance. The reflected radiance is partially deduced from the sun and sky. If it hits a diffuse object, the reflected diffuse radiance from the sky and sun are calculated. If the object has a specular property, a secondary reflection ray is projected. The ray tracer also accounts for multiple reflections between objects surfaces within a scene. If that secondary ray hits an object, then contribution from this background object is calculated. However, if the secondary ray does not hit an object, the sky and sun reflected radiance are calculated. Atmospheric effects are also taken into account when tracing all of the rays. Atmosphere attenuates the composed radiance

(self emitted radiance + reflected radiance), along the path between the surface and the sensor. The atmosphere also itself emits a radiation. In the end, all contributions from the branches of a given sensor ray casting may be appropriately back summed to yield its final perceived radiance. For the spectral signature model, a spectral array of radiance is associated with each ray, so that these sums would be performed independently for each spectral wavelength. Total in-band at sensor radiance is calculated accounting for both the atmospheric transmission and path radiance, including the emissive and reflective contributions and sensor system response. The basis of ray tracer based radiometric calculations is sketched in Figure 4.4.

4.2.2 Camera Model

An infrared sensor system is usually composed of several components such as opto-mechanical elements, detectors and filters. For this implementation, the sensor model includes field of view, screen resolution and system response waveband limits parameters. The field of view for the infrared sensor is selected as $10°$ for both horizontal and vertical along with the image size. Modulation transfer function and noise model effects are out of scope for this work. Camera has 4-Degree of freedom for movement. It cannot perform roll and pitch movement in order to limit geometry of atmosphere data but it can change position in all axes and can perform yaw rotation. Hence, depending upon the sensor view angle or eye space, the 3D scene geometry is projected onto a 2D image plane.

4.2.3 Scene 3D Geometry Model

To visualize the infrared signature of a scene, it is essential to first model the geometry of the entire scene from the sensor viewpoint. The scene objects are positioned in a simple background comprised of a terrain and a sky dome. The geometrical shape of the scene objects is described in terms of a 3D surfaces a set of polygons. All the scene geometry are generated in local space and then transformed into the world space with respect to other objects. The movement of these objects in world coordinates could be done by using ray surface intersections equations.

The description of the scene objects geometry is required to develop a signature model. In this implementation, the primitive element for defining object geometry is a surface that can be represented with a mathematical equation for ray surface intersection tests. For example, a sphere geometry can be defined with a center point and radius. A triangle can be defined as a series of vertex points. Each object surface has a normal vector that is used for radiance calculations. In addition to simple geometrical surfaces such as sphere, plane and cube, triangle based mesh geometry models are used. Mesh based geometry models are formed by grouping many triangle surfaces into a smaller number of *patches*. The number of triangles is arbitrary, and depends on object geometry complexity, however, the more triangles, the better the approximation of the real object geometry. This triangle based *facet* approach is more commonly known as a *wire-frame model*. An example of wire-frame model is given in Figure 4.5.
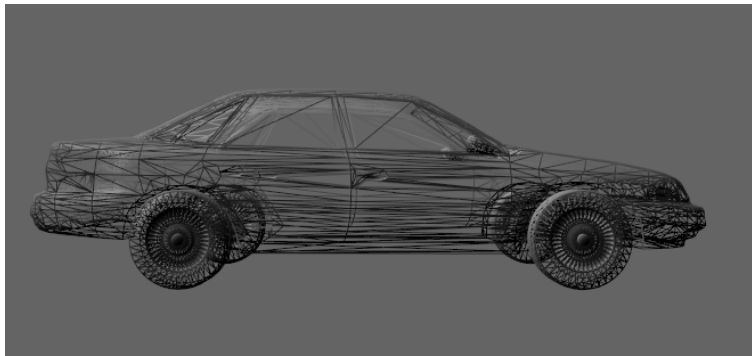
Figure 4.5: Car wire-frame model

There are many formats used to represent the scene object geometry from commercial computer aided design (CAD) packages and other data sources. In this implementation, the geometry loader currently handles the *Wavefront OBJ* file formats [47] which is a widely used format for representing mesh based geometric objects but could easily be extended to other formats. These obj files can be generated from 3D geometry modeling tools. Furthermore, for higher-fidelity modelling, the object geometry models are divided into parts based on geometrical shape, temperature characteristics and surface material radiometric properties. For example; a car comprising of hot metal parts, comparatively cold skin and glass canopy. All these parts have different temperatures and different radiometric properties and may behave differently in the infrared band.

CHAPTER 5

SIMULATION AND ANALYSIS RESULTS

This chapter presents simulation and analysis results which are obtained during this thesis. First section introduces the system requirements to run the infrared scene simulation software and simulated test scenes which are created to investigate the performance and signature analysis results. Also, screen shots of these infrared test scenes are shown. Then, radiometric data used for infrared signature modeling are presented with figures in the next section. Finally, last section explains and discusses the signature and performance analysis results of the infrared scene simulations.

5.1   Simulated Test Scenes

A variety of test scenes are defined to evaluate the results of the proposed infrared scene simulation under different conditions. Some of the test scenes have very simple scene geometry to analyze the effects of the signature models. To analyze the performance of the scene simulation, more complex scene geometries are created. The signature test scenes are created to represent the scene geometries which are used for the analysis of the spectral and band-averaged signature models. However, the performance test scenes indicate the scene geometries which are used for the performance analysis of the GPU based infrared ray tracer simulation.

Developed system requires the following hardware and software specifications. The system could run on a standard PC with OpenGL compatible CUDA enabled Nvidia graphics accelerator. The software requirements are Microsoft® Windows 7 64 bit operating system, OpenGL, GLUT and OptiX libraries.

Three signature test scenes are described below and rendered images are shown as Figure 5.1.
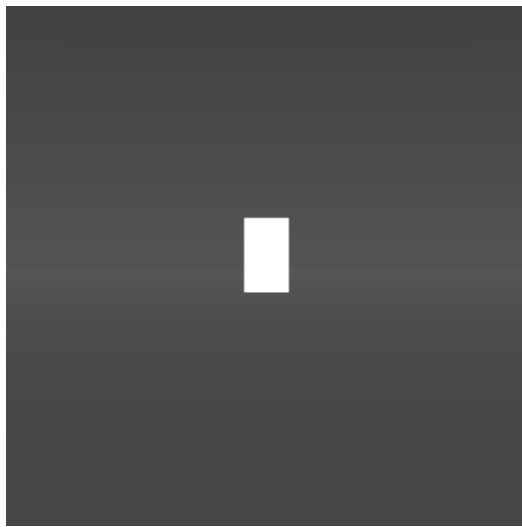
(a) Signature Test Scene 1
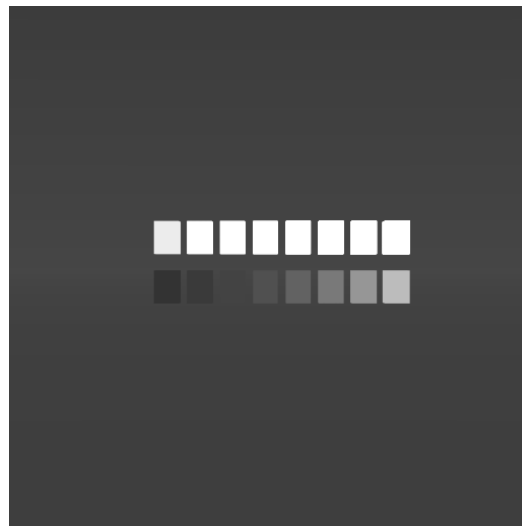
(b) Signature Test Scene 2

(c) Signature Test Scene 3

Figure 5.1: Signature test scenes

Signature Test Scene 1 in Figure 5.1(a) comprises of a cube with a terrain plane and clear sky background. All surfaces of this cube are assigned same temperature and blackbody material. Since cube is a simple and symmetric flat geometry, it is used in signature analysis of atmosphere and temperature effects at different distances from the camera. The simplicity of the *Signature Test Scene* 1 is made it suitable for the signature analysis of the atmospheric effects.

Signature Test Scene 2 in Figure 5.1(b) is another scene, contains a number of different cubes in addition to *Signature Test Scene* 1. Each of these cubes has different temperature but same blackbody material to analyze the effect of the temperature on infrared signatures.

Signature Test Scene 3 in Figure 5.1(c) consists of a house which have more complex geometry and surface normals, making it more suitable for the reflectance analysis. This house has a diffuse reflective material and it is placed on the terrain plane. Sky background radiations and solar reflected radiations are also considered in this test scene.

In addition to proposed signature test scenes, a number of different test scenes are applied on developed infrared scene simulation system in order to test the rendering performance. Four performance test scenes are described below and shown as Figure 5.2.
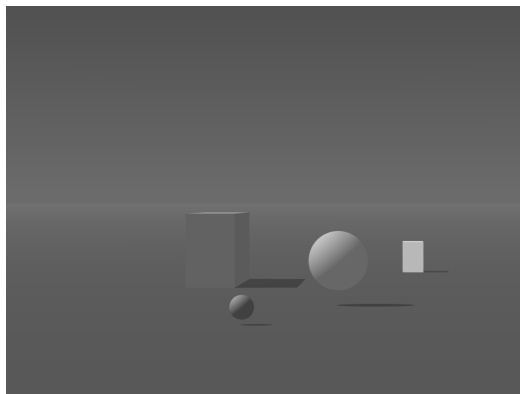
(a) Performance Test Scene 1
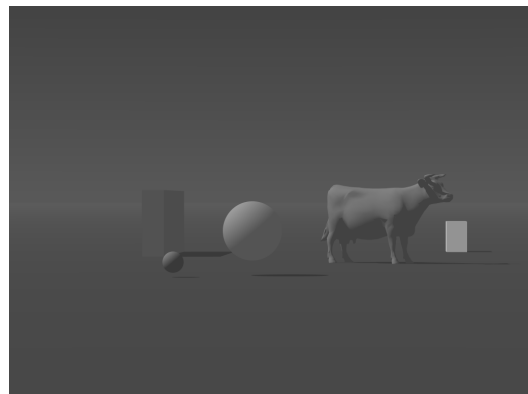
(b) Performance Test Scene 2
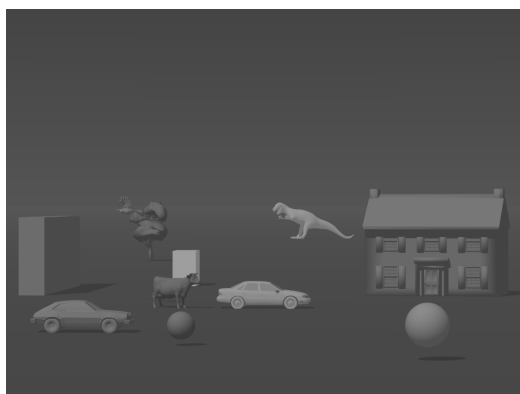
(c) Performance Test Scene 3
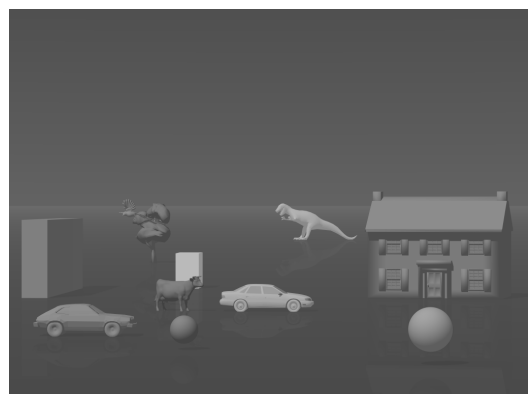
(d) Performance Test Scene 4

Figure 5.2: Performance test scenes

Performance Test Scene 1 in Figure 5.2(a) comprises of two cubes and two spheres with a terrain plane and clear sky background. All surfaces have diffuse materials. Therefore, there is no secondary reflections in this test scene. This test scene has very simple scene geometry.

Performance Test Scene 2 in Figure 5.2(b) is another scene, consists of triangle based mesh geometry model in addition to *Performance Test Scene* 1. The mesh model contains 5804 triangle faces. In the same way, all scene objects have diffuse materials.

Performance Test Scene 3 in Figure 5.2(c) has more complex scene geometry. There are nearly 30000 triangle surfaces in addition to two cubes and two spheres with a terrain plane and clear sky background in this scene.

Performance Test Scene 4 in Figure 5.2(d) contains the same geometry as in the *Performance Test Scene* 3 but this time, terrain plane has a specularly reflective material. Hence, secondary reflections are taken into account for this test scene.

In the general sense, the purposes of the test scenes are to investigate the effects of the number of the ray-surface intersections and radiometric signature calculations on ray tracing algorithm efficiency. For example, screen resolution size, complexity of the objects geometry, surfaces optical properties and signature models affect ray-surface interactions and radiance computations.

5.2 Simulation Datasets

This section describes the radiometric datasets of the signature components which are used in the developed infrared scene simulation system to calculate the total infrared signatures. Furthermore, the radiometric datasets are presented with figures for the different cases.

The main component of the thermal signature is temperature. Spectral blackbody radiance curves for the temperatures of $50\,^{\circ}C$, $75\,^{\circ}C$ and $100\,^{\circ}C$ are calculated from Planck's Law and given in Figure 5.3 and Figure 5.4 for the MWIR and LWIR spectral regions, respectively.
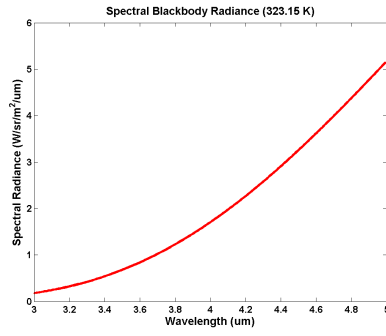
(a) 50 °C
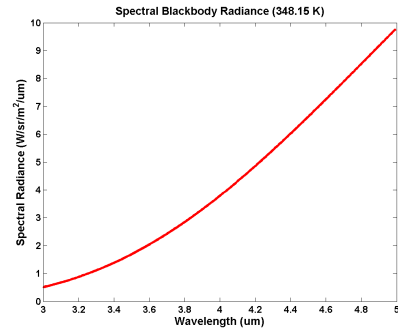
(b) 75 °C
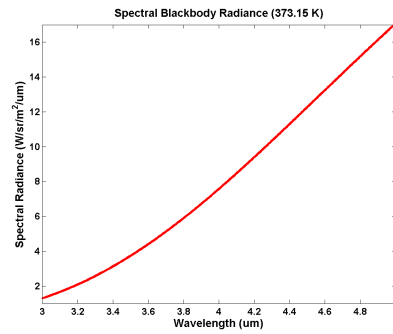
(c) 100 °C

Figure 5.3: Spectral blackbody radiances for the MWIR band
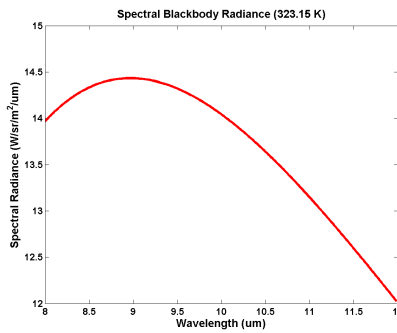
(a) 50 °C
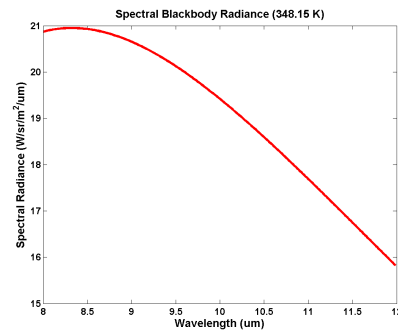
(b) 75 °C
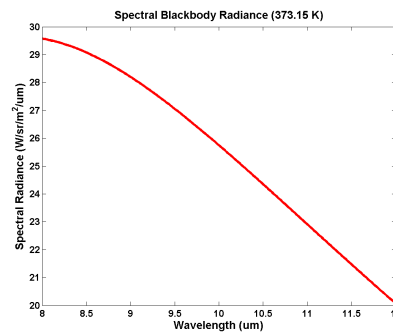
(c) 100 °C

Figure 5.4: Spectral blackbody radiances for the LWIR band

Total incident radiance captured by a sensor is affected by the spectral system response of the sensor. Spectral system response for the infrared regions of midwave and longwave are shown in Figure 5.5. These values are taken as an example and do not correspond to any specific sensor system.

(a) MWIR

(b) LWIR
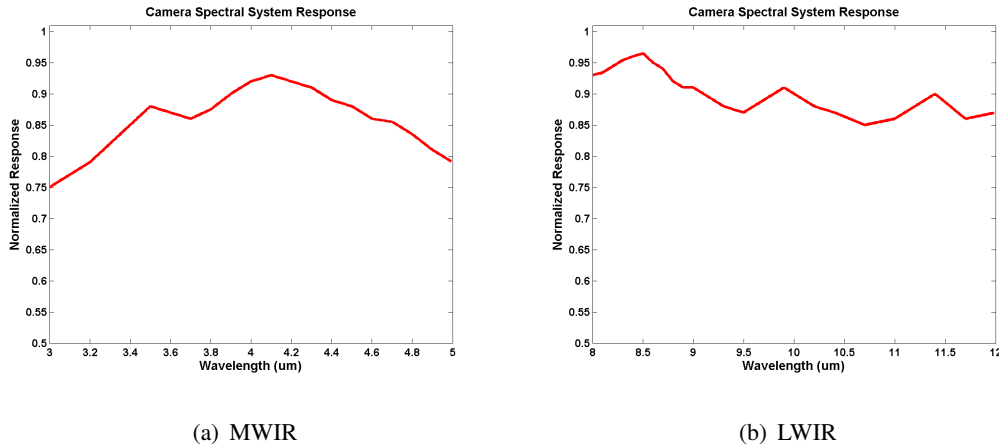
Figure 5.5: Sensor spectral system response

Material optical properties determine the reflectivity and emissivity characteristics of the surfaces. Hence, the reflected and emitted radiance are affected by material spectral properties. A variety of spectral material data is obtained from ASTER spectral library for this thesis work. Some of these materials have highly emissive nature whereas, the others have reflective optical properties. Furthermore, some materials may have different spectral characteristics over wavelengths but the others may be constant for all wavelengths. Spectral emissivity characteristics of some particular materials are presented with figures in this section. By the way, spectral reflectivity of these materials has a reverse behaviour of the spectral emissivity.

Blackbody and graybody materials are theoretical materials are generally used in simple infrared signature models to approximate surface material properties. They have constant nature for all the spectral bands. A blackbody material perfectly absorbs and emits all the radiation and do not reflects. However, graybody materials have both constant emissive and reflective components. Figure 5.6 shows blackbody spectral emissivity data for the MWIR and LWIR waveband regions.

70

(a) MWIR

(b) LWIR
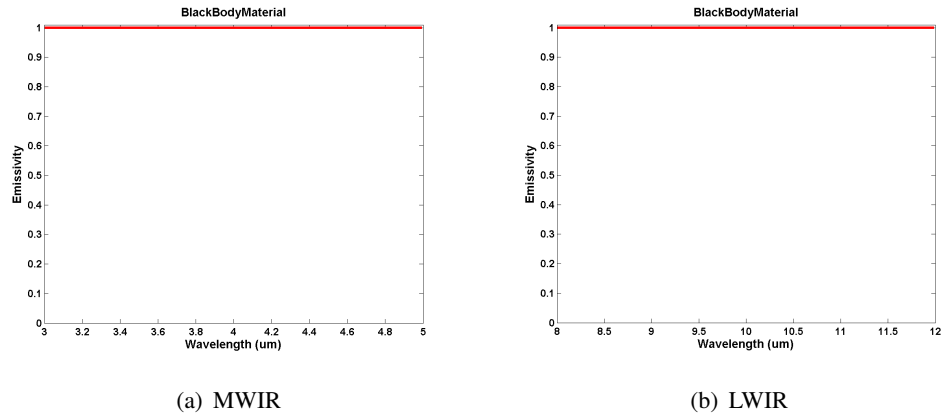
Figure 5.6: Blackbody spectral emissivity data

In addition to blackbody and graybody materials, measured optical data for a number of different materials are described. Figure 5.7 shows spectral emissivity data of the *bare red brick* material for the MWIR and LWIR spectral regions.

(a) MWIR

(b) LWIR
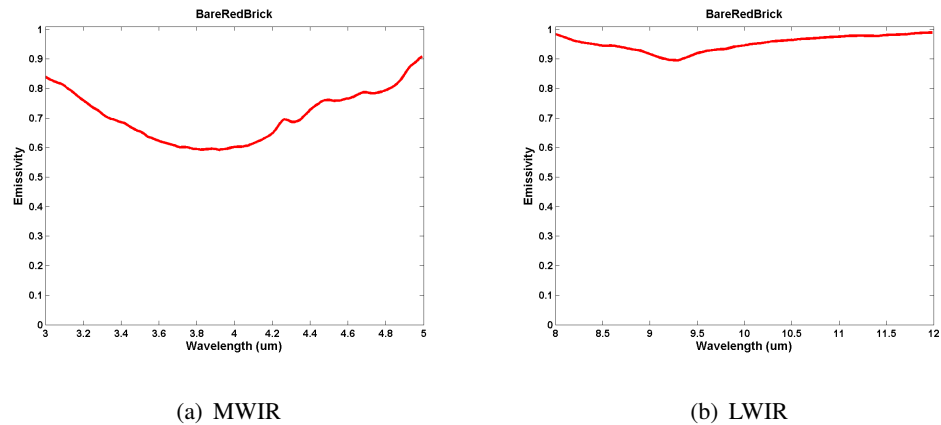
Figure 5.7: Bare red brick spectral emissivity data

In the infrared region, most of the materials generally have highly emissive nature in the LWIR sub bands. The *sandy soil* material displays a typical curve is given in Figure 5.8, showing higher values of spectral emissivity in the interval of $8 - 12\ \mu m$ than at wavelengths shorter than $5\ \mu m$.

Plate window glass however, has a different characteristics. It is more reflective in the LWIR region than MWIR region exceptionally. Spectral emissivity of this material is shown in Figure 5.9.
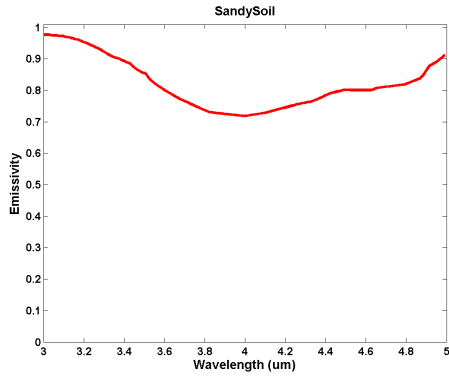
(a) MWIR
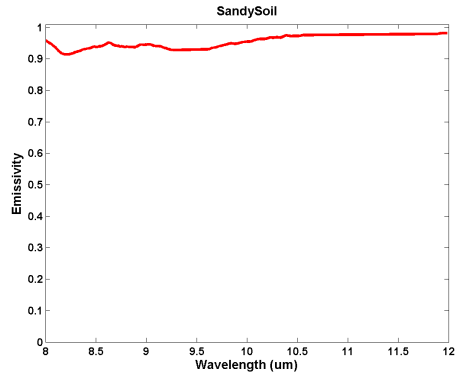
(b) LWIR

Figure 5.8: Sandy soil spectral emissivity data
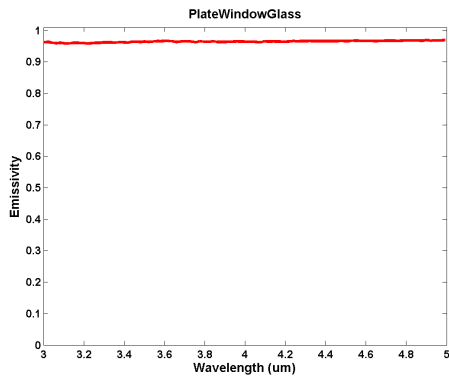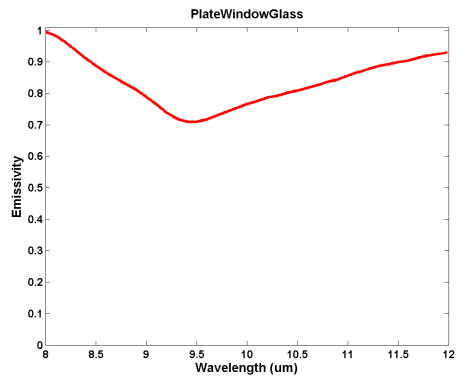
(a) MWIR

(b) LWIR

Figure 5.9: Plate window glass spectral emissivity data
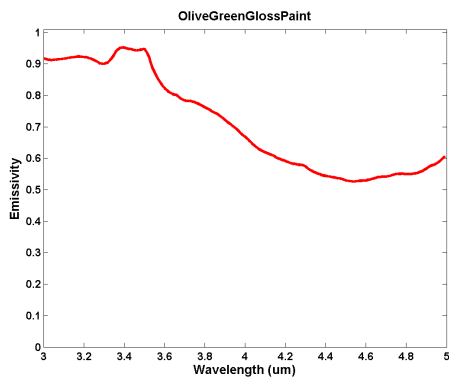
(a) MWIR
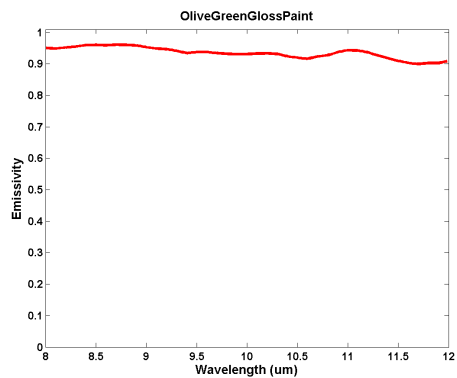
(b) LWIR

Figure 5.10: Green gloss paint spectral emissivty data

In the infrared imaging applications, painted materials are commonly used to determine surface optical properties. An object with highly emissive surface radiates more energy as compared to highly reflective surfaces in thermal bands. For example, infrared imaging target detection system of a missile seeker can detect highly emissive objects easily. By covering the objects with reflective painted materials may decrease the radiated signature of the targets. Figure 5.10 shows spectral emissivity of the *green gloss paint*. As can be seen, it has a low emissive characteristics in the MWIR region.

Atmospheric effects have a significant effect on the total signature captured by the infrared sensor. In order to model the atmospheric effects accurately, MODTRAN radiative transfer model is used. Spectral atmospheric transmittance, path radiance, solar irradiance and sky radiance data are obtained from MODTRAN for the specified line of sight path geometries and atmospheric conditions.

In order to analyze the atmospheric effects in different conditions, two types of scenarios are defined. These are labelled as *Type1* and *Type2*. In these scenarios, clear sky background with *Rural* aerosol model at meteorological range of $23km$ is considered. The spectral wavebands are selected as $3 - 5 \ \mu m$ (MWIR) and $8 - 12 \ \mu m$ (LWIR) with a $1 \ cm^{-1}$ spectral resolution. *MidLatitude Summer* and *MidLatitude Winter* standart atmosphere models are used to represent average seasonal and latitude variations in atmospheric properties such as air temperature, pressure, relative humidity and concentrations of molecules. It is assumed that all of the infrared scene simulations are performed on geographic location at $35°$ latitude and $30°$ longitude.

Type 1 atmosphere data are obtained for the universal time 13:00pm and the date 15, July. MidLatitude Summer atmosphere model is selected in this scenario. Spectral atmospheric transmittance and path radiance data for three different range values are given in Figure 5.11 and Figure 5.12, respectively to represent the Type 1 scenario in both MWIR and LWIR regions. Then, spectral sky radiance data for three different zenith angles and spectral solar irradiance data are shown in Figure 5.13 and Figure 5.14, respectively for the MWIR and LWIR regions.
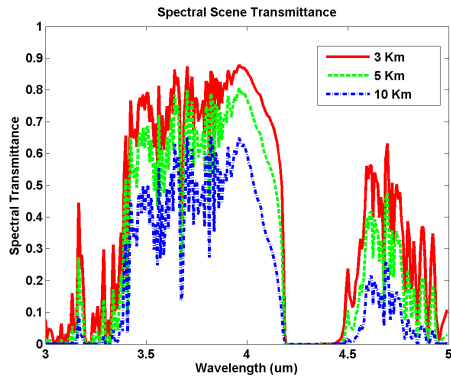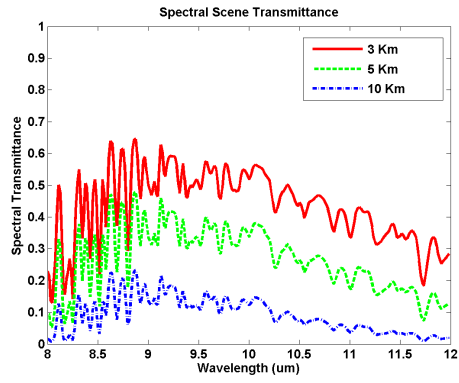
(a) MWIR

(b) LWIR

Figure 5.11: Spectral transmittance for $3, 5$ and $10km$ ranges for the Type 1.
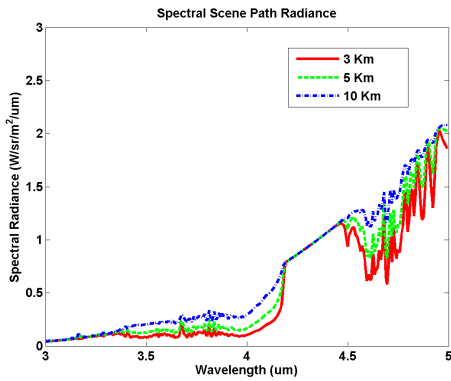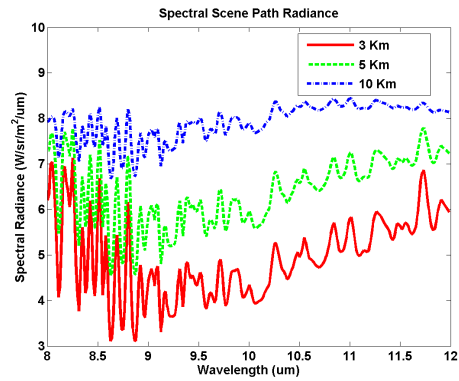
(a) MWIR

(b) LWIR

Figure 5.12: Spectral path radiance for $3, 5$ and $10km$ ranges for the Type 1.
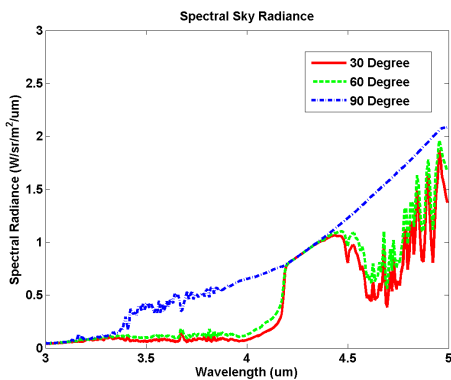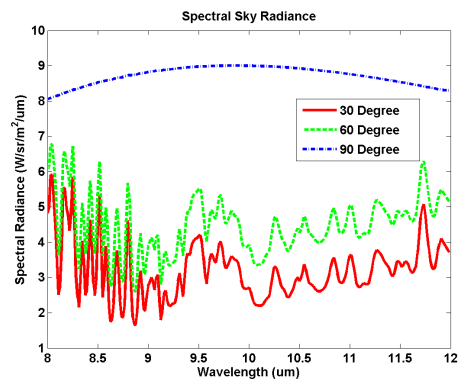
(a) MWIR

(b) LWIR

Figure 5.13: Spectral sky radiance for $30, 60$ and $90°$ zenith angles for the Type 1.
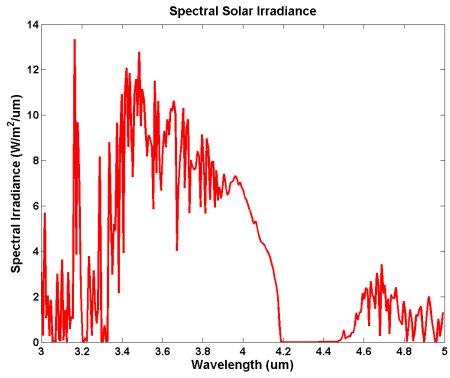
(a) MWIR
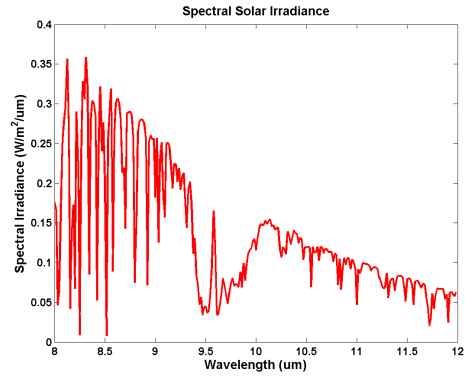
(b) LWIR

Figure 5.14: Spectral solar irradiance for the Type 1

Band-averaged atmospheric transmittance data with in-band atmospheric path radiance and sky radiance data are calculated from spectral atmospheric radiation data which are given previously are integrated across sensor spectral band of the interest. Band-averaged atmospheric transmittance and in-band path radiance data are shown as a function of distance in Figure 5.15 and Figure 5.16, respectively to represent the Type 1 scenario in both MWIR and LWIR regions. Then, in-band sky radiance data are presented as a function of zenith angle in Figure 5.17 for the MWIR and LWIR regions.
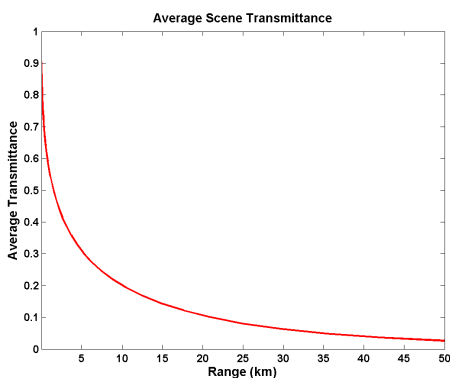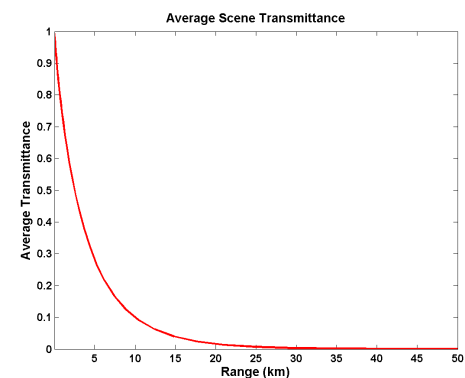
(a) MWIR

(b) LWIR

Figure 5.15: Band-averaged transmittance as a function of distance for the Type 1.
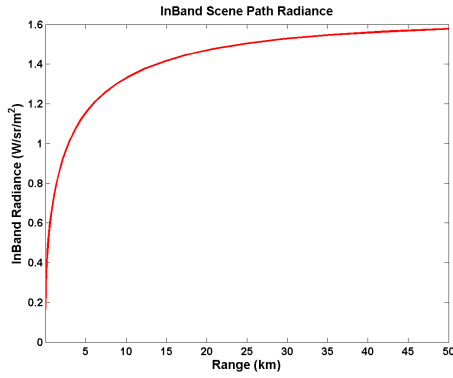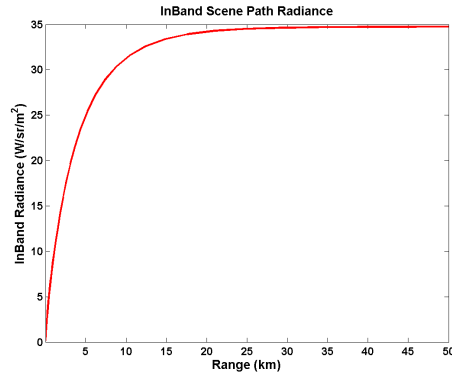
(a) MWIR

(b) LWIR

Figure 5.16: In-band path radiance as a function of distance for the Type 1.
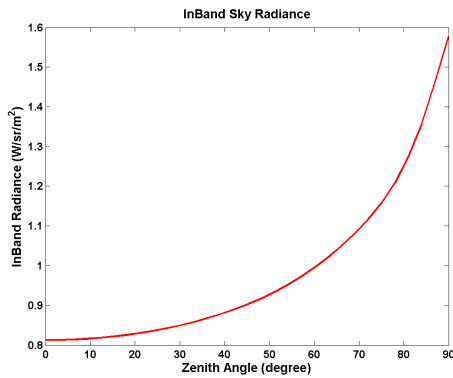
(a) MWIR
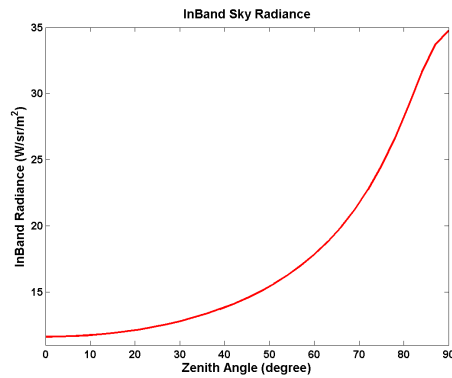
(b) LWIR

Figure 5.17: In-band sky radiance as a function of zenith angle for the Type 1.

Type 2 atmosphere data are obtained for the universal time 13:00pm and the date 15,January. MidLatitude Winter atmosphere model is selected in this scenario. Spectral atmospheric transmittance and path radiance data for three different range values are given in Figure 5.18 and Figure 5.19, respectively to represent the Type 2 scenario in both MWIR and LWIR regions. Then, spectral sky radiance data for three different zenith angles and spectral solar irradiance data are shown in Figure 5.20 and Figure 5.21, respectively for the MWIR and LWIR regions.

76
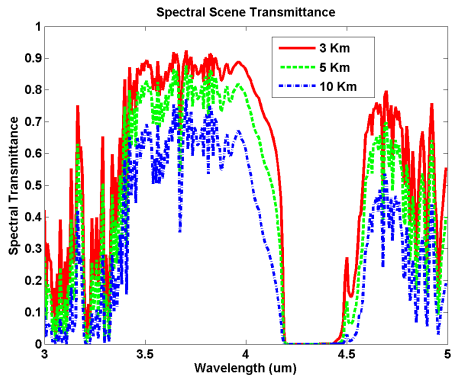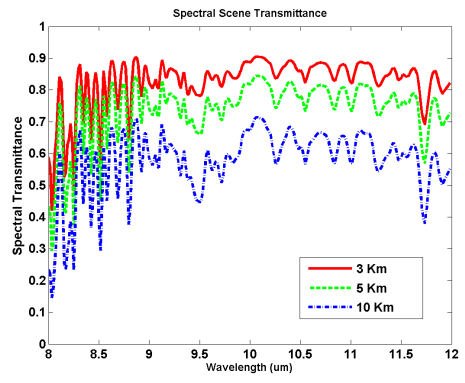
(a) MWIR   (b) LWIR

Figure 5.18: Spectral transmittance for 3, 5 and $10km$ ranges for the Type 2.
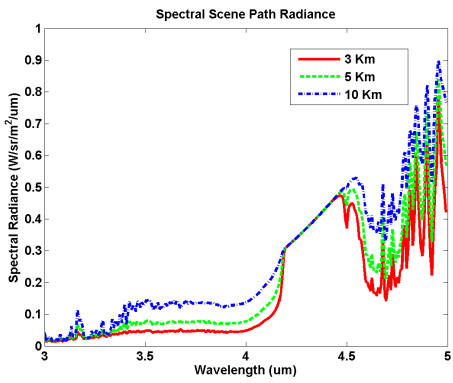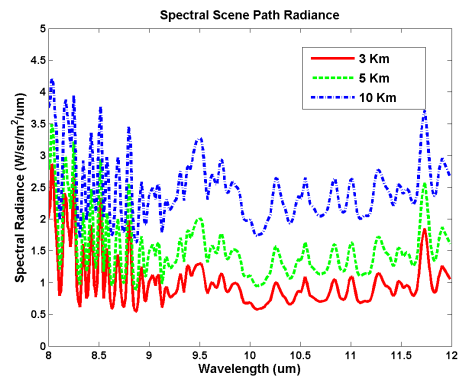
(a) MWIR   (b) LWIR

Figure 5.19: Spectral path radiance for 3, 5 and $10km$ ranges for the Type 2.
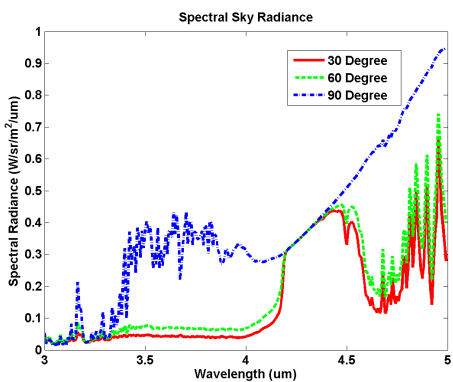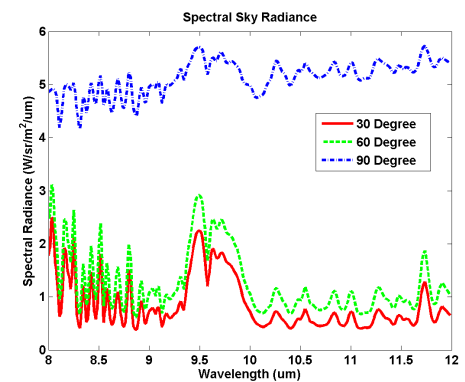
(a) MWIR   (b) LWIR

Figure 5.20: Spectral sky radiance for 30, 60 and $90°$ zenith angles for the Type 2.
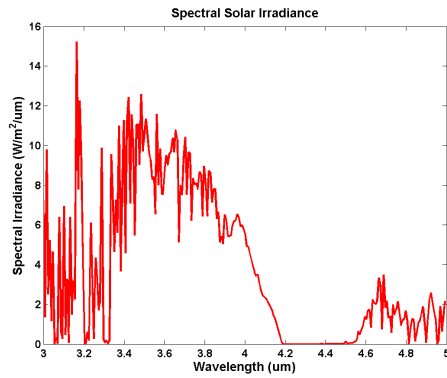
(a) MWIR
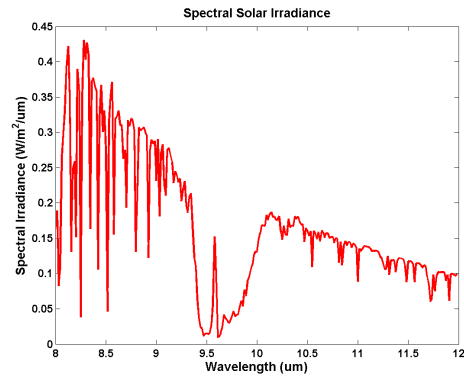
(b) LWIR

Figure 5.21: Spectral solar irradiance for the Type 2.

Band-averaged atmospheric transmittance and in-band path radiance data are shown as a function of distance in Figure 5.22 and Figure 5.23, respectively to represent the Type 2 scenario in both MWIR and LWIR regions. Then, in-band sky radiance data are presented as a function of zenith angle in Figure 5.24 for the MWIR and LWIR regions.

Some important points are needed to be emphasized before passing to the analysis results section. As can be seen from the figures that all of the radiometric data are highly dependent on spectral wavelengths. They have also a different characteristics in the MWIR and LWIR wavebands.
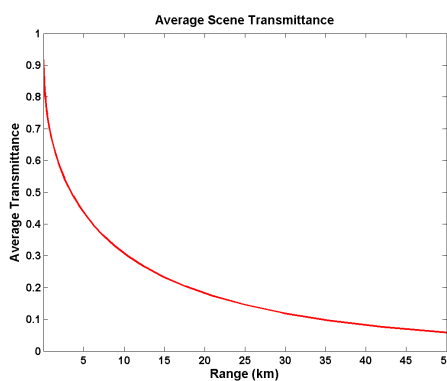
(a) MWIR
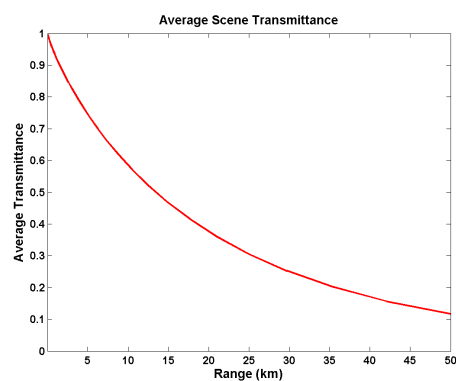
(b) LWIR

Figure 5.22: Band-averaged transmittance as a function of distance for the Type 2.
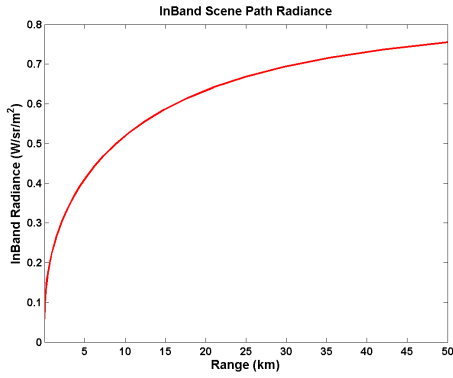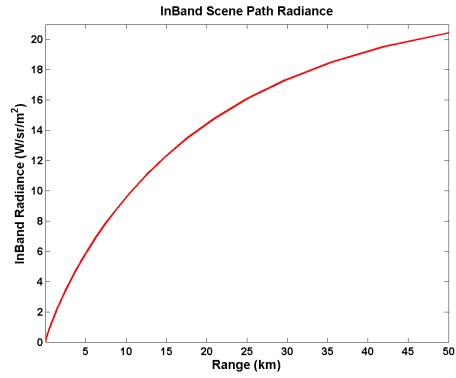
(a) MWIR   (b) LWIR

Figure 5.23: In-band path radiance as a function of distance for the Type 2.
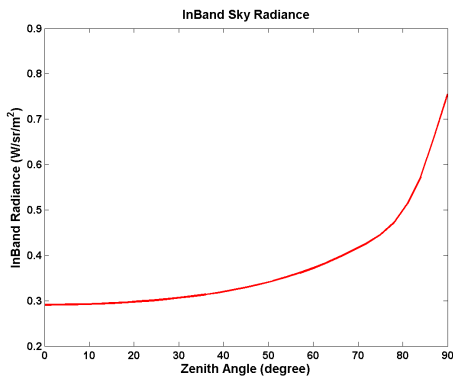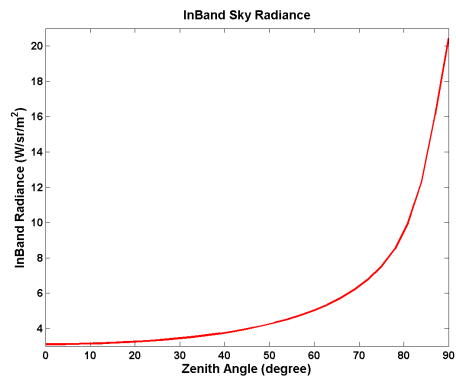
(a) MWIR   (b) LWIR

Figure 5.24: In-band sky radiance as a function of zenith angle for the Type 2.

Blackbody radiance curves for different temperatures have an interesting distribution over the spectral wavelengths. As the temperature increases, peak value of spectral blackbody radiance data shifts to shorter wavelengths. Moreover, atmospheric transmittance has a significant variance over the wavelengths, especially in MWIR spectral bands. Due to CO_2 emissions in the wavebands of $4.2 - 4.4\ \mu m$, atmospheric transmittance is almost zero in this region. Furthermore, seasonal variations have a reasonable effect on the atmospheric data. MidLatitude Summer and MidLatitude Winter standart atmosphere models are considered to represent seasonal differences with Type 1 and Type 2 scenarios. For the Type 1 conditions, which is MidLatitude Summer atmosphere model, atmospheric transmittance decreases rapidly as a function of distance, especially in the LWIR region. Whereas, for the Type 2 atmosphere, which

79

is MidLatitude Winter model, atmospheric attenuation decreases slowly as compared to Type 1. Conversely, path radiance has higher values for the Type 1.

In addition, spectral transmittance displays little variation in the LWIR band as compared with the MWIR region. Also, spectral solar radiation shows a significant different characteristics. In the MWIR band, solar irradiance data have considerably high values compared to LWIR region. Hence, solar reflected radiations become more significant in the MWIR band. Moreover, atmospheric transmittance, path radiance and sky radiance values vary with line of sight geometry. For example, as the distance between the sensor and region of interest increases, atmospheric transmittance decreases and becomes significant attenuator wheras path radiance increases as a function of distance.

One infrared scene feature of interest as can be seen in Figure 5.25 is the infrared horizon. Nearer to the horizon the path radiance component becomes significant as the atmospheric transmission is reduced. Above the horizon the sky radiance falls as the zenith angle is decreased, consistent with the reduction in the path radiance component. This is because the path becomes more optically dense as more atmosphere at low altitudes is included in the simulation. The sky radiance is also dependent on the spectral band. For the MWIR waveband, the sky radiance is less as compared to the LWIR as shown in figures. Since the temperature interval of the sky is relatively low, for example $0 - 25°C$, its radiance is more for the longer wavebands as a result of the Planck curve.
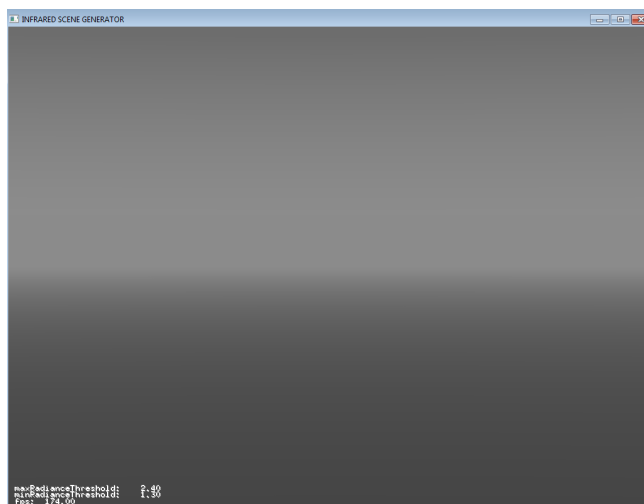
Figure 5.25: Infrared horizon

5.3 Analysis Results

In this section the analysis results of the simulated infrared test scenes are presented to investigate the effects of the radiometric signature components and performance parameters. Simulation results of the infrared test scenes are produced in numerical data form and analyzed with graphical and tabular representations.

5.3.1 Signature Analysis

This section presents detailed analysis of the infrared signature components to investigate the effects of the signature models on the infrared radiation captured by the sensor. In order to analyze the results, predefined signature test scenes are simulated for MWIR and LWIR spectral wavebands, Type 1 and Type 2 atmosphere conditions, different temperatures, material characteristics and object geometries.

In some cases, signature analysis is intended to eliminate reflected radiations. As described in the previous section, object surfaces in the specific signature test scenes are assigned as blackbody material in order to preclude the possible reflected radiations from these objects due to other sources. In order to understand the impact of the line of sight geometry of the atmosphere on total signature, signature test simulations are repeated for different range values.

As an analysis criterion, an error metric ξ, which shows the error percentage, is defined for the analyses with the following equation.

$$\xi = \frac{\left| L_{total} - \hat{L}_{total} \right|}{L_{total}} \times 100 \tag{5.1}$$

where L_{total} represents the total incident radiance result into the sensor computed with spectral signature model and $\hat{L}_{total}$ indicates the total incident radiance with band-averaged signature model. This metric actually indicates the differences of the total signature values with respect to band-averaged signature modeling and spectral based signature modeling approaches. Since the infrared signature components have wavelength dependent parameters spectral signature calculation approach is radiometrically more accurate model compared to band-averaged calculation approach as

81

explained previously. Hence, spectral signature equation proposed in section 3.3.1 is assumed as reference model and actual radiance values are calculated using this approach.

As a result of these simulations, total radiances at sensor are obtained from band-averaged signature model and spectral signature model calculations and the error percentages of the signature models are represented with graphs. At the end of this section, signature analysis results are discussed.

5.3.1.1   Atmosphere Analysis

For the first analysis, the effects of the atmospheric components on infrared signature are analyzed by simulating Signature Test Scene 1. In this analysis, Type1 and Type2 atmosphere conditions are simulated for signature models in both MWIR and LWIR bands. In each simulation, a set of results are obtained for the temperatures of $50°C$, $75°C$ and $100°C$, and range values in the interval of $0 - 50\ km$.

Total radiance results calculated from spectral signature model as a function of range are given in Figure 5.26 for the Type 1 in both MWIR and LWIR bands.
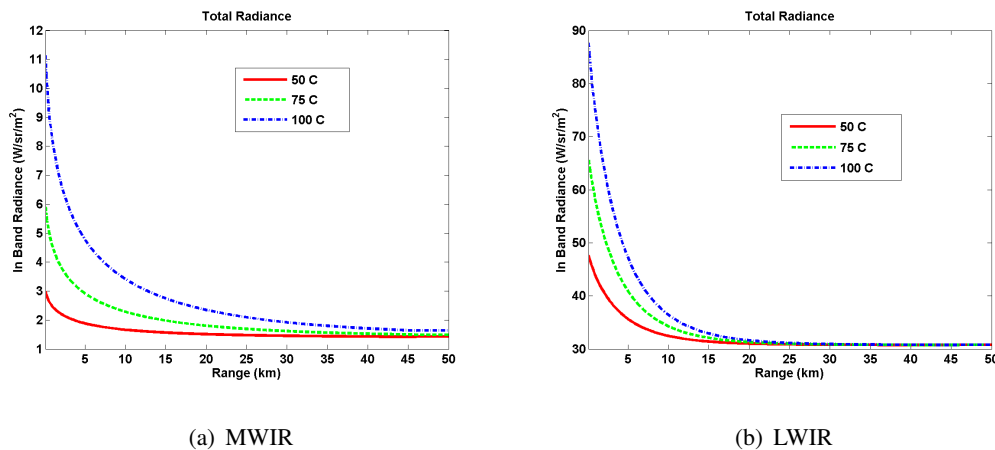
(a) MWIR   (b) LWIR

Figure 5.26: Type 1 atmosphere analysis, total radiance for the spectral signature model.

Similarly, Figure 5.27 shows the total radiance results of the band-averaged signature model for the Type 1.
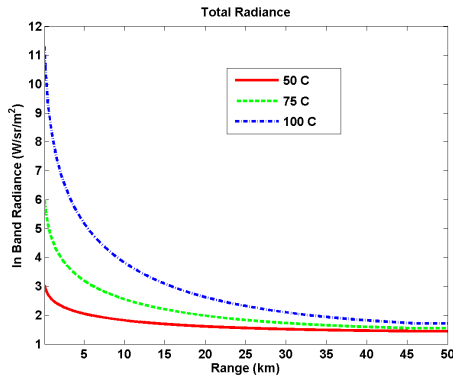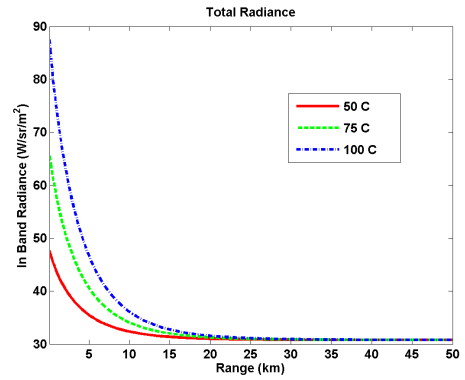
(a) MWIR   (b) LWIR

Figure 5.27: Type 1 atmosphere analysis, total radiance for the band-averaged signature model.

In order to analyze the effects of the atmosphere on signature model in MWIR and LWIR bands, the total radiance results obtained from the spectral and band-averaged signature models are compared by computing the error percentages. Figure 5.28 shows the error results for the Type 1 atmosphere analysis in MWIR and LWIR bands.
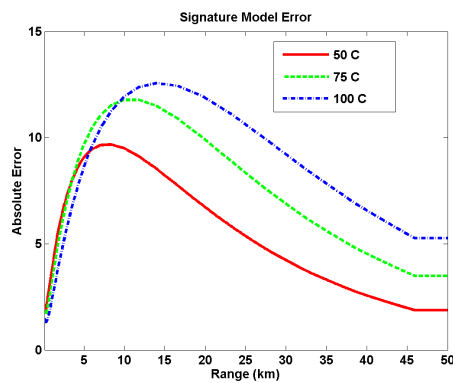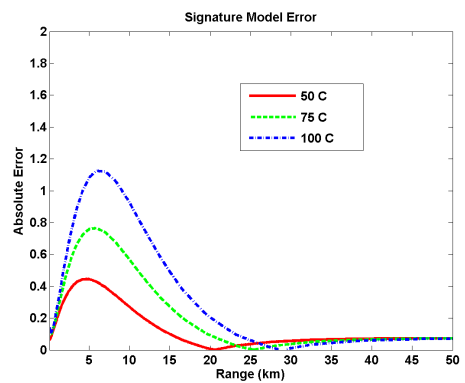
(a) MWIR   (b) LWIR

Figure 5.28: Type 1 atmosphere analysis, signature model error.

The same analyses are performed again for the Type 2 atmosphere conditions. Total radiance results and signature model error percentages are obtained from simulations and given with figures. Spectral signature model total radiance results for the Type 2 in both MWIR and LWIR bands are shown as Figure 5.29.
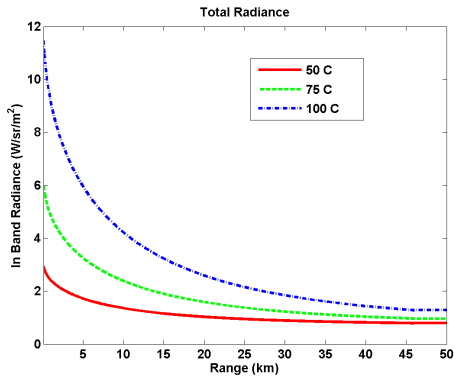
(a) MWIR
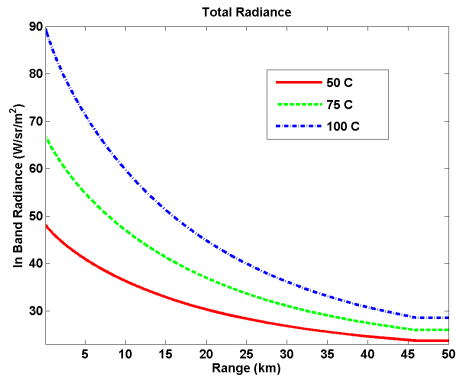
(b) LWIR

Figure 5.29: Type 2 atmosphere analysis, total radiances for the spectral signature model.
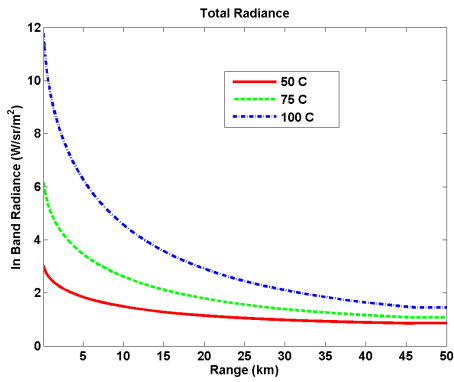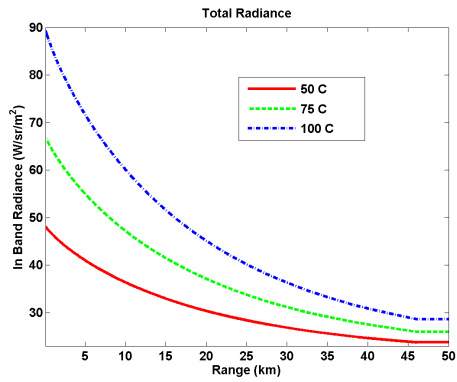
(a) MWIR

(b) LWIR

Figure 5.30: Type 2 atmosphere analysis, total radiances for the band-averaged signature model.
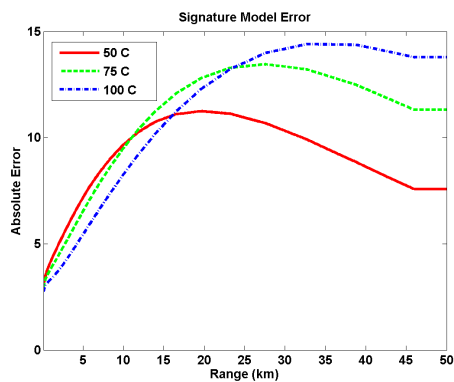
(a) MWIR
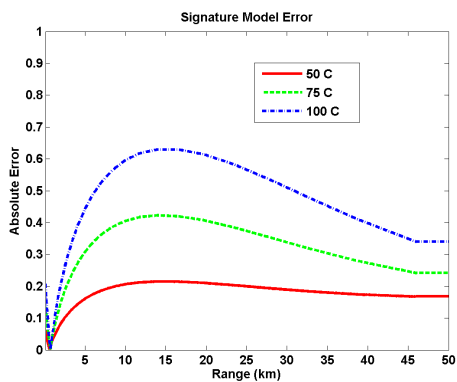
(b) LWIR

Figure 5.31: Type 2 atmosphere analysis, signature model error.

Similarly, Figure 5.30 shows the total radiance results of the band-averaged signature model for the Type 2. Lastly, Figure 5.31 gives the signature model error results for the Type 2 atmosphere analysis.

5.3.1.2 Temperature Analysis

In order to analyze the impact of the temperature on infrared signature, Signature Test Scene 2 is simulated in both MWIR and LWIR bands for a varying number of temperature values in the interval of $0 - 25°C$. In this analysis, Type 1 atmosphere is used and a set of results are obtained for the distances of $1\ km$, $5\ km$ and $10\ km$.

Total radiance results calculated from spectral signature model are shown as Figure 5.32 for the Type 1 in both MWIR and LWIR bands.

(a) MWIR   (b) LWIR
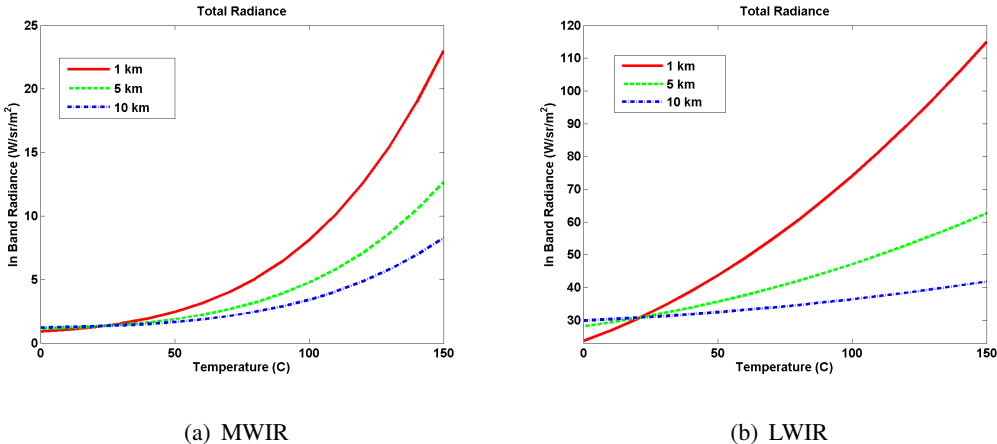
Figure 5.32: Temperature analysis, total radiances for the spectral signature model.

For this time, the same analyses are performed again for the band-averaged signature model. Total radiance results for the Type 1 in both MWIR and LWIR bands are shown as Figure 5.33.

From the total radiance results obtained by simulating Signature Test Scene 2, signature model error percentages are calculated for the different temperature values. Figure 5.34 gives the error results for the temperature analysis in MWIR and LWIR bands.
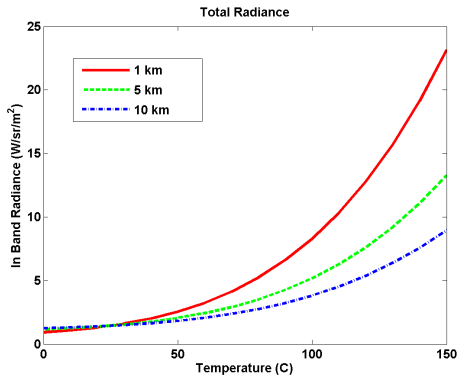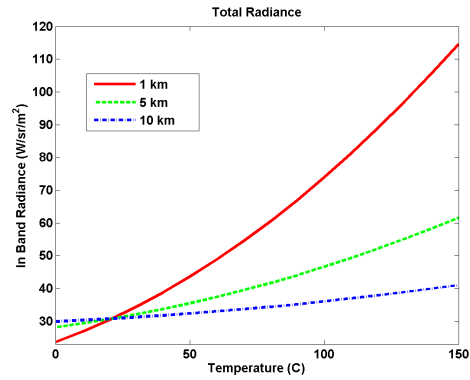
(a) MWIR   (b) LWIR

Figure 5.33: Temperature analysis, total radiances for the band-averaged signature model.
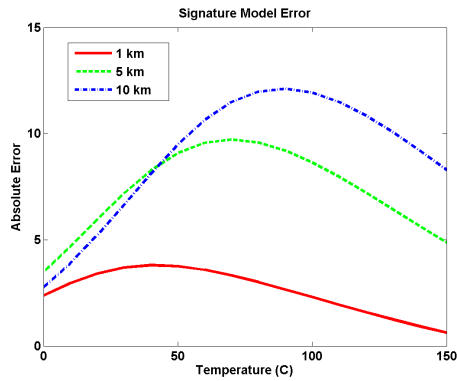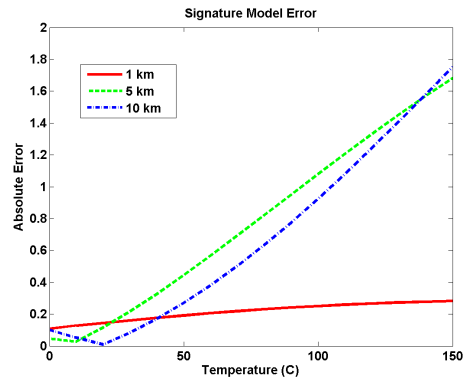
(a) MWIR   (b) LWIR

Figure 5.34: Temperature analysis, signature model error.

5.3.1.3 Reflection Analysis

In this analysis, the effects of the surface material reflection properties on infrared signature are analyzed. Green gloss paint material is used in the Signature Test Scene 3 for the Type 2 atmosphere conditions in both MWIR and LWIR bands. In each simulation, a set of results are obtained for the temperatures of $50°C$, $75°C$ and $100°C$, and range values in the interval of $0 - 50\ km$.

Total radiance results calculated from spectral signature model as a function of distance are given in Figure 5.35 for the Type 2 in both MWIR and LWIR bands.
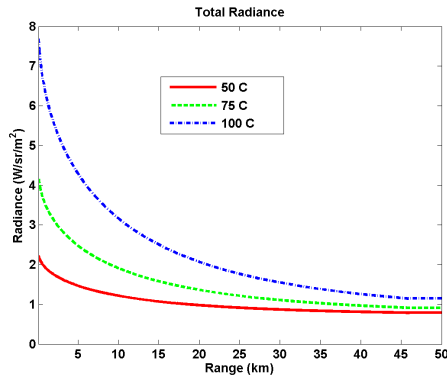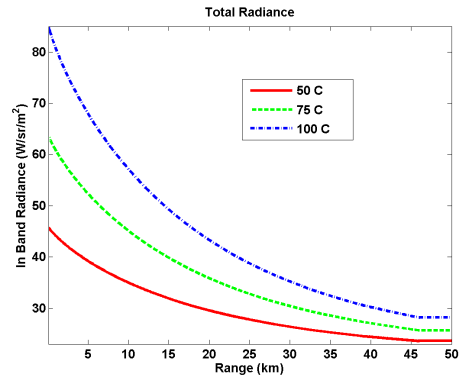
(a) MWIR

(b) LWIR

Figure 5.35: Reflection analysis, total radiances for the spectral signature model.
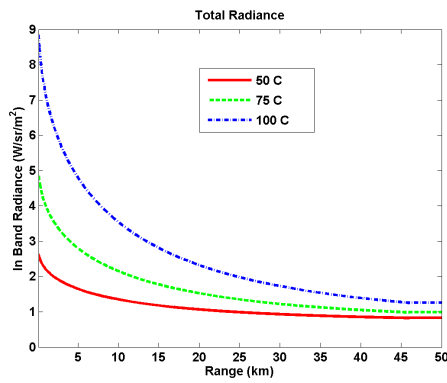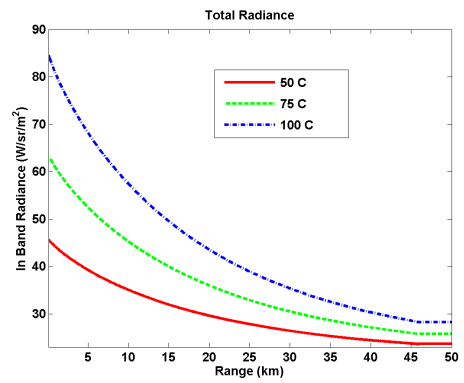
(a) MWIR

(b) LWIR

Figure 5.36: Reflection analysis, total radiances for the band-averaged signature model.
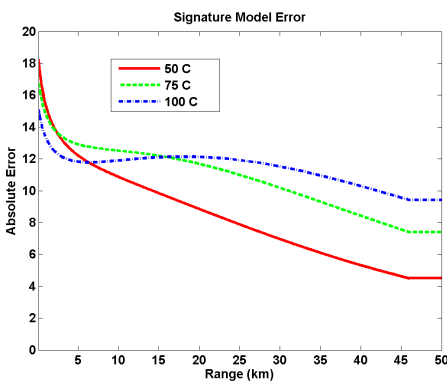
(a) MWIR
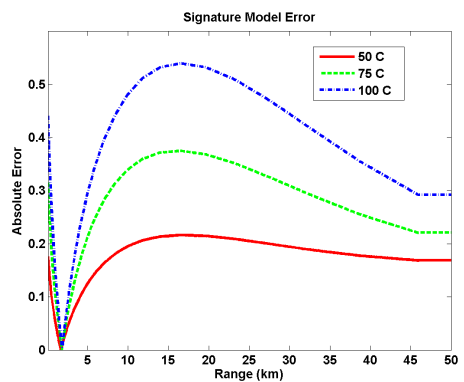
(b) LWIR

Figure 5.37: Reflection analysis, signature model error.

87

Similarly, Figure 5.36 shows the total radiance results of the band-averaged signature model. The signature model error results are obtained for the reflection analysis are given in Figure 5.37 for both MWIR and LWIR bands.

5.3.1.4   Discussions on Signature Analysis

In this section, results of the signature analysis of the test scenes are discussed in general. It can be observed from the results that the infrared radiation is directly affected by the atmospheric effects, temperature, material characteristics and spectral wavebands. Also, the spectral sensor response directly affects the total radiance incident on the sensor. Hence, the band-averaged signature model can not accurately characterise the sensor response.

As can be seen from the total radiance analysis results, the radiance decreases as a function of the distance due to atmospheric transmittance effect. The total radiance becomes equal to the atmospheric path radiance component for the very distant objects, where the atmosphere attenuates all the incident radiation from the scene objects, eventually. For example, in Figure 5.26, the total radiance results of the blue curve, which represents an object of $100°C$, vary with distance. The total radiance at a distance of $5\ km$ is reduced more as compared to the radiance at $10\ km$ as a result of the atmospheric attenuation. Hence, the total radiance decreases with increase in distance for the given temperatures.

Furthermore, total radiance increases as a function of the temperature as can be seen from the temperature analysis results. For example, in Figure 5.32, the red curve, labelled as $1\ km$, represents the radiance results at a distance of $1\ km$. The total radiance results of an object with $100°C$ are larger than the radiance with $50°C$ as a result of the Planck Law. Moreover, similiar results of the atmosphere analysis can be seen from the temperature analysis. In the same figure, the total radiance reduces as a function of distance. For example, the red curve represents the distance of $1\ km$ has the maximum radiance values as compared to the distances of $5\ km$ and $10\ km$, the green and blue curves, respectively. Hence, the radiance values of the curves decrase as a function of range. However, there is an important point that should be noted. In Figure 5.32, the three radiance curves for the temperature values

smaller than nearly $20°C$ have a different characteristics with respect to range values. Since the atmospheric path radiance component dominates the total radiance for the relatively low temperatures, especially in the LWIR band, the total radiances of these temperatures are maximum for the further objects.

Another result of the atmosphere analysis is that seasonal variations significantly affect the total radiances. Type 1 and Type 2 scenarios are used to analyze the total radiance results. For the Type 1 conditions, atmospheric transmittance decreases more rapidly as a function of distance as compared to Type 2 scenario. In contrast to transmittance, the path radiance has higher values for the Type 1. In a similar fashion, comparing the total radiance for the Type 1 and Type 2 conditions, the total radiance is decreasing more rapidly in Type 1 as the atmospheric transmittance is getting more. Therefore, the effect of the weather and the distance on the infrared radiations is adverse.

In reflection analysis, it can be seen that material optical characteristics have an important impact on the total radiance. For the temperature and atmosphere analysis, blackbody material is used. However, in order to analyze the reflected signature radiation, a material has both emissive and reflective nature is used. Therefore, the total radiance from the object is the sum of the the reflected and emitted radiances. The emissivity values of this material are smaller than the blackbody object. Therefore, total emitted radiance is reduced. However, solar reflected and sky reflected radiances contribute to the total radiance at this time. Solar radiation component is dominant in shorter wavelengths as it is explained from the previous section. In thermal infrared, solar reflected radiances have a small contributions to total radiances, especially in the LWIR band.

The green gloss paint material which is used in Signature Test Scene 3 has a considerable reflection characteristics as can be seen from the figures. Hence, the total radiance of this material is less than the total radiance of the blackbody material at the same temperature. It can be seen by comparing the total radiance analysis results of the blackbody material and reflective material at the same conditions. In Figure 5.29, the total radiance of the blackbody material with $100°C$ at a distance of $10\ km$ for the Type 2 atmosphere scenario is nearly $4\ W.sr^{-1}.m^2$ in the MWIR band and

$65\ W.sr^{-1}.m^2$ in the LWIR band. However, in Figure 5.35, the total radiance of the reflective material with $100°C$ at a distance of $10\ km$ for the Type 2 atmosphere is nearly $3\ W.sr^{-1}.m^2$ in the MWIR band and $60\ W.sr^{-1}.m^2$ in the LWIR band. It can be concluded that the total radiance of an object is the maximum as its emissivity is more. Also, solar reflected signatures are not significantly affect the total radiance of an object with high temperature, especially in the LWIR regions.

Signature model error analyses for the proposed signature models made for both in the MWIR and LWIR spectral regions. The error results show that spectral dependency of the radiometric data significantly affects the total incident radiances for the MWIR band when compared to the ones in the LWIR. This is mainly because in the MWIR region the spectral variation of the atmospheric transmittance has a significant effect on signature calculation.

In some cases, the maximum absolute error may rise (up) to 20% for the MWIR region. Since the atmospheric transmittance data have a significant spectral variation in the MWIR region, blackbody and graybody material assumption may not give the accurate results for the band-averaged signature calculation model. On the other hand, the maximum error remains below 2% for the LWIR band. This means that the lack of exact spectral radiance calculation may not be critical for signature modeling in the LWIR region. Also, it can be good approximation to use band-averaged values for camera response, atmospheric transmittance and material optical properties in LWIR waveband where radiometric data display little spectral variation across the band of interest.

Atmospheric transmittance curves have a considerable spectral variation in the MWIR band, especially for the $4.2 - 4.4\ \mu m$ sub bands due to molecular absorptions in the atmosphere. For this reason, band-averaged atmospheric transmittance can not represent the actual spectral behavior and leads to errors when it is used in the proposed band-averaged signature model. As can be seen from the signature model error results for the atmosphere analysis in the MWIR band, the error percentages changes as a function of distance. Since the spectral variation of the atmospheric transmittance is not handled in band-averaged signature model, the atmospheric attenuation is the main reason of the error. The signature model error increases as a function of dis-

tance, where transmittance values are dominant in calculation of the total radiance. For example, in Figure 5.28, signature model error has the maximum values in the interval of $10 - 20 \, km$ in the MWIR case. In this example, atmospheric transmittance becomes an important atteunator and significantly affects the total radiance. However for the small distances transmittance percentage has maximum values and can not considerably change the total radiance. Similarly, signature model error decreases for the very distant objects, where the atmosphere attenuates all the radiation and spectral dependency becomes insignificant.

In order to understand the effects of the atmosphere conditions on signature model error, Type 1 and Type 2 signature results for the atmosphere analysis are compared. In addition to distance, spectral characteristics of the transmittance curves can be an important point for the error analysis. For example, for the Type 2 atmosphere, transmittance curve has more spectral variation compared to the Type 1 as can be seen from the figures given in the previous section. Therefore, total absolute error in Type 2 is larger than the Type 1 atmosphere conditions as can be seen by comparing Figure 5.28 and Figure 5.31 for the MWIR cases. Another reason is that the atmospheric transmittance for the Type 1 decreases more rapidly as a function of distance as compared to Type 2 scenario. Since the atmospheric transmittance decreases to almost zero at smaller distances compared to Type 2 and the path radiance component becomes dominant in radiance calculations, the spectral variations of the transmittance becomes insignificant for the signature model. Conversely, atmospheric transmittance curves display less spectral variation in LWIR band as compared with MWIR region. Therefore, using the band-averaged transmittance values in the signature computation model gives more accurate results in contrast to MWIR region, where atmospheric transmittance has a significant spectral variation.

Furthermore, signature model error changes with temperature especially in the MWIR band as can be seen from the temperature analysis results. Temperature of an object determines the emission spectrum of its blackbody radiation. Note that the integrated blackbody radiance is proportional to the area under the Planck curve in the band of interest. The radiance rapidly increases with the temperature. Also, the wavelength corresponding to the maximum radiation shifts towards shorter wavelengths as the temperature increases. Moreover, the spectral variation of the transmittance curve

has the most significant effect in the $4.2 - 4.4 \; \mu m$ bands. Hence, the total signature model error increases as a function of temperature if the band of interest contains strong spectral variations due to transmittance. This is especially significant if the total integrated radiance of the band of interest is close to the integrated radiance of the sub-band with large spectral variations. Figure 5.34 illustrates the effect of the temperatures on signature model error in the MWIR and LWIR bands. For the MWIR band in the figure, the green curve represents the distance of $5 \; km$ has the maximum error values in the interval of $0 - 25°C$ temperatures and the signature model error always decreases for the out of this temperature interval as a result of the behavior of the Planck radiation distributions. Hence, the total signature model error increases as a function of temperature as the significant portions of the integrated radiance originates from the critical sub-band region for the given $50 - 100°C$ temperature interval.

When material optical properties such as emissivity and reflectivity have also spectral variation, graybody material assumption increases the error percentages of the band-averaged signature model. By using the spectrally variant surface material instead of the blackbody material in reflection analysis, the total signature model error increases in the MWIR band as can be seen from Figure 5.37. Also, the error percentages have the maximum values at smaller distances in the MWIR region. This is simply because the spectral material characteristics are dominant on the reflected total radiance for the initial distances. Also, temperature effects and spectral variation of the atmosphere contributes the error. However, as the the total radiance is attenuated with increase in distance, atmospheric transmittance becomes more significant on the total radiance as compared to material data. Thus, error percentages decrease as a function of distance. Moreover, signature model error is minimal for the LWIR region as can be seen from the given figure. This is due to the fact that solar radiation component does not sigificantly affect the total signature as compared to the MWIR region.

It is concluded that the total radiance incident on the sensor depends on the atmospheric effects, surface geometry and material characteristics, temperature, line of sight geometry and spectral waveband region of interest. Signature components have spectrally variant radiometric data especially in the MWIR band. Hence, infrared signature model equation should take into account the spectral characteristics.

5.3.2 Performance Analysis

In this section, performance of the developed infrared scene simulation system is tested and analyzed under different performance parameters such as screen resolution, scene geometry complexity, surface material characteristics and signature modeling approach by simulating the proposed performance test scenes. Also, rendering performance is benchmarked on different hardware environments. At the end of this section, performance analysis results are discussed.

5.3.2.1 Benchmark Setup

All the hardware performance test setups use OptiX version 3.0.1 and CUDA 5.0.35 for running all simulations on Windows 7 64 bit operating system with high end CPU, Intel Core I7 3770 @3.4GHz. The test scenes are benchmarked on three different NVIDIA GeForce graphics cards: GTX 560, GTX 660 and GTX 680. Specifications for these cards are listed in Table 5.1 [48]

Table 5.1: Specifications of Benchmark GPUs

CARD	CUDA CORES	CORE FREQ.	GLOBAL MEMORY	PEAK PERFORMANCE
GTX 560	336	810 MhZ	1024 MB 256 Bit GDDR5	7.26 GFLOPS
GTX 660	960	980 MhZ	2048 MB 192 Bit GDDR5	13.44 GFLOPS
GTX 680	1536	1006 MhZ	2048 MB 256 Bit GDDR5	15.85 GFLOPS

5.3.2.2 Test Scenarios

Proposed performance test scenes specify the complexity of the scene geometry and radiometric properties. For example, *Performance Test Scene* 4 contains mesh based complex geometry models with specular and diffuse surfaces whereas, *Performance Test Scene* 1 has more primitive geometry with only diffuse surfaces as given in section 5.1.

In addition to test scenes, a number of test scenarios are defined to analyze the effects of the different performance parameters. Performance simulations are employed on the benchmark GPUs for each of the proposed four performance test scenes with varying scene resolutions and different signature models. The test scenarios consist of different screen resolutions which are selected as $320x240$, $640x480$ and $1024x768$ and the proposed signature models, which are spectral and band-averaged signature models.

For the screen resolution analysis, band-averaged signature model is used in test simulations. Similarly, for the signature model analysis, test simulations are performed with $512x512$ screen resolution. Furthermore, accurate scene radiance calculation is directly proportional to the number of spectral wavelength bin in the band interval of interest. Hence, for the spectral signature model simulations, total spectral wavelength number in the MWIR and LWIR bands is selected as 128, which is sufficient to represent spectral characteristics of the radiometric components.

5.3.2.3 Analysis Results

In this section, performance analysis results of the test scenarios are presented with tables for each of the benchmark GPUs. Benchmark measurements do not include any preprocessing calculation time. However, it includes the time it takes to ray trace scene geometry, transfer any data necessary between CPU and GPU, perform the radiance computation, and finally render to OpenGL buffers to display the frames on the screen. Performance measurements are done after 100 iterations of the algorithm with the calculation of the average number of frames per second (fps).

94

Tables 5.2 to 5.4 describe the performance results for the GTX 560, GTX 660 and GTX 680, respectively.

Table 5.2: GTX 560 performance analysis results

Performance	Screen Resolution			Signature Model	
Test Scenes	320x240	640x480	1024x768	Band-Averaged	Spectral
Test Scene 1	628	410	233	442	64
Test Scene 2	552	353	196	371	59
Test Scene 3	434	248	131	283	54
Test Scene 4	345	177	92	204	36

Table 5.3: GTX 660 performance analysis results

Performance	Screen Resolution			Signature Model	
Test Scenes	320x240	640x480	1024x768	Band-Averaged	Spectral
Test Scene 1	623	445	309	482	63
Test Scene 2	535	394	256	403	60
Test Scene 3	442	298	178	328	56
Test Scene 4	374	222	125	258	42

Table 5.4: GTX 680 performance analysis results

Performance	Screen Resolution			Signature Model	
Test Scenes	320x240	640x480	1024x768	Band-Averaged	Spectral
Test Scene 1	720	560	387	585	91
Test Scene 2	588	455	345	465	86
Test Scene 3	510	372	247	381	83
Test Scene 4	420	301	173	298	63

From the test results, it can be seen that the performance is closely related to the image resolution, the complexity of the scene geometry, signature model used and hardware environment. In all of the test scenarios, *Performance Test Scene* 1 is the fastest scene to render since it has simple scene geometry. However, *Performance Test Scene* 4 is the slowest scene due to its scene geometry complexity and specular surface characteristics. For a specular surface, multiple reflections causes more traced rays and results in more computational cost.

Performance results of three benchmark GPUs are listed in Table 5.5. This table presents the results for the band-averaged signature model and $1024x768$ screen resolution case.

Table 5.5: Performance results for the benchmark GPUs

CARD	Test Scene 1	Test Scene 2	Test Scene 3	Test Scene 4
GTX 560	233	196	131	92
GTX 660	309	256	178	125
GTX 680	387	345	247	173

It can be observed that benchmark GPUs have different performance results. These are GPUs of a similar generation; however the GTX 680 has the highest performance for all the test scenes. The GTX 680 is operating at a higher clock rate and it has more CUDA cores, which account for the performance difference. Also the GTX 560 performs slower than the GTX 660 on all test scenes since it has relatively the lowest specifications.

Each pixel requires a large amount of computation to calculate scene radiance. Since the number of pixels is related to the number of ray operations, in a simplified sense, ray tracing performance depends on the number of pixel operations. Hence, screen resolution size has also considerable effects on performance. Table 5.6 illustrates performance results of the screen resolution analysis when benchmarking the simulator on the GTX 680.

Table 5.6: Performance results for the screen resolutions

Screen Resolution	Test Scene 1	Test Scene 2	Test Scene 3	Test Scene 4
320x240	720	588	510	420
640x480	560	455	372	301
1024x768	387	345	247	173

Performance results of the signature model implementations are also compared. It is important to note that the performance of the system is affected negatively by spectral signature model. Radiometric accuracy requires spectral signature computations at

each wavelength sample in the infrared band interval. Since the radiometric signature calculations for each of the spectral wavelength are implemented as sequantially on GPU and also total incident in-band radiance on the sensor is required to integrate in the infrared band of interest, spectral signature model significantly drops the parallel processing performance in all the test cases. Table 5.7 shows the GTX 680 benchmark results of the signature model analysis.

Table 5.7: Performance results for the signature models

Signature Model	Test Scene 1	Test Scene 2	Test Scene 3	Test Scene 4
Band-Averaged	585	465	381	298
Spectral	91	86	83	63

As it can be observed that there is minimal performance difference between test scenes in the spectral signature model since in this implementation spectral radiance computations are executed as sequentially. Therefore, parallel processing power cannot be used effectively.

5.3.2.4 Discussions on Performance Analysis

In this section, results of the performance analysis of the test scenarios are discussed in general. It can be seen from the analysis results that infrared scene simulation performance highly depends on the simulated test scene complexity, screen resolution and signature model. Moreover, benchmarking results show that GPU parallel processing capabilities also affect the performance.

Performance analysis results show that the band-averaged signature model has significant performance gain over the proposed spectral signature model implementation. For the Test Scene 4, it is about 4.7 times faster. When the test scene has a simple scene geometry such as Test Scene 1, the speedup increased to a factor 6.4. This is not surprising, since the band-averaged signature model implementation is well suited for execution on the GPU. Therefore, it is believed that spectral signature model algorithm can be accelerated further by paralleling the sequentially implemented spectral radiance calculations.

As shown in signature analysis section, in some cases, it is observed that the lack of exact radiometric calculation is not critical and band-averaged radiometry data can be valid for signature modeling. For this purpose, it is advantageous to use band-averaged signature model for the LWIR band, where radiometric data display little spectral variation across the band of interest. Hence, this proposed model implementation provides significant performance gain.

To achieve full performance on GPU, many threads should be work in parallel. Modern GPUs are manycore architectures with thousands of cores which can be exploited for massively parallel computations. Performance gain differences between the benchmark GPUs become obvious when the number of parallel executions increases. For example, the GTX 680 has a performance gain of $1.2x$ over the GTX 560 for the $320x240$ screen resolution in *Performance Test Scene* 4 whereas, it has $1.88x$ for the $1024x768$ case.

The GPU code is actually executed in groups of 32 threads, which is called as warp in CUDA. If the parallelization efficiency of the algorithm are good enough, latency hiding can be provided with switching warps when memory operations are executed and performance of a GPU application be increased. One of the important limiting factor of the parallelization in CUDA is branching. The performance of a GPU application can be significantly reduced if there are thread divergence inside warps, or if only some of the execution units are processing at the same time. If two threads diverge, they are executed serially instead of in parallel. This causes a significant decrease in performance. Unfortunately, there is much branching in ray tracing algorithm. This is the possible reason of that The GTX 680 is demonstrated to offer a speedup of $1.66x$ to $1.88x$ over GTX 560 on test scenes, which is less than the theoretical FLOPS increase offered by GTX 680, about $2.2x$.

It is concluded from the measurements that tracing the scene geometry and spectral radiance computations take a chunk of the time per frame. Especially, spectral signature calculations in a sequential process and integrating spectral radiances in the infrared band interval are major bottlenecks. This is due to fact that after the ray tracing the scene geometry in a parallel fashion, in order to compute total in-band radiance of the closest hit point, spectral radiance calculations for each of the wavelengths are em-

ployed as a sequential process. Hence, spectral signature model takes a chunk of the time per frame to calculate wavelength dependent spectral radiances. From this point, performing the spectral signature calculations for each of the wavelength in parallel can increase the performance significantly. It may be also possible to optimize ray tracing the scene geometry, for instance, looking at shared or texture memory, but it may require functionality currently not available in OptiX. Moreover, since thread launches are handled by OptiX, it is unable to experiment with other choices of grid and block dimensions to investigate the parallel processing performance.

As a conclusion, frame rates around $60\ Hz$ are currently being achieved for physics based high fidelity complex infrared spectral scenes at $512x512$ resolution, using a $3.4\ GHz/8GB\ Intel$ 3770 CPU PC equipped with an NVIDIA GeForce GTX 680 graphics card.

CHAPTER 6

CONCLUSIONS AND FUTURE WORK

The aim of this thesis is to develop a GPU based, high fidelity, infrared signature model and scene simulation system. This chapter concludes the research work with an overall summary of the topics that are discussed in explained briefly. Recommendations are made for further research work which may be undertaken in continuation of this work.

6.1   Conclusions

In this thesis work, a physics based scene simulation is developed to simulate infrared scene in 3D by utilizing parallel processing power of state of the art GPU technology. NVIDIA® OptiX™ ray tracing engine makes it possible to simulate high fidelity infrared 3D scenes at high frame rates. The developed system can simulate infrared scenes at high frame rates by employing physics based spectral signature calculations. This computer based infrared scene simulation system can provide a cost effective alternative to field trials in which different complicated conditions can be simulated in a relatively short time with controlled environmental factors.

In the signature modeling part of this thesis work, some physical improvements are proposed as compared to literature review. These improvements are also reflected to the implementation of infrared scene simulation. The improvements are multiple reflections, accurate modeling of atmospheric effects, taking into account for spectral dependency, specular reflections, parallelization of ray tracing algorithm, etc. Furthermore, the developed system is tested on several benchmarks to examine how it

performs in different scenarios with various performance parameters. Also, radiometric accuracy of the proposed signature model is investigated with compherensive analysis. The results show that spectral dependency of the radiometric data and atmosphere effects are important and must be taken into account to render physically accurate infrared images.

The performance results show that by utilizing the current GPU technology and supporting hardware, it is feasible to develop a ray tracing algorithm based scene simulation system on GPU capable of simulating complex and high fidelity infrared images at high frame rates. NVIDIA® CUDA™ architecture allows programmers to develop algorithms that can use highly parallel architecture for general purpose computing. The main and the most important requirement is that the algorithm must be massively parallelizable. Ray tracing algorithm is a massively parallel problem and CUDA computing platform can produce good performance results.

The main goals that are accomplished in this thesis work can be listed as follows.

- Developing a ray tracer based high fidelity infrared signature modeling and simulation system on GPU and a personal computer at high frame rates is accomplished.

- It is demonstrated that OptiX ray tracing engine can be extended to simulate infrared scenes

- Radiative transfer model is applied on signature calculations to simulate the effects of the atmosphere.

- The developed system can generate infrared signatures under a different atmospheric and infrared waveband conditions.

- Detalied signature analysis for radiometric calculations in MWIR and LWIR spectral regions are employed.

6.2 Future Work

In this section, some extensions which are considered as future work to increase the fidelity and performance of the proposed model are discussed.

Fidelity of the infrared signature model can be increased by incorporating a measurement based parameterized BRDF model to calculate reflected radiations.

Parallel processing on GPU is the main capability of this fast ray tracer based simulation. One of the most important future work is that computation power can be increased by parallelizing the spectral infrared signature calculations instead of in a sequential implementation.

Furthermore, fidelity of the infrared signature model can be increased by modeling the heat transfer equations to predict the heat conduction, convection and radiation between scene objects and the environment or integrating a physical thermal model software.

Finally, proposed infrared signature models can be implemented using Monte Carlo ray tracing methods such as path tracing and photon mapping to solve rendering equation.

REFERENCES

[1] F. P. J. le Roux. An investigation into the use of OpenGL as a library for the simulation of infrared scenarios. Master's thesis, University of Pretoria, September 2001.

[2] R. S. Wright, N. Haemel, G. Sellers, and B. Lipchak. *OpenGL SuperBible Fifth Edition*. Pearson Education, Inc, 2010.

[3] Nvidia Corporation. CUDA toolkit homepage @ONLINE. `https://developer.nvidia.com/cuda-toolkit`, June 2014.

[4] NVIDIA OptiX application acceleration engine @ONLINE. `http://www.nvidia.com/object/optix.html`, June 2014.

[5] H. Ludvigsen and A. Elster. Real-time ray tracing using Nvidia OptiX. *Euro-Graphics in Norrkoping*, pages 65–68, May 2010.

[6] Digital imaging and remote sensing image generation (DIRSIG) @ONLINE. `http://www.dirsig.org/`, 2010.

[7] C. J. Willers and M. S. Willers. OSSIM:optronics scene simulator white paper. Tech. Rep. 6700-PG-103400-01 Rev 3, Council for Scientific and Industrial Research (CSIR), February 2011.

[8] J. R. Schott. The image chain approach. *Remote Sensing of Environment*, 2007.

[9] R. Dumont. SAFIR, a software architecture for model interoperability. In *3rd International IR Target and Background Modeling and Simulation Workshop*, 2007.

[10] J. R. Schott, R. Raqueno, and C. Salvaggio. Incorporation of a time-dependent thermodynamic model and a radiation propagation model into infrared three-dimensional synthetic image generation. *Optical Engineering*, 1992.

[11] E. H. ShorLowe, C. Salvaggio, and J. R. Schott. Three-dimensional longwave infrared (LWIR) synthetic image generation incorporating angular emissivity effects using ray tracing techniques. In *SPIE Vol. 1341 Infrared Technology XVI*, 1990.

[12] Y. Yang, Z. Wu, and L. Yao. Method of calculating the radiance of point-source target in infrared image. *International Journal of Infrared and Millimeter Waves*, 23:1347–1355, 2002.

[13] S. J. King and M. A. Richardson. Modeling the signature vulnerability of a main battle tank. *Journal of Battlefield Technology*, 3:29–34, 2000.

[14] T. Shen, M. Guo, and C. Wang. IR image generation of space target based on OpenGL. In *Proc. of SPIE Automatic Target Recognition and Image Analysis and Multispectral Image Acquisition*, volume 6786, pages 1–6, 2007.

[15] C. L. Christie, E. Gouthas, and O. M. Williams. Graphics processing unit (GPu) real time infrared scene generation. In *Technologies for Synthetic Environments: Hardware in the loop Testing XII, Proc. SPIE*, volume 6544, 2007.

[16] O. M. Williams, C. L. Christie, E. Gouthas, and L. Swierkowski. Real time scene generation infrared radiometry. In *Technologies for Synthetic Environments: Hardware in the loop Testing XV, Proc. SPIE*, volume 7663, 2010.

[17] C. L. Christie, E. Gouthas, O. M. Williams, and L. Swierkowski. Dynamic thermal signature prediction for real time scene generation. In *Technologies for Synthetic Environments: Hardware in the loop Testing XVIII, Proc. SPIE*, volume 8707, 2013.

[18] Vega Prime IR Scene Technical Overview. Technical report, MultiGen-Paradigm, 2004.

[19] N. Duong and M. Wegener. SensorVision radiometric equations version 2.2. DSTO Report DSTO-TN-0193, Defence Science and Technology Organisation, February 1999.

[20] M. Lorenzo, E. Jacobs, R. Moulton, and J. Liu. Optimized mapping of radiometric quantities into OpenGL. In *Part of the SPIE Conference on Modeling, Simulation and Visualization for Real and Virtual Environments*, volume 3694, pages 173–182, April 1999.

[21] H. Li. An infrared imaging computation model and its validation. In *International Symposium on Photoelectronic Detection and Imaging*, 2009.

[22] B. T. Phong. Illumination for computer generated pictures. *Communications of the ACM*, 1975.

[23] A. Berk. LOWTRAN-7 user guide. Technical report, Ontar Corporation, Ontario, Canada,, 1989.

[24] *DIRSIG user's manual.* `http://dirsig.org/documentation`, 2006.

[25] Ontar Corp. Ontar software @ONLINE. `http://www.ontar.com/Software/ProductDetails.aspx?item=modtran`, April 2014.

[26] William L. Wolfe. Radiation theory. In W. L. Wolfe and G. J. Zissis, editors, *The Infrared Handbook*, IRIA Series in Infrared & Electro-Optics. The

Infrared Information Analysis (IRIA) Center, Environmental Research Institute of Michigan, Ann Arbor, MI, fourth edition, June 1993.

[27] L. Li, W. Nui, and Z. Wu. Fast calculation of object infrared spectral scattering based on CUDA. In *Proc. Of SPIE*, volume 7854, 2010.

[28] R. G. Driggers, P. Cox, and T. Edwards. *Introduction To Infrared and Electro-Optical Systems*. Artech House, Inc., 2003.

[29] F. E. Nicodemus. *Geometrical considerations and nomenclature for reflectance*, volume 160. US Department of Commerce, National Bureau of Standards Washington, D. C, 1977.

[30] M. Schlessinger. *Infrared Technology Fundamentals*. M. Dekker, Inc, 1995.

[31] R. D. Hudson. *Infrared System Engineering*. Wiley-Interscience, 1969.

[32] B. P. Horn and R. W. Sjoberg. Calculating the reflectance map. A.i. memo 498, Massachusetts Institute of Technology, Artificial Intelligence Laboratory, October 1978.

[33] M. Pharr and G. Humphreys. *Physically Based Rendering*. Elsevier, Inc., 2010.

[34] A. Appel. Some techniques for shading machine renderings of solids. In *In Proceedings of spring joint computer conference*, 1968.

[35] T. Whitted. An improved illumination model for shaded display. *Communications of the ACM*, 23:343–349, 1980.

[36] *NVIDIA OptiX Ray Tracing Engine – Programming Guide Version 3.0*, 2012.

[37] I. Wald. *Real time ray tracing and interactive global illumination*. PhD thesis, Universität Saarbrücken, 2004.

[38] NVIDIA Corporation. CUDA 5.0 C Programming Guide @ON-LINE. `http://docs.nvidia.com/cuda/cuda-c-programming-guide/index.html`, June 2013.

[39] NVIDIA Corporation. Nvidia OptiX Ray-tracing framework @ONLINE. `https://developer.nvidia.com/optix`, June 2013.

[40] S. G. Parker, J. Bigler, A. Dietrich, H. Friedrich, J. Hoberock, D. Luebke, D. McAllister, M. McGuire, K. Morley, A. Robison, et al. Optix: a general purpose ray tracing engine. In *ACM Transactions on Graphics (TOG)*, volume 29, page 66. ACM, 2010.

[41] J. T. Kajiya. The rendering equation. In *ACM Siggraph Computer Graphics*, volume 20, pages 143–150. ACM, 1986.

[42] J. C. Willers, S. M. Willers, and F. Lapierre. Signature modelling and radiometric rendering equations in infrared scene simulation systems. In *SPIE Security and Defence*. International Society for Optics and Photonics, 2011.

[43] A.M. Baldridge, S.J. Hook, C.I. Grove, and G. Rivera. The ASTER spectral library version 2.0. *Remote Sensing of Environment*, 113(4):711–715, 2009.

[44] E. H. Shor. Three-dimensional longwave infrared synthetic scene simulation. Master's thesis, Rochester Institute of Technology, Center for Imaging Science, 1990.

[45] A. Berk, G. P. Anderson, P. K. Acharya, and E. P. Shettle. *MODTRAN 5.2.1 User's Manual*, 2011.

[46] I. Reda and A. Andreas. Solar position algorithm for solar radiation applications. *Solar energy*, 76(5):577–589, 2004.

[47] J. A. Goguen, T. Winkler, J. Meseguer, K. Futatsugi, and J. P. Jouannaud. *Introducing obj*. Springer, 2000.

[48] Desktop GPUs @ONLINE. `http://www.geforce.com/hardware/desktop-gpus`, June 2014.

APPENDIX A

ASTER SPECTRAL LIBRARY

The Advanced Spaceborne Thermal Emission Reflection Radiometer (ASTER) on NASA's Terra platform has been widely used in geological and other science studies. In support of ASTER studies, a library of natural and man-made materials are available as the ASTER Spectral Library. The ASTER library is an excellent resource that provides a comprehensive collection of over 2300 spectra of a wide variety of materials covering the wavelength range $0.4 - 15.4 \ \mu m$. It contains the infrared spectra for various natural materials are available in hemispherical reflectance. Kirchhoff's Law is used to convert to emissivity from hemispherical reflectance.

APPENDIX B

MODTRAN

B.1 MODTRAN Overview

MODTRAN® (MODerate resolution TRANsmission) serves as the U.S. Air Force (USAF) standard moderate spectral resolution radiative transport model for wavelengths extending from the thermal infrared through the visible and into the ultraviolet (0.2 to 10000.0 μm). The MODTRAN program is a computationally rigorous radiation transfer algorithm that is used to calculate the spectral absorption, transmission, emission and scattering characteristics of the atmosphere for wavelengths extending at moderate resolution from thermal infrared through the visible and into the ultraviolet. It can be used to calculate the transmission and/or the radiance for a specified path through the atmosphere. MODTRAN software has been extensively validated and serves as a currently accepted standard atmospheric band model for the remote sensing community. The MODTRAN transmission calculations use three temperature dependent parameters: an absorption coefficient, a line density parameter, and an average line width. The radiance calculations consider contributions from the following sources:

- atmospheric self-emission

- solar and lunar radiance single-scattered into the path

- direct solar irradiance through a slant path to space

- multiple scattered solar and atmospheric emitted radiance into the path.

The MODTRAN package includes several parameters to define the aerosol background. Several aerosol types are available e.g. *Rural, Urban, Desert, Maritime* and *Fogs*. The geometry of lines of sight between the observer and the target can also be specified. Solar and lunar source function parameters can be chosen. MODTRAN is valid over the frequency range 0 to 50000 cm^{-1} or for wavelengths longer than 0.2 μm. The user has many ways of defining the calculation geometry. The geometry package considers effects caused by atmospheric refraction and the curvature of the earth. The atmosphere is treated as a stack of up to 33 atmospheric layers, from 0 to 100 km altitude. Physical parameters, ranging from pressure and temperature to molecular absorption and extinction coefficients, are defined for each layer. Several standart model atmospheres can be used, or the user can supply a custom atmospheric profile based on direct measurements or radiosonde profiles. Aerosol models can also be used to simulate the effects of dust, clouds, or other particulates in the path; standart aerosol profiles or user supplied ones can be used. As the path travels through each layer in the model, the atmospheric components of interest are computed and summed over the path and wavelength band.

B.2   MODTRAN Aerosol Models

An important feature of MODTRAN is its inclusion of aerosol transmission and radiance effects. Aerosols are basically particles suspended in the atmosphere. These particles have widely varying sizes and are located only in certain parts of the atmosphere. The two primary parameters of interest are the extinction and absorption coefficients. Several different aerosol distributions are available for the boundary layer (0 to 2 km). For example; *Rural* model is intended to represent the aerosol conditions one finds in continental areas which are not directly influenced by urban and industrial sources. This continental, rural aerosol background is partly the product of reactions between various gases in the atmosphere and partly due to dust particles picked up from the surface.

B.3   MODTRAN Model Atmospheres

MODTRAN offers two general ways to define atmospheric parameters. The user can either provide meteorological data (from measurements or radiosondes) or use one of several generic model atmospheres. These standart atmospheres are provided to allow modeling of average conditions. Each standart profile defined by pressure, density, temperature and concentration of the molecules as a function of altitude. Most of the infrared radiation originates in the lower atmosphere. The six generic profiles are named according to season and latitude:

- 1976 US Standard Atmosphere

- Tropical Model (15 degrees North)

- Midlatitude Summer (45 degrees North, July)

- Midlatitude Winter (45 degrees North, January)

- Subarctic Summer (60 degrees North, July)

- Subarctic Winter (60 degrees North, January)

The 1976 US Standard Atmosphere is taken from the NASA U.S. Standard Atmospheric Supplements, 1976. The other five seasonal models were put together using data from a variety of sources. They are intendent to represent average seasonal and latitude variations in atmospheric properties. The three parameters that exhibit the most significant changes with location and time are the atmosperic pressure, temperature and water concentration.